ABSTRACT

Title of dissertation: EFFECTS OF WATER PLASMA CHEMISTRY ON HELICON THRUSTER PERFORMANCE

Elaine Petro
Doctor of Philosophy, 2019

Dissertation directed by: Professor Ray Sedwick
Department of Aerospace Engineering

The focus of this work is on the operation of a helicon thruster with water as the propellant. The characteristics of a water plasma are investigated and used to develop an analytical thrust efficiency model for the system. The efficiency of a helicon thruster operating with water vapor is compared to the efficiency with traditional noble gas propellants. Next, the predicted efficiency range is compared with other state-of-the-art electric propulsion devices. The addition of an "electrodeless" ion cyclotron heating stage is investigated as a means of increasing thrust efficiency. The thrust efficiency model is extended to assess the parameter space for which the addition of ion cyclotron heating improves performance. Additionally, a particle-based trajectory model is developed to study antenna sizing, phasing effects, and energy conversion. Finally, the effects of second-order reactions on plasma composition and acceleration efficiency are explored using particle balance and particle-in-cell methods.

EFFECTS OF WATER PLASMA CHEMISTRY ON HELICON THRUSTER PERFORMANCE

by

Elaine Petro

Dissertation submitted to the Faculty of the Graduate School of the
University of Maryland, College Park in partial fulfillment
of the requirements for the degree of
Doctor of Philosophy
2019

Advisory Committee:
Professor Raymond Sedwick, Chair/Advisor
Professor Christine Hartzell
Professor Christopher Cadou
Professor Adil Hassam
Professor James Drake

Acknowledgments

"All of our dreams can come true if we have the courage to pursue them."

- Walt Disney

Research is often depicted as a solitary endeavor, where the achievements of the individual are celebrated. In my experience, it has been everything to the contrary that is most important. While I spent more time than suits my personality alone in concentrated thought, with only textbooks and my computer, these are not the moments that define my graduate degree. I owe the achievement of this milestone to all of the incredible people that have been in my life and have supported me over the past 6 years and beyond. This is in no way a solitary effort or accomplishment.

First, I want to express my gratitude to my research advisor and mentor, Dr. Ray Sedwick. I would likely not have had the courage to pursue a Ph.D. were it not for him going out of his way to tell me that I should consider it as a senior undergraduate in 2010. I may have never had as good of an opportunity to follow through on it if he didn't go out of his way to open the door for me to join his lab when I was finally ready to apply in 2013. And I would certainly have not enjoyed the many opportunities and successes that I was lucky to have in my graduate career without his guidance. I hope to pay it forward by attempting to be as good of a mentor to future students as he has been to me and my labmates.

Next, I want to thank my committee members who have been my instructors and mentors over the course of my graduate study. I am grateful to Dr. Jim Drake and Dr. Adil Hassam for their instruction in plasma physics, their technical insight, and for helping us bridge the communities of electric propulsion and plasma physics at UMD. I want to thank Dr. Christine Hartzell for serving on my committee and expanding the breadth of space research in our department. The department has been greatly improved by her presence. I want to thank Dr. Chris Cadou for being an instructor and mentor since my undergraduate years and a wonderful role model in our department. I also want to thank our fantastic department chair, Dr. Norm Wereley, for being an important mentor to me since I met him as an undergraduate and for being a tireless advocate for the students in our department.

I am deeply indebted to a few organizations and the people behind them who generously supported my graduate research through fellowships. This includes the National Science Foundation, the Zonta Foundation, the ARCS Foundation, the University of Maryland Graduate School, the Clark School Women in Engineering Program, the Department of Aerospace Engineering, and the Brown Family. I want to particularly thank Mary Snitch and Dr. Keoki Jackson from Lockheed Martin who have been sponsors and mentors to me for the past 2 years.

I want to thank my wonderful friends and family both inside and outside of the university. Among my many fears about graduate school was the thought that I may be able to make friends. Luckily I was wrong and instead, my labmates, classmates, and friends in aerospace community at UMD have been the absolute best part of my graduate experience. I want to especially thank my SPPL labmates (Pratik, Eric, Arber, Adriane, Matt, Josh, John, Jarred, Adam, Drew, Allison, Melissa, et. al.) who have been my best friends, role models, study partners, practice audiences, roommates, happy hour company, karoake partners, dogsitters, comic relief, and therapists over the past years and for years to come. Every one of you has inspired me and helped me grow into a better person by your influence.

I am blessed to have an incredibly wonderful and supportive family from my grandparents and aunts who celebrate even the smallest accomplishment, to my parents who told me that I could be anything I wanted to and my little brother who has taught me most of the real-world engineering that I know. I wouldn't be here without the support of my husband, Peter, who has been with me for every turn, always reminding me the importance of getting 8+ hours of sleep. And of course I have to mention our dog, Ally, who has been with me throughout graduate school and our new dog, Penny, who joined us for the final stretch.

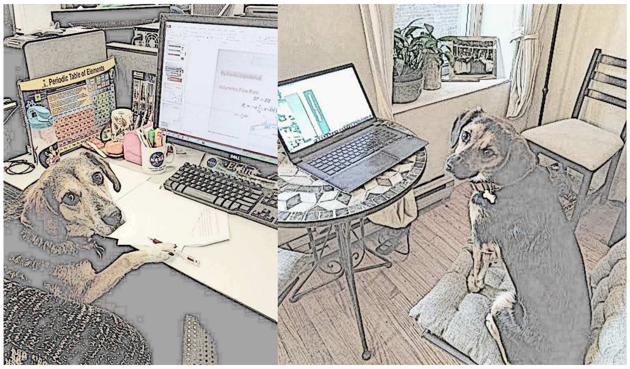

Lastly I want to acknowledge the coffee shops that have made this thesis possible. Among those closest to my heart are Capitol City Cheesecake (Takoma Park, MD), the Board and Brew and Vigilante (College Park, MD), Flour and Sofra (Cambridge, MA) and Fuel (Boston, MA). Thank you to everyone that has supported me and made the last 6 years an amazing experience. It means more than I can ever say. I look forward to a lifetime of learning from these continued friendships and the chance to make new friends and role models both within and beyond the aerospace community.

"Everyone you will ever meet knows something that you don't" -Bill Nye

Table of Contents

List of Tables

List of Figures

Chapter 1: Introduction

1.1 Introduction and Motivation for Study

Electrodeless plasma thrusters have attracted interest as they offer the potential for high velocity (>10,000 m/s) exhaust beams without life-limiting accelerating grids or neutralizing cathodes [2]. An electrodeless thruster generically consists of a radio-frequency (RF) ion source, such as helicon or electron cyclotron resonance (ECR), confined in a dielectric chamber with an axial magnetic field. Downstream of the plasma generation region, the chamber is open to space where the plasma escapes along a diverging magnetic field. The plasma expands with the magnetic field and eventually detaches to form the exhaust plume.

There has been additional interest in electrodeless thrusters because of their amenability to a wide range of propellants [3]. Traditional EP systems such as ion engines or Hall thrusters have walls and grids that are susceptible to erosion by the plasma environment. Thus, non-reactive noble gases have been preferred as propellants in these systems. Noble gases also have fewer energy loss pathways in the ionization process than molecular gases. However, cost, ease of storability, and accessibility for in-situ refueling are all motivating factors to explore the use of alternative propellants. The absence of accelerating grids makes electrodeless thrusters

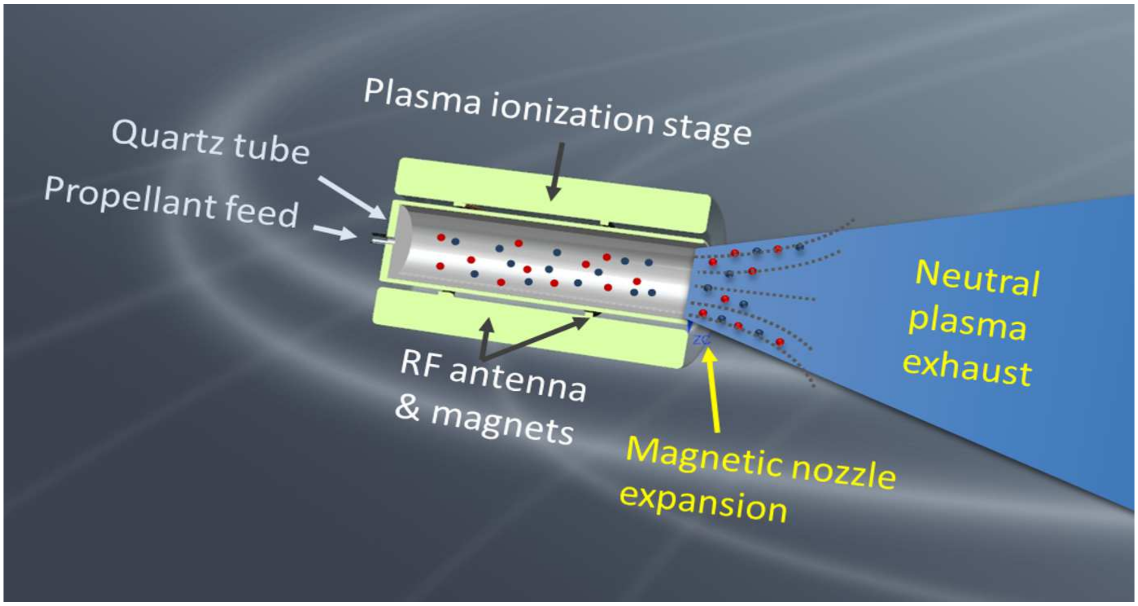

Figure 1.1: Diagram of an electrodeless plasma thruster.

an ideal candidate for this task. Early helicon source experiments characterized operation with non-noble gases such as H_2 [4, 5] and SF_6 [6], to study potential structures in the plume. Charles et. al. later evaluated the propulsive characteristics of additional molecular propellants, including CO_2, N_2, O_2, NH_3, and CH_4 [7]. They were able to measure ion exhaust velocities in excess of 10,000 m/s for all gases in their experiments. Another group employed kinetic schemes combined with particle-in-cell plume modeling to predict the performance and optimal operating points for a helicon thruster using H_2, O_2, N_2, and N_2O [8]. They found N_2O to perform the best due to its low ionization potential (12.9 eV).

The present work focuses on the use of water vapor, H_2O, as a propellant, which has an even lower ionization potential than N_2O (12.6 eV), and could be more easily harvested for refueling. In addition to being easily storable, water has been identified in various forms at the majority of bodies in the solar system. Missions to distant bodies high in water content, such as Enceladus or Europa, could prove ideal applications for refueling operations for high specific impulse (Isp) thrusters. Furthermore, missions with a focus on astrobiology are designed to seek out liquid water and would greatly benefit from the ability to harvest propellant for sample return.

1.2 Water Plasmas and Electric Propulsion

The exploration of water as a propellant for spacecraft has had steady interest over the past several decades with a renewed enthusiasm of late. The development of the small satellite market along with strict launch constraints on secondary payloads has made inert and inexpensive propellants like water particularly attractive. Several groups are interested in using electrolysis to dissociate the water molecule into the reactive species H_2 and O_2 and recombine to produce thrust. This architecture could prove valuable for CubeSats and other spacecraft if successful, but will be limited to a chemical propulsion Isp of 450 seconds or less. For long duration small-sat missions and large payload cargo transport, a high Isp to match the large mission velocity change (Δv), requirements is imperative. Thus there is also interest in water-plasma architectures to provide high Isp solutions for these and other applications.

The development of a water-based plasma thruster requires a merging of background knowledge from the field of electric propulsion and the broader field of molecular plasmas. Both fields typically fall in the category of low-temperature plasmas

($T_e < 10$ eV). Molecular plasmas are often studied in the context of applications such as surface processing or atmospheric chemistry, spanning many orders of magnitude in density and pressure. An example of the breadth of studies of water plasma for various applications is included in Fig. 1.2 across a wide range of mean free paths (mfp) and gas pressures.

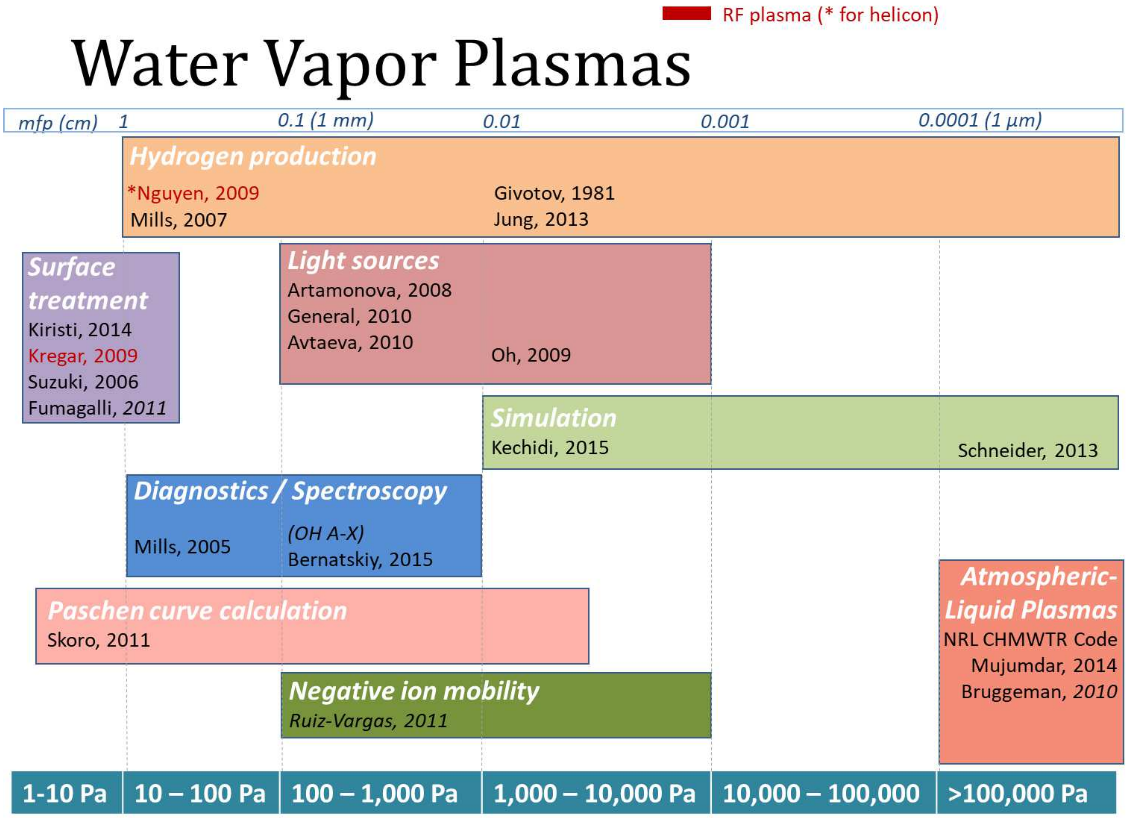

Figure 1.2: Organization of Water Plasma Studies by Topic and Density Regime

Electric propulsion systems fall on the low pressure side of the this spectrum. Despite the importance of water in our society and the various applications of water-based plasmas, there are still wide knowledge gaps in this area. For example, while characterization of neutrals is easy, most experimental work has not clearly identified the composition of ion species, especially ratios of species close in mass such as

H_2O^+, OH^+, and H_3O^+. Nor have researchers well characterized other plasma properties such as ionization fraction and electron temperature for discharge regimes of interest to the propulsion community. On the other hand, electric propulsion systems such as Hall thrusters, ion engines, and other electrodeless concepts have been largely operated with noble gas propellants. Thus the majority of the numerical and experimental knowledge in this field is devoid of molecular effects. This thesis represents an extension of the field of electric propulsion by considering the effects of the molecular propellant, water, on performance. While this work has been motivated by interest in using water in electrodeless thrusters, many of the conclusions and methods are applicable to a more general set of architectures. An outline and executive summary of the key contributions of this effort is provided in the following section.

1.3 Outline of Thesis and Contributions

- **Chapter 2: State of the Art in Electric Propulsion** includes a survey of the state of the art in the field of electric propulsion for advanced systems that operate at a similar size and power scale to electrodeless concepts. A literature review of electrodeless thrusters, including those that use helicon plasma generation ("helicon thrusters") is provided and compared to the state-of-the-art in the field. The performance of all systems is evaluated in the context of mission-driven needs for solar system exploration.

  This chapter has been peer-reviewed and published in the *Journal of Spacecraft* *and Rockets* according to the following citation:

Petro, E. and Sedwick, R.,
Survey of moderate power electric propulsion systems,
Journal of Spacecraft and Rockets, Vol. 54 (3), 2017.
`https://doi.org/10.2514/1.A33647`

- In **Chapter 3: Single Stage Performance Analysis**, the effects of water plasma processes on system efficiency are investigated. The modes of energy deposition in a low density water plasma are explored and incorporated in the analysis of the water-based thruster. Contributions from this chapter include an ionization cost (energy required per ion) model for a Maxwellian water plasma and a model for the thrust efficiency of an electrodeless water plasma thruster.

  This chapter has been peer-reviewed and published in the *Journal of Propulsion and Power* according to the following citation.

  Petro, E. and Sedwick, R.,
  Effects of Water-Vapor Propellant on Electrodeless Thruster Performance,
  Journal of Propulsion and Power, Vol. 33 (6), 2017.
  `https://doi.org/10.2514/1.B36389`

- In **Chapter 4: Helicon Thruster Performance with An Acceleration Stage**, the analysis developed in Chap. 3 is extended to assess the efficacy of ion cyclotron heating (ICH) for a small-scale electrodeless thruster with water vapor as its propellant. This model is used to perform scaling studies to investigate the physical dimensions and magnetic field strengths for which efficiency improvements over a single-stage design can be obtained. Finally, details of single-particle ion heating and conversion of perpendicular to parallel energy are captured using 3D trajectory simulations. Calculations are performed to couple the magnetic field strength, device radius, and antenna length. Analysis of a 10 centimeter diameter ICH stage is presented.

This chapter is composed of work that has been peer-reviewed for and published in the following conference proceedings:

Petro, E. and Sedwick, R.,
Effects of Water Vapor Propellant on Helicon Thruster Performance,
52nd AIAA/SAE/ASEE Joint Propulsion Conference, 25-27 July, Salt Lake City, Utah, AIAA 2016-4735, published online 22 July 2016,
`https://doi.org/10.2514/6.2016-4735`

Petro, E. and Sedwick, R.,
Ion Cylotron Heating in an Eletrodeless Water Vapor Thruster,
35th International Eletric Propulsion Conference, 8-12 October, Atlanta, Georgia IEPC-2017-468, published online 12 October 2017.

- In **Chapter 5: Effects of Plasma Composition on Acceleration Efficiency**, the details of second-order plasma chemical reactions on both discharge composition and acceleration efficiency are assessed. A zero-D particle balance model is developed to investigate the effects of ion-neutral and ion-electron reactions on plasma composition. Next, the effects of these reactions on plume formation during the acceleration process are investigated using particle-in-cell simulations.

  This chapter is has been accepted for presentation at and publication in the following conference proceedings:

Petro, E., Brieda, L., and Sedwick, R.,
PIC Simulations of Chemistry Effects
in an Electrodeless Water Plasma Thruster,
55th AIAA/SAE/ASEE Joint Propulsion Conference,
19-22 August, Indianapolis, Indiana

- **Chapter 6: Conclusions and Future Work** provides the conclusion to the thesis and suggestions for future work in several sub-topic areas.

Chapter 2: State of the Art in Electric Propulsion

This chapter has been published in the *Journal of Spacecraft and Rockets* according to the following citation. At the time of this thesis publication, it has been cited 7 times!

Petro, E. and Sedwick, R.,
Survey of moderate power electric propulsion systems,
Journal of Spacecraft and Rockets, Vol. 54 (3), 2017.
`https://doi.org/10.2514/1.A33647`

Section 2.4.3 is added here and was not included in the published manuscript. It provides an overview of helicon thrusters and their demonstrated performance in the context of other EP systems.

2.1 Introduction

Electric propulsion (EP) systems have become an integral component of many space mission architectures. The field of EP has grown to include many unique systems that fill niches from primary propulsion for high impulse missions to precision control for formation flight. The intent of this review is to focus on a subset of the technologies driven by a particular mission application. Specifically, the state of the art in moderate power systems that are applicable to deep space exploration missions is assessed. A brief overview of the fundamentals of EP is included, followed by a discussion of the mission characteristics that guide thruster selection for this study.

While the field of electric propulsion is wide and the variety of thrusters developed is vast, EP systems are united in the goal of increasing the efficiency of propellant usage by achieving high specific impulse. The specific impulse, Isp, characterizes how efficiently the propellant is used to impart momentum change and is closely related to the propellant exit velocity, u_e. Formally, it is defined as the amount of impulse provided per unit weight of propellant and can be calculated as the ratio of the thrust force, F_t, multiplied by the thrusting time, τ, to weight of propellant at the earth's surface as given in equation 3.7 below (where m_p is the propellant mass expelled, and g is the acceleration due to gravity).

$$Isp = \frac{F_t \cdot \tau}{m_p \cdot g} = \frac{m_p \cdot u_e \cdot \tau}{m_p \cdot g} = \frac{u_\varepsilon}{g} \tag{2.1}$$

If the propellant flow rate, $\dot{m}_p$, is assumed constant, then the specific impulse is determined by the exit velocity alone. The impact of high Isp on mass savings can be seen through the rocket equation (per the above definition, $Isp \cdot g$ appears in the rocket equation in place of the exit velocity, u_e).

$$\frac{m_0}{m_f} = \frac{m_f + m_p}{m_f} = e^{\Delta v / \,\mathrm{Isp}\, \cdot g}; \quad m_p = m_f \left(e^{\Delta v / \,\mathrm{Isp}\, p \cdot g} - 1 \right) \tag{2.2}$$

where m_f is the final mass after all propulsive maneuvers, m_0 is the initial wet mass of the spacecraft, and Δv is the velocity change required to reach the desired destination. For missions with large delta-v requirements, such as geosynchronous station-keeping or interplanetary explorers, the propellant mass savings achievable with EP systems becomes significant.

From a practical perspective, the propellant mass savings must be weighed against the added power system mass required to produce a higher Isp. For electric power supplies, the mass of the power system hardware, m_{ps}, is proportional to the required power [9].

$$\alpha(P) = \frac{P}{m_{ps}} \tag{2.3}$$

For an EP system, the required power, at constant thrust, is directly proportional to the Isp, as given by Eq. 2.4.

$$P = \frac{T \cdot \mathrm{Isp} \cdot g}{2\eta} \tag{2.4}$$

While a higher Isp will always minimize the propellant mass, a more sophisticated analysis shows there is an optimal Isp that minimizes the total wet mass, m_0. For a given payload mass and delta-v, this is equivalent to minimizing the sum of the power system and propellant masses. A simple illustration of this principle is given by Eq. 2.5.

$$\left(\frac{\partial m_0}{\partial Isp}\right)_{m_{pl}} = \left(\frac{\partial\left(m_{ps} + m_{prop}\right)}{\partial Isp}\right)_{T,n} = 0 \rightarrow Isp, opt = \left(\frac{\Delta v}{g}\right)\left(1 + \frac{m_{pl}}{m_{ps}}\right) \tag{2.5}$$

The result given by Eq. 2.5 reduces to $Isp, opt \approx \Delta v/g$ when the power system dominates the dry mass ($m_{ps} \gg m_{pl}$) and $Isp, opt \approx 2\Delta v/g$ when the power system and payload masses are comparable ($m_{ps} \approx m_{pl}$). Thus, when the propulsion system drives the power system mass, the optimal Isp depends on the payload and power system characteristics and scales with the mission delta-v. A more detailed analysis of these principles is performed in [10]. Thus, performance scaling with input power is a critical factor for EP system evaluation.

Many variations of electric thrusters have been developed that are often separated into three categories based on the dominant ion acceleration mechanism: (1) electrothermal (2) electrostatic and (3) electromagnetic. Electrothermal thrusters, such as arcjets and resistojets offer moderate gains in specific impulse over chemical propellants and have been heavily implemented for station keeping and orbit raising applications in earth orbit. Electrostatic and electromagnetic thrusters offer significant gains in specific impulse, typically in the range of 1000 to 3000 seconds and have been preferred for deep space exploration missions. For an overview of the broader history of EP, the reader is referred to book publications such as those by Katz and Goebel [11] or Jahn [12].

Because the performance range and implementations of the different thruster types are so varied, it is desirable to look at a subset of the broader EP landscape instead of a comprehensive review of the field. Often, mission constraints such as available power, delta-v, and optimal specific impulse, limit the applicable propulsion systems to just a few options. Thus an in-depth comparison of EP systems suitable for a particular mission type is appropriate. Though surveys of electric propulsion performance are periodically published [9,13], they typically only quote only a few performance points for any particular technology (which suffices for their purpose). In contrast, presented here are detailed performance data that are typically omitted from the above mentioned sources. This analysis includes a compilation of data for all major thrusters of a particular class, both in the laboratory and on-orbit. This survey also aims to investigate the variation in performance across a range of input powers for several different technologies. Performance data is compiled and presented in a format that will be useful to mission planners interested in incorporating and comparing state-of-the-art EP systems for all phases of their mission. In addition, trends across thruster class are established that may be used as a point of reference for those interested in developing new thruster architectures or improving upon existing systems.

2.2 Motivation and Scope

Any mission reliant on solar power that ventures out of earth's orbit must operate over a wide range of input power as available solar energy decreases $\propto 1/r^2$ with distance from the sun. For missions that travel sufficiently far from the sun, nuclear power becomes essential. The trade between solar electric propulsion (SEP) and radioisotope electric propulsion (REP) is often made for missions to the outer solar system. The constraints levied by the power system on the thruster are introduced briefly below. SEP and REP mission architectures discussed in detail in Section III.

For a solar-powered system, the mission designer is particularly interested in performance across a range of input power, spanning up to an order of magnitude for deep space missions. Typical mission architectures span from tens of kW near Earth to only a few kW or less at the destination. For example, the solar arrays on the Dawn mission supplied 10.3 kW total power at 1 AU and only 1 kW at 3 AU [14]. For REP missions, due to the current state of the art in REP specific power (power provided per kg of hardware) and tight mass budgets, the performance of EP systems in the sub-kW power range is of greatest interest. Thus it is important to understand the variation in EP system performance with input power for both SEP and REP architectures. For example, it will be shown that the demonstrated thrust efficiency of both Hall thrusters and ion engines tends to drop off significantly at input powers below 1 kW, both due to physical loss mechanisms and immaturity of development.

Thus a survey was performed of existing electrostatic and electromagnetic thrusters that would be suitable for moderate power SEP and REP exploration missions. Electrothermal thrusters are not included in this survey as they typically have significantly lower Isp, higher thrust, and different intended propulsive applications. For this survey, thrusters were selected that operate between 0.1 and 10 kW, offer an Isp on the order of 1000 seconds, and thrust levels on the order of mN. The systems that meet these requirements are generally ion engines, Hall thrusters, and spin-off designs of the two. Helicon thrusters are also assessed as an emerging technology in this power class, though the state of the art is still relatively immature. A list of particular designs included in this survey with accompanying references is included in the sections unique to each technology that follow.

2.3 Mission Applications

In this section, a brief overview of missions which incorporate of electric propulsion for deep space exploration is presented. In some cases, such as rendezvous with one of the ice giants Uranus or Neptune, the use of EP enables a mission that might otherwise be unfeasible with traditional propulsion methods. For lower delta-v missions, the use of EP results in propellant mass savings that can be reallocated to improve a science instrument suite. As mission cost often scales by the mass of the spacecraft at launch [15], the mass savings enabled by EP can also lead to significant cost savings. For example, the incorporation of solar electric propulsion allowed the DAWN mission to fit under the Discovery class of missions ($450M) instead of having to compete as a New Frontiers ($650M) or Flagship mission ($1B) [16].

To date, EP has been employed as the primary propulsion system on five exploration missions: Deep Space 1, SMART-1, DAWN, Hayabusa, and Hayabusa 2. As each of these missions relied on solar arrays, the power available for the propulsion system varied significantly over the course of the mission. In Table 2.1, the maximum and minimum input power (per thruster) are presented for each mission to give an idea of the operating ranges required.

Building on the success of the above listed missions, SEP will continue to be considered for future Discovery and New Frontiers class missions. Oh et. al. [22] performed a parametric study of 3 existing EP systems for 3 different missions: a near-Earth asteroid sample return, Vesta-Ceres rendezvous, and comet Kopff rendezvous. They find that because cost caps limit solar array size, Discovery-class

Table 2.1: SEP exploration missions

Mission	**Ref.**	**Launch Date**	**Destination(s)**	**Electric Thruster**	**Max. Power (kW)**	**Min. Power (kW)**
Deep Space 1	[17]	October 24, 1998	Asteroid 9969 *Braille*	*NSTAR* Ion Engine	1.94	0.48
Hayabusa	[18]	May 9, 2003	Asteroid 25143 *Itikawa*	*Mu-10* Microwave Ion Engine	0.35	0.25
SMART-1	[19]	September 27, 2003	Lunar orbit	*PPS-1350-G* Hall Thruster	1.41	0.65
DAWN	[20]	September 7, 2007	Protoplanets *Vesta and Ceres*	*NSTAR* (modified) Ion Engine	2.57	0.52
Hayabusa II	[21]	December 3, 2014	Asteroid 162173 *1999* JU_3	*Mu-10* Microwave Ion Engine	0.42	0.31

missions greatly benefit from EP systems that are able to operate efficiently at power levels below 5 kW. In a later study [23], they evaluate existing EP systems against practical considerations such as flight heritage and hardware adaptability. These factors are not assessed in the present survey but are certainly of significant practical importance. For missions to the outer solar system, mission planners must often evaluate trades between SEP and REP, or a combination thereof. The architecture for a mission reliant on REP is quite different than SEP missions. The only nuclear power source appropriate for moderate power (kW level) electric propulsion are radioisotope thermoelectric generators (RTGs). Solar arrays are an obvious choice for near-Earth missions as they are both cheaper and have a higher specific power (power delivered per unit mass of power system hardware). At 1 AU, current solar arrays output around 50 W/kg. In contrast, the GPHS (General Purpose Heat Source) RTG which flew on Cassini had a specific power of 5 W/kg and the MMRTG (Multi-Mission RTG) designed for the Mars Science Laboratory is even lower at under 3 W/kg [24]. However, the performance of solar arrays decreases drastically for deep space missions. For example, with a mass of 204 kg, the specific power of Dawn's solar arrays drops to 6.4 W/kg at 3 AU [14]. Thus, REP is often proposed over alternate power and propulsion options to enable rendezvous with one or more of the four outer planets (Jupiter, Saturn, Uranus, and Neptune) and their moons. In contrast to SEP missions which may lose an order of magnitude of power with distance, an RTG will maintain a relatively constant power output, only losing about 5% performance every four years [25].

Traditionally, deep space missions such as Voyager I and II or more recently, New Horizons, have employed an RTG with a simple monopropellant thruster and have only been able to perform fly-bys of planetary bodies. More detailed science could be performed by entering into orbit around the body, but this significantly increases the mission delta-v. Many REP mission concepts have been proposed to enable such missions where chemical or monopropellants cannot. A brief summary of some conceived REP enabled explorers are presented in Table 2.2. The assumed operating power and performance for the EP systems are included.

Additional studies have been conducted that look parametrically at REP enabled missions to determine optimal architectures. For example, Oleson et. al. [29] found that trip times are significantly reduced if a powerful upper stage is used to deliver a light spacecraft directly into an escape orbit and REP is used to decelerate

Table 2.2: REP exploration missions

Mission Type	**Ref.**	**EP Usage**	**Assumed Thrust, Isp**	**Power per Thruster (W)**	**Number of Thrusters Required**
Pluto Orbiter Probe	[25]	Pluto orbit capture, spiral to low altitude orbit	35 mN, 4500 s	500	2 primary, 2 redundant
Uranus Orbiter	[26]	Uranus orbit capture	15 mN, 3200 s	500	2 primary, 2 redundant
Chiron Orbiter	[27]	Chiron orbit capture	39 mN, 1585 s	578	3 primary, 1 redundant
Neptune System Explorer	[28]	Small maneuvers between Earth and Triton flybys	119 mN, 3090 s	3000	2 primary, 1 spare

near the target body. They also found the best balance between payload mass and trip time to occur for a total REP input power of 750 W for this architecture. Constraints on REP mission power levels are mostly driven by cost caps, availability of nuclear fuel, and launcher capabilities [24]. In a white paper submitted for the Planetary Science Decadal Survey [30], Noble and colleagues cite the need for EP systems that achieve 65-75% efficiency at power levels below 3 kW for use on REP missions. A goal of this survey is to assess the state of the art in electric propulsion and evaluate the performance against both REP and SEP mission requirements. Proposed operating points for these missions span at least 2 orders of magnitude in input power. REP missions will generally be interested in sub-kW performance and thrusters that are efficient at one particular operating point. SEP missions benefit from thrusters that are efficient over a wide range of input powers, with the particular limits determined by the mission class and destination. Some key considerations are summarized:

- REP missions generally are proposed with a total power budget on the order of 1 kW and approximately 500 W or less dedicated to each thruster.
- REP missions benefit from high thrust efficiency EP systems ($> 65\%$) below 3 kW.
- Discovery-class SEP missions benefit from high thrust efficiency at input powers below 5 kW.
- All SEP missions benefit from high thrust efficiency over a wide power range (several hundred watts to several kW).

2.4 Technologies Surveyed

Based on the mission scenarios presented in Section 2.3, performance data was collected for Hall, ion, hybrid and existing helicon thrusters designed to operate between approximately 0.1 and 10 kW. Operating parameters such as thrust and specific impulse have been tabulated and compared across thruster type and power level.

While parameters such as specific mass (mass per unit power) and lifetime are also important factors in the selection of an EP system, they are not fully explored in this study. It is generally expected that both the mass of the thruster and accompanying power processing unit (PPU) grow linearly with input power above a threshold value. Scaling models for thruster mass, m_T, and PPU mass, m_{PPU},

Table 2.3: Representative EP system masses

Mission	**Ref.**	**Thruster Unit Mass, kg**	**PPU Mass, kg**	**Other Components, kg**
Hayabusa	[32]	2.3 kg	2.1 kg (power unit), 2.3 kg (microwave supply)	34.5 kg (propellant tank, tubing gimbal, control unit)
DAWN	[33]	8.2 kg	13.3 kg (power processing unit)	24 kg (propellant tank and tubing)

that were developed by Hofer and Randolph [31] based on flight systems are given in Eqns. 2.6 and 2.7 below. P is the input power in kW.

$$m_T = 1.87P + 0.71 \tag{2.6}$$

$$m_{PPU} = 1.74P + 4.65 \tag{2.7}$$

The total mass of an EP subsystem is often dominated by the PPU and supporting hardware and does not vary significantly with thruster type within the systems considered. Items such as propellant tanks, gimbals, and control units will contribute considerably to the overall system mass. Some representative values are given in Table 2.3.

Because the thrusters included in this survey fall under a wide range of development levels, it is difficult to compare the lifetimes, many of which have not yet been characterized. The reader is referred to other reviews such as [23, 34] for a detailed summary of demonstrated operating lifetimes and throughput capabilities.

The primary goal of this review is to assess performance over a range of input powers. Thus it is useful to briefly discuss design heritage in this context. While there is significant interest in incorporating EP in deep space exploration missions, it has been spacecraft in Earth's vicinity that have driven the development of most existing systems. Of the 350 spacecraft current flying EP systems, 70% are commercial, Earth-orbiting communications satellites [31]. Thus the power provided by these satellite buses, especially the amount available for geostationary stationkeeping, has been targeted. As the power available has grown, EP systems have followed. For example, Aerojet Rocketdyne's BPT Hall thruster series has grown from 2 kW to 4.5 kW and may extend into the 10-20 kW range [31]. As customers also adopt EP for orbit raising from LEO to GEO, there is interest in power throttling to trade Isp for thrust during the transfer phase. Expanded throttling ranges and variable Isp will also be desirable for exploration missions. Even REP missions with a constant input power could benefit from high thrust operation while in gravity wells near massive bodies and high Isp when in interplanetary cruise. Some of NASA's flight and developmental thrusters have been designed with these principles in mind. For example, the NASA Evolutionary Xenon Thruster (NEXT) project aims to expand the throttling range of the NSTAR thruster to power levels up to 7 kW [35].

While many needs have driven thrusters to higher power, the popularization of CubeSats and other miniaturized spacecraft are spurring innovation on the other end of the spectrum. These small satellites can typically accommodate no more than tens of Watts [36] for an EP system. While there is interest in scaling down Hall thrusters, ion engines, and helicon thrusters to this market, other systems such as electrospray thrusters become competitive at these scales. The effect of the small satellite market on thruster development shows up in some of the designs at the lower end of the spectrum of this study.

Because EP systems are still largely optimized to operate at a specific design point, certain thrusters are more appropriate for a given mission than others. Thus it is useful to categorize performance according to operating power. Also, because most thrusters have been designed to operate at kW level powers, it is useful to characterize sub-kW performance for REP or small-scale SEP applications. For the designs selected, thrust, specific impulse, and overall thrust efficiency were obtained over all available input powers. For most thrusters, data was available for one or two, often optimal, operation points. Some of the flight thrusters, however, have been fully characterized over the entire range of input power. Where thrust efficiency is not directly reported, it is calculated from the reported thrust, specific impulse, and input power. Thrust efficiency η is the measure of percentage of total input electrical power P_{in} that is converted into the exhaust jet power P_{jet} and is defined as:

$$\eta = \frac{P_{jet}}{P_{in}} = \frac{F_t^2}{2\dot{m}_p P_{in}} = \frac{F_t u_e}{2P_{in}} = \frac{F_t l_{sp} g}{2P_{in}} \tag{2.8}$$

Performance of different systems within each thruster class are presented first, along with brief descriptions of their operation. The data presented for ion engines and Hall thrusters are a combination of flight and laboratory demonstrations. The data included for helicon thrusters are a combination of laboratory demonstrations and theoretical predictions due to the relative novelty of these designs. Finally, the performance of the all thruster types are combined and compared. In the following sections, data are presented in chart format to convey typical trends observed across thruster type and power level. Detailed data for each thruster are also included in table format in the Appendix.

2.4.1 Gridded Ion Engines

The gridded ion engine was one of the earliest forms of electric propulsion developed. Ion engines have been flown in space since the 1960s and thus have reached a very mature level of development. An ion engine can be described simply as a plasma source with a grid system on the open end, designed to extract and accelerate the positive ions. Because the volume between the grids contains only positively charged species, space charge constraints limit the maximum current and thus the thrust density of the system. After being energized through the grids, the positive ion beam is neutralized via the injection of electrons from an external cathode. The plasma can be generated and sustained by either direct current (DC) electrodes or radio frequency (RF) wave heating. The RF version inductively heats free electrons with an antenna which typically operates in the MHz range and surrounds the insulating discharge chamber. This design eliminates the need for the potentially life-limiting cathode immersed in the plasma [11]. Electron cyclotron resonance (ECR) discharges are a subtype of RF systems which operate in the microwave frequency range (GHz) in order to resonantly heat magnetized electrons. As defined here, RF thrusters are inclusive of systems with axial magnetic fields, unlike the definition given in [11] and [37]. RF systems are not distinguished by operating frequency in this survey. It will be seen that RF ion engines tend to achieve higher efficiencies than their DC counterparts and have achieved the highest overall thrust efficiency of any EP system to date.

Ion engines also employ varying discharge chamber geometries and magnetic fields. Early ion engines were designed with cylindrically symmetric discharge chambers and an axial magnetic field employed to impede electron transport to the walls. Newer designs often contain a tapered discharge chamber and cusped magnetic fields to further reduce the loss of charged particles to the walls. Designs with solenoidal fields and DC discharges are referred to as *Kaufman-type* thrusters. These magnetic fields are primarily shaped with permanent ring magnets, giving rise to the *ring-cusp* classification. A diagram of each configuration is provided in Fig. 2.1. Most modern ion engines are optimized to operate with xenon propellant because it is inert, relatively high molecular weight, and has a low ionization energy (12.1 eV).

A list of the ion engines considered in this study is presented in Table 2.4. The developer, level of maturity, and references for performance data are also included for each thruster.

For these systems, reported values of thrust, specific impulse, and thrust efficiency are compared across input power in power in Fig. 2.2, Fig. 2.3, and Fig. 2.4, respectively. The results indicate trends in demonstrated operating points, with input power as the chosen mission-relevant variable. However, input power in turn is a function of discharge and accelerating potentials, mass flow rates, and the loss mechanisms that determine efficiency. Thus the results shown here represent trends in

Table 2.4: Ion Engines surveyed

Thruster Name	**Model**	**Developer**	**Discharge Type (DC/RF)**	**Technology Maturation**	**Ref.**
BRFIT	3	Busek	RF	Developed (current)	[38]
	7				
ESA	XX	ESA	RF	Developed (Past)	[39]
IES	XX	JAXA (Melco)	DC	Scheduled for Flight	[40, 41]
Ion Engine (R&D)	–	JAXA	DC	Developed (Current)	[40]
IT	50	Russia	DC	Flight	[42]
	100				
Mu	10	JAXA (Melco)	RF	Flight	[18, 43]
NEXT	–	NASA	DC	Flight	[33, 44]
NSTAR	–	NASA	DC	Flight	[31, 45, 46]
RIT	10	Astrium	RF	Flight	[47]
	22			Developed (Current)	[48, 49]
	35			Developed (Past)	[50]
T	5	ESA	DC	Flight	[51]
	6			Scheduled for Flight	[52]
XIPS	8 cm	L-3 Technologies	DC	Developed (Current)	[53]
	13 cm			Flight	[46, 54]
	25 cm			Flight	[54, 55]

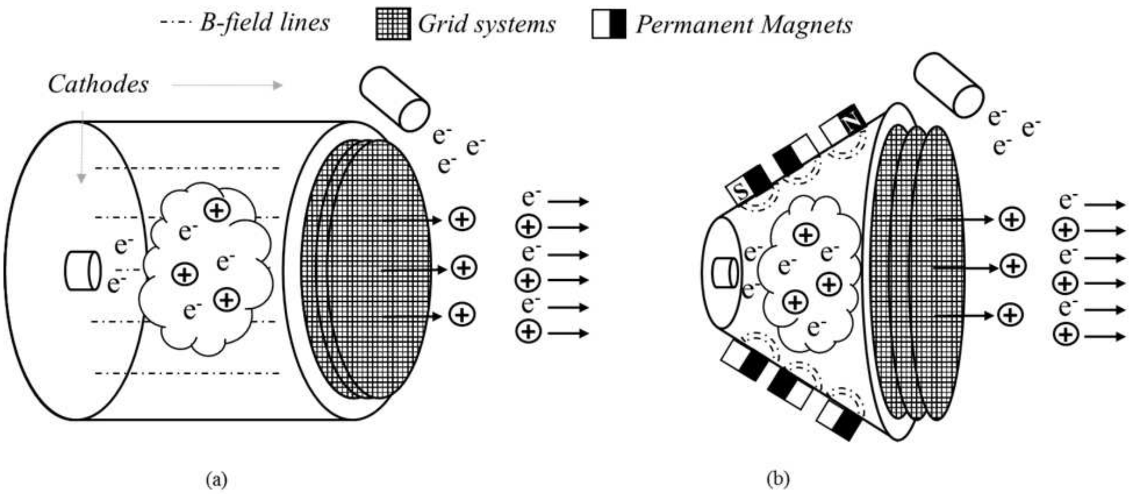

Figure 2.1: Diagrams of ion engine architectures with a) cylindrical geometry and an axial magnetic field and b) a tapered discharge chamber and cusped magnetic fields.

the state-of-the-art published operating points which are influenced both by physical processes and market influences.

The performance trends for ion engines were found to be bracketed by architecture (DC and RF). It can be seen in Fig. 2.2 that the demonstrated thrust increases linearly with input power. A trendline is given by a linear least squares fit, the slope of which characterizes the demonstrated *thrust-to-power ratios* for each system. It is noted that the performance of RF systems begins to deviate from this value below 500 W. One might not expect a priori to find such strong trending over a large range of input power. The linearity of this relationship indicates that the thrust-to-power ratio is not explicitly a function of input power.

Observation of the linear relationship between thrust and power motivated comparison of linear least squares slopes with dataset averages. Direct averaging of

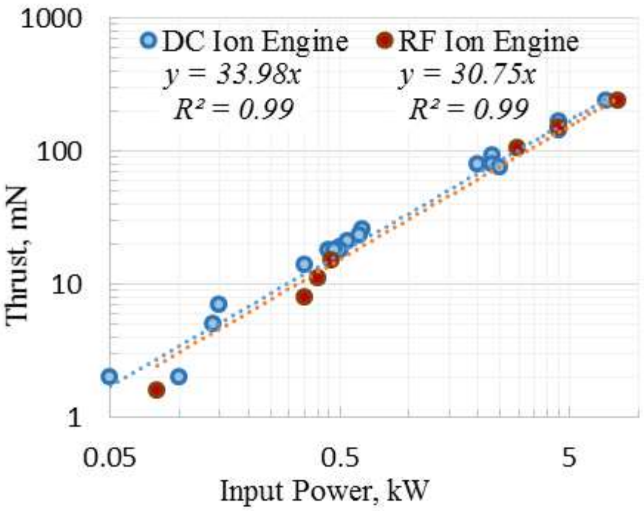

Figure 2.2: Log-log plot of thrust versus input power for Ion Engines.

Table 2.5: Average thrust-to-power values for ion engines surveyed

Thruster Architecture	**Average of thrust-to-power T/P_{in}, mN/kW**	**Standard Deviation, mN/kW**
DC Ion Engine	36.7	5.5
RF Ion Engine	28.7	5.6

the thrust-to-power ratio over all systems in each subtype gives equal weighting to all input powers and produces slightly different results. The averages and standard deviation for each system are given in Table 2.5. Although the relationship between thrust and power is quite linear, the standard deviation is between 15% and 20% of the average value. Thus, the linear relationship revealed in Fig. 2.2, does not mean thrust-to-power is invariant for any architecture, only that it is similar across thruster manufacturer and operating power level.

In contrast to thrust, Fig. 2.3 (semi-log scale) indicates that the demonstrated specific impulse increases nonlinearly with input power. A logarithmic best fit line is used to model the trending, which again is found to depend on thruster architecture. The differentiation by architecture is somewhat surprising as both systems employ an electrostatic grid system to accelerate the ions. It is observed that there is significant variation among different systems, especially those operating near 500 W. Three different technologies, the BRFIT-7, the IT-100, and NEXT, are highlighted near the 500 W operating point. The BRFIT-7 and IT-100 report the highest specific impulse of their respective subtypes. For the NEXT thruster, this data point falls at the lower limit of its operating range. The NEXT Isp approximately triples over its operating range, reaching 4000 s at 7.2 kW. These data points are highlighted to emphasize the variation in Isp possible for an individual thruster. The highest Isp demonstrated below 10 kW was 5400 s by the ESA-XX thruster below.

The thrust and specific impulse together determine the overall thrust efficiency as given in Eq. 2.8. DC ion engines operate at higher thrust-to-power while RF ion engines operate at higher specific impulse and thus the architectures achieve comparable thrust efficiencies. This result exemplifies the trade between thrust-to-power and Isp at constant thrust efficiency. Below 500 W, more efficient DC thrusters have been developed, and at high powers (around and above 5 kW) the RF thrusters have performed better. Around 500 W, there is no clear distinction in performance between the two systems, with thrust efficiencies for both bounded between 30% and 60%. However, because both architectures follow approximately the same trend in efficiency versus input power, only one trendline has been provided for the combined datasets in this case. An exponential fit that asymptotes to unity for large input powers is applied. The highest efficiency thrusters are labeled in Fig. 2.4.

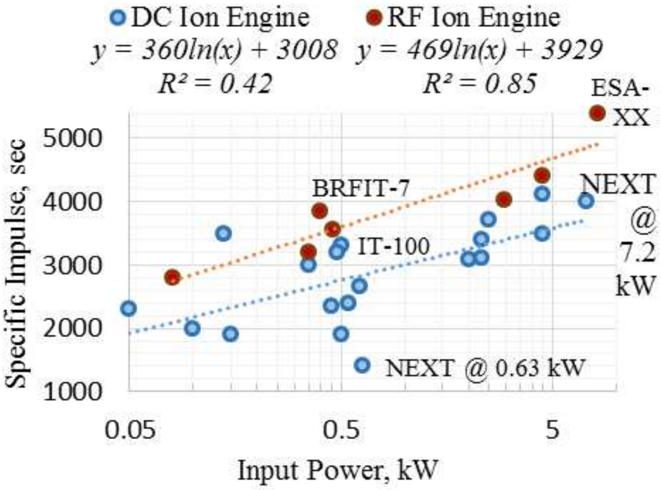

Figure 2.3: Semi-log plot of specific impulse versus input power for ion engines.

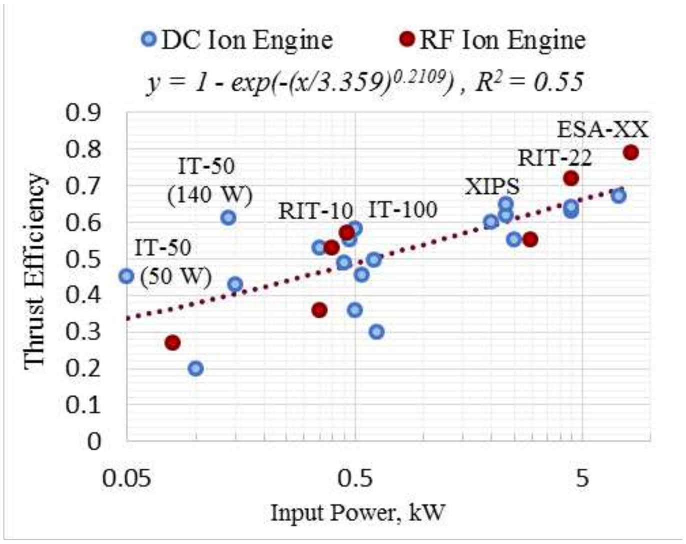

Figure 2.4: Semi-log plot of thrust efficiency versus input power for ion engines.

The linear relationship between thrust and power indicates that efficiency should be proportional to specific impulse within each ion engine subtype. Reported efficiencies are plotted against specific impulse in Fig. 2.5. It is apparent that there is a positive correlation between the two variables within the range of Isp values reported. Lines of best fit that capture trends in the survey data are provided for each subtype.

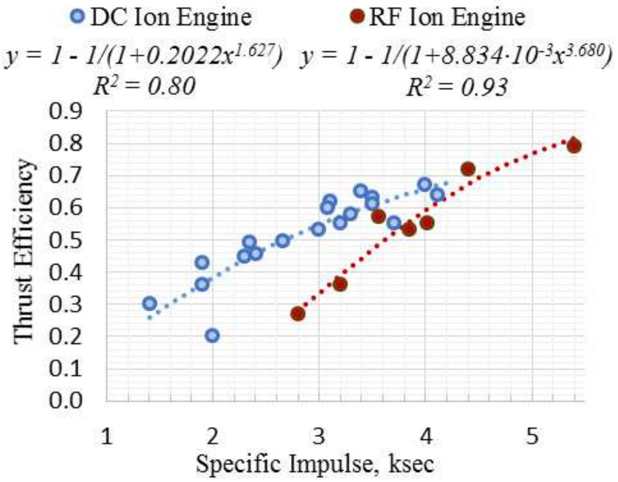

Figure 2.5: Thrust efficiency as a function of specific impulse for ion engines.

The survey data results are compared to detailed NEXT thruster data to aid in interpretation. The trends observed for thrust, specific impulse, and thrust efficiency as a function of input power across the many thrusters in this survey agree with those of the NEXT thruster over its operating range. The throttle table values for thrust and specific impulse reported in [35] are plotted and compared against DC ion engine best fit lines from the survey data in Fig. 2.6. It can be seen from Fig. 2.6(a) that for any given mass flow rate, the thrust-to-power ratio varies with input power, but the linear trendline for the aggregate data over all mass flow rates closely matches that for all DC ion engines in this survey. An explanation for the linear trending can be deduced from the NEXT results. Increases in input power are associated more with increases in mass flow rate than specific impulse. For any constant mass flow rate, the ratio of thrust-to-input power does change with specific impulse. However the range of specific impulses (and thus thrust-to-power ratios) is relatively constant across the range of mass flow rates. The increases in mass flow rates are accompanied by proportional increases in input power, keeping the thrust-to-power ratios relatively constant. It is expected that the same result holds for thrusters of different origins because they are constrained to similar Isp limits and can obtain similar efficiencies for a given Isp ($T/P = 2\eta/u_e$). The trendline for specific impulse versus input power (Fig. 2.6(b)) overpredicts the average NEXT Isp at the lowest powers (and low mass flow rates) but slightly underpredicts for all other values. Thus it is further cautioned that the trendlines given above for the survey data represent generally demonstrated values at any given operating point, while each individual thruster may have its own equivalent curves.

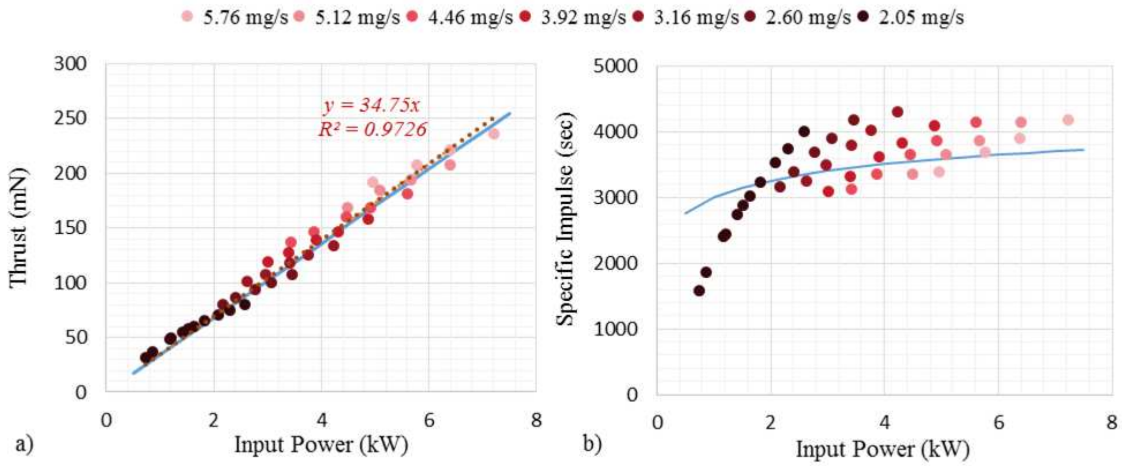

Figure 2.6: Comparison of the NEXT thruster thrust and specific impulse profiles with survey fit lines.

2.4.2 Hall Thrusters and Hybrid Designs

Like the ion engine, the Hall thruster has a strong history of development and flight experience. Hall thrusters were first flown in the early 1970s by the Russian space agency [11]. Since that time, Hall thrusters have become integral to the space industry, particularly in the commercial sector for stationkeeping of communications satellites. In comparison to ion engines, Hall thrusters typically have higher thrust densities (thrust per unit area) at the expense of reduced specific impulse. There have been two dominant Hall thruster designs, the *stationary plasma thruster* (SPT) and *thruster with anode layer* (TAL), which are both described briefly below. Others are experimenting with open cylindrical discharge chambers to reduce wall losses at smaller power and size scales. The performance of these systems is included in this survey but it is acknowledged that they are early laboratory prototypes.

The SPT design employs an annular discharge chamber and an external cathode at the discharge exit. The annular anode surface is near the front of the chamber along with the propellant inlet. Electrons released from the cathode accelerate toward the anode surface and generate the plasma via collisions with neutral gas. A radial magnetic field is established near the downstream edge of the discharge chamber that magnetizes electrons and impedes their axial transport. The trapped electrons drift azimuthally due to the combined effects of the electric and magnetic fields, forming the Hall current. The ions, largely unaffected by the magnetic field, are accelerated through the potential difference sustained across the discharge channel and form the exhaust beam. The positive ion beam is neutralized by electrons leaving the cathode at the exit plane. Because the Hall thruster has no region of isolated charge, there is no space charge limit on the thrust density of the system. However, because the ionization and acceleration both occur across the discharge channel, the need to keep potentials low enough for efficient plasma production limits the specific impulse of the system. Like ion engines, modern Hall thrusters predominantly employ xenon as the propellant, though there is interest in alternative propellants. A semi-empirical model of performance scaling using different propellants is explored in [56]. The thrusters in this survey are not delineated by propellant type. Hall thruster principles of operation and geometry are depicted in Fig 2.7.

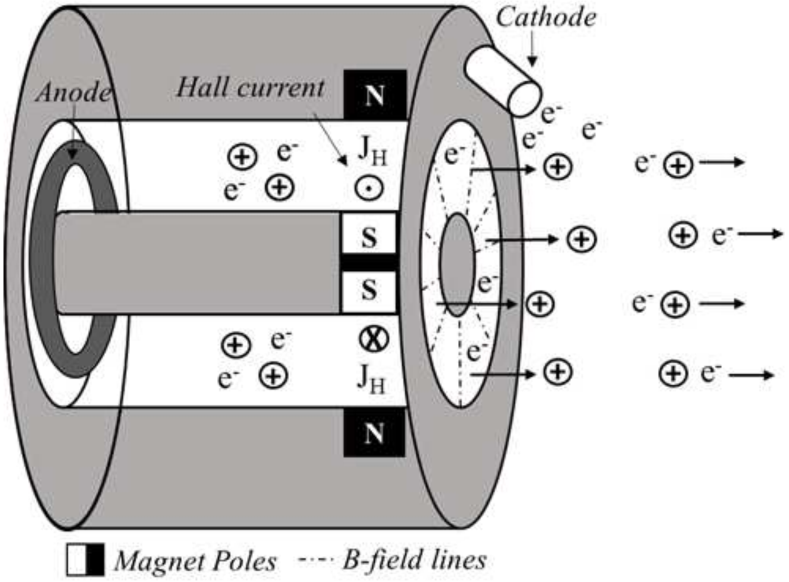

Figure 2.7: Diagram of a Hall thruster depicting conventional geometry and operation.

The TAL Hall thruster operates on the same basic principles as the SPT, but has slightly different physical characteristics. The TAL walls are metallic, which provide a different potential structure from insulating SPT walls. The TAL electric field accelerates the ions through a much smaller spatial region and thus allows for a shortened channel length. As with ion engine designs, a shorter channel length is desired to reduce wall losses. Despite their differences, both the SPT and TAL can be considered traditional Hall thruster designs. Each remains in production today and some hybrid SPT/TAL designs exist as well [57].

Several thruster concepts employ traditional Hall thruster principles but differ in ways that warrant discussion. For example, cylindrical Hall thrusters were designed to improve efficiency by eliminating losses to the inner wall in the annular configuration. These thrusters are typically geared at low power (sub-kW) operation, where the effects are most pronounced [58]. In cylindrical Hall thrusters, a magnetic core is typically still present but is severely shortened so that the chamber is largely open. The shortened core results in an axial magnetic field established closer to the front wall of the discharge chamber and a cusped component is added near the exit to impede electron transport. Other concepts, such as the "High Efficiency Multistage Plasma Thruster", or HEMPT [59], have implemented drastic changes to magnetic field topology. These fields result in different electron interactions and ion acceleration regions. The performance of sufficiently developed examples are included in this survey.

A list of the Hall thrusters considered in this study is presented in Table 2.6. The developer, level of maturity, and references for performance data are also included for each thruster. Where possible, thrusters are classified by subtype. The design details for some commercial thrusters are not available. Again, the technology maturation is listed representing the state of the technology when the referenced performance data was published.

The performance data for Hall thrusters gathered from the references listed above are plotted versus input power in Fig. 2.8, Fig. 2.9 and Fig. 2.10. The general trends are the same as observed for ion engines. The plot of thrust versus input power is again used to obtain a representative thrust-to-power ratio for the systems developed. The annular (SPT/TAL) systems have a higher ratio (54 mN/kW) than cylindrical systems (33 mN/kW) as given by the slope of linear fit lines.

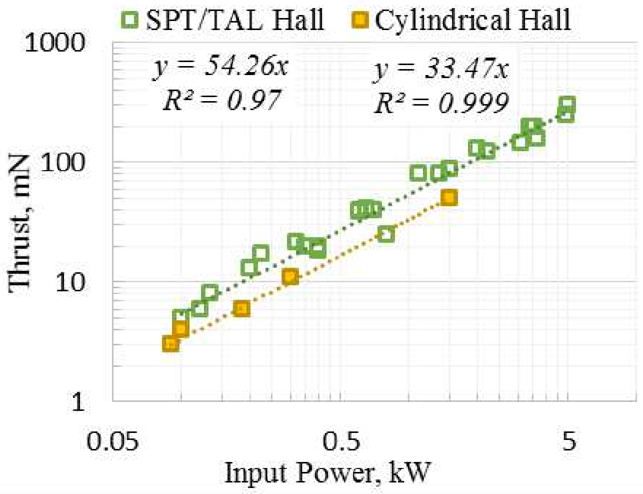

Figure 2.8: Log-log plot of thrust versus input power for Hall thrusters.

As with ion engines, the thrust-to-power ratios from linear fit lines are compared with the averaged values for the datasets. The average and standard deviation of the thrust-to-power ratio for each Hall thruster architecture is provided in Table 2.7. Again, despite a very linear trend, significant standard deviations of 17% and 9% are found for the thrust-to-power ratios within the SPT/TAL and cylindrical subtypes, respectively. Thus like ion engines, the thrust-to-power ratio of Hall

Table 2.6: Hall Thrusters surveyed

Thruster Name	Model	Developer	Thruster Type	Technology Maturation	Ref.
BHT	200	Busek	Annular	Flight	[60, 61]
	600			Developed (Current)	
	1000			Developed (Current)	[61]
	8000			Developed (Current)	[62]
BPT (XR)	2000	Aerojet	Annular	Developed (Current)	[63, 64]
	4000 (5)			Flight	
CHT	28 mm	KAIST	Cylindrical	R&D Prototype	[65]
	40 mm				
	50 mm				
CHT	2.6 cm	NASA / Princeton PPPL	Cylindrical	R&D Prototype	[58, 66]
	9 cm				
HiVHAc	–	NASA / Aerojet	SPT	Developed (Current)	[67, 68]
HEMPT	–	Thales	Cylindrical	Developed (Current)	[59]
HT	100D	ESA / Alta	SPT	Developed (Current)	[69]
	400				[70]
PlaS	40	Russia / Fakel	Hybrid (SPT/TAL)	Developed (Current)	[57, 71]
PPS	1350-G	SNECMA	SPT	Flight	[70, 72, 73]
ROS	200	ESA / Alta / Astrium	Annular	Developed (Current)	[57, 71]
SPT	1	Russia / Fakel	Hybrid (SPT/TAL)	Flight	[74]
SPT	50	Russia / Fakel	Annular	Flight	[11, 42, 75]
	70				
	100				
	140				
T	40	Pratt & Whitney / Aerojet	Annular	Developed (Current)	[76]
	140				
TCHT	3B	Osaka University	Cylindrical	R&D Prototype	[77, 78]

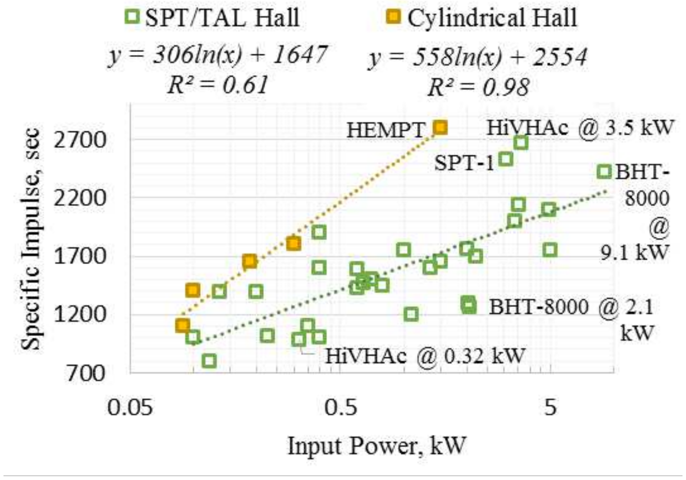

Figure 2.9: Semi-log plot of specific impulse versus input power for Hall thrusters.

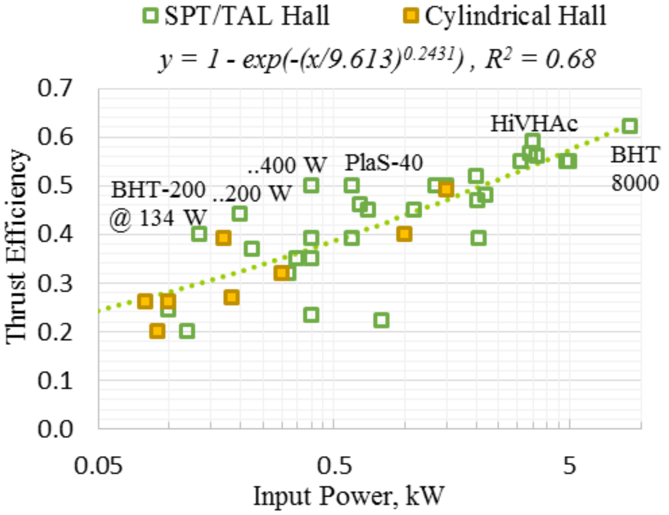

Figure 2.10: Semi-log plot of thrust efficiency versus input power for Hall thrusters.

thrusters will vary with the exact operating conditions about some average value. There may be more spread in the observed Hall thruster values as the beam current and specific impulse are more closely coupled than in ion engines, which have separate ionization and acceleration potential gradients.

While the annular thrusters provide higher thrust at a given power, the cylin-

Table 2.7: Average thrust-to-power values for Hall thrusters surveyed

Thruster Architecture	**Average of thrust-to-power T/P_{in}, mN/kW**	**Standard Deviation, mN/kW**
SPT/TAL Hall Thruster	57.2	9.8
Cylindrical Hall Thruster	35.2	3.2

drical thrusters have been able to achieve significantly higher specific impulse. The highest specific impulse is 2800 s, provided by the HEMPT thruster operating at 1500 W. The SPT-1 and HiVHAc thrusters are also well above the trendline for their subtype. At the upper limit of their power ranges, the HiVHAc and SPT-1 have an Isp of 2665 s and 2533 s, respectively. At the lower end, the Isp values drop to 981 s and 1424 s, respectively, with the HiVHAc spanning a wider power range.

Like ion engines, the constant thrust-to-power ratios coupled with nonlinear increases in Isp result in nonlinear increases in thrust efficiency for Hall thrusters over the input powers considered. Though cylindrical thrusters have been proposed to improve performance at low power levels, it is clear that they have not surpassed traditional systems. The BHT-200 thruster is well above the average performance at sub 500 W power levels, achieving between about 40% and 50% efficiency. The highest Hall thruster thrust efficiency, 59%, is reported by the HiVHAc at 3.52 kW. It is interesting to note that the HiVHAc can be throttled up from this point to 3.66 kW for high Isp operation (as highlighted above), but its overall thrust efficiency drops in the process. Similar relationships were found between the Hall thruster survey data and HiVHAc throttle tables as between DC ion engine survey data and NEXT throttle tables (see Fig. 2.6 and related discussion).

A positive correlation between specific impulse and thrust efficiency is shown in Fig. 2.11, though SPT/TAL efficiencies appear to level-off or even decrease beyond 2000 seconds. Thus again, best fit lines are provided and are applicable across the range of survey data for each thruster subtype. Because physical mechanisms are expected to contribute to decreased Hall thruster efficiency at higher specific impulses, these trends should not be extrapolated outside of the present range. Again it is cautioned that the performance of any individual thruster across its operating range may deviate from the survey data trends.

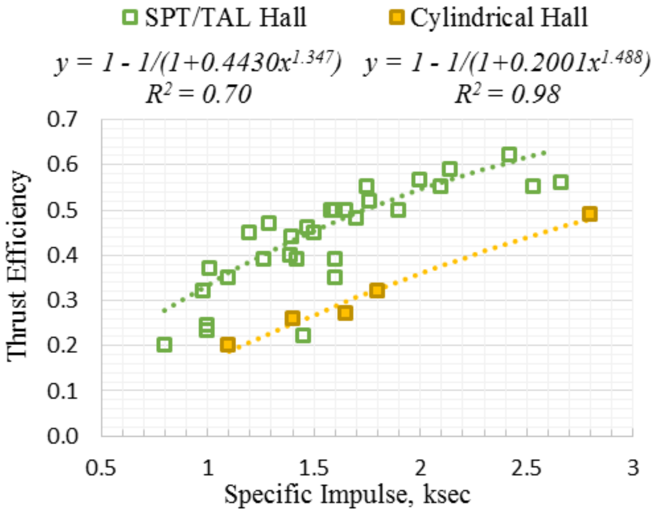

Figure 2.11: Plot of thrust efficiency versus specific impulse for Hall thrusters.

2.4.3 Helicon Thrusters

Although helicon thrusters are much less developed than ion engines and Hall thrusters, they are expected to achieve theoretically comparable thrust and specific impulse, and operate over the power ranges of interest for this survey. Helicon plasma sources were discovered in the 1960s but the benefits they offer in ionization efficiency were not well known until the 1980s. Since then, interest in helicon plasma generators has grown because they are known to produce plasma densities that are an order of magnitude higher than traditional sources for the same input power. Helicon sources were proposed for use in EP systems with the hope that a higher propellant ionization fraction would translate into a higher thrust efficiency.

Due to the nature of their operation, helicon thrusters could offer advantages over existing EP technologies, such as ion engines and Hall thrusters, including:

1. Higher plasma densities by an order of magnitude: high propellant utilization fraction, high thrust efficiency
2. No grids or electrodes immersed in plasma environment: circumvents life-limiting erosion of components, may result in longer operational lifetimes
3. Exhaust beam is composed of equal concentrations of ions and electrons: does not require external beam neutralizer, introducing additional power and mass savings
4. Amenable to a wide range of propellants: includes gases that could be harvested throughout the solar system for refueling and propellants more easily storable than noble gases (e.g. water vapor)

A helicon source is a type of RF plasma generator that incorporates an axial magnetic field to confine electrons and support propagation of circularly-polarized low frequency "helicon" waves [79]. A stand-alone helicon thruster consists of a quartz glass tube wrapped in a copper helical antenna, enclosed by an outer tube and an axial magnetic field source (e.g. solenoid or Hemholtz coils, not pictured), and with one end open to allow the exhaust to escape (see Fig. 2.12). The ions are presumed to be accelerated across a plasma sheath that forms at the exit, which alleviates the need for internal acceleration grids. Some authors have noted the formation of a "current-free double layer" outside of the thruster exit plane with an accelerating potential larger than that of a traditional, single-layer sheath [80]. The presence and properties of naturally forming acceleration mechanisms in these devices is still an area of active research and debate.

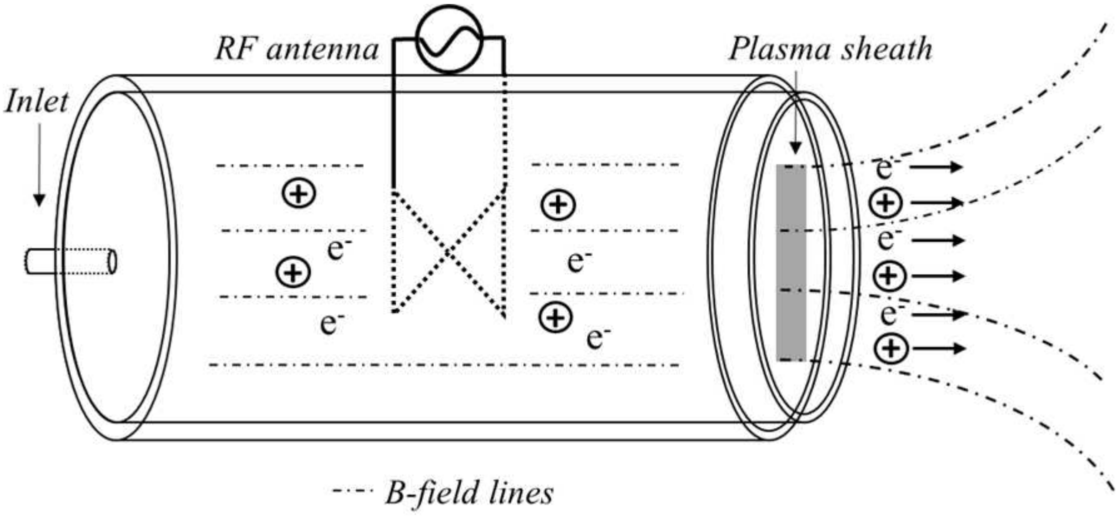

Figure 2.12: Schematic of helicon thruster geometry and operation.

Many protoype thrusters have been developed with varied downstream magnetic field profiles [81, 82]. While early work to describe the acceleration region was centered around free-standing and double-layer sheaths as reviewed in [83, 84] and described above, more recently the problem has been treated as supersonic plasma expansion in a diverging magnetic field [85, 86]. Despite their differences, these approaches roughly converge to predict ion acceleration approximately equal to that of a planar wall sheath, with the underlying mechanism rooted in steady-state current ambipolarity.

While several experimental helicon thruster prototypes have been developed to date, the technology is still yet to be flight demonstrated. In laboratory operation, helicon ion sources consistently achieve high plasma densities, up to 10^{13} cm^{-3} [87], but the efficiency in a thruster configuration is far from competitive with existing technologies. For example, Takahashi et. al. [82] have tested several iterations of helicon thrusters and most recently reported an overall efficiency of only 13.5% after modifying the downstream magnetic field structure. Williams and Walker [88] characterized a helicon thruster operating under standard conditions and reported an overall thrust efficiency of 1.4%, well below the 60-70% routinely seen in ion engines. They hypothesize that poor mass utilization and high beam divergence contribute to the inefficiency. Even if these issues were remedied, the authors predict a maximum efficiency of 30% and thus propose the addition of a secondary ion acceleration stage to achieve performance competitive with existing technologies.

Several authors have begun work to investigate the performance gains that can be achieved with the addition of an ion acceleration stage as was suggested in [82]. The VASIMR (Variable Specific Impulse Magnetoplasma Rocket) is an extremely large scale example of this concept that has undergone significant testing and development [89]. The VASIMR system employs a helicon ionization stage augmented

Table 2.8: Helicon Thrusters Surveyed

Thruster Name	**Research Group or University**	**Technology Maturation**	**Ref.**
HEAT	Japanese Collaboration	R&D Prototype	[92, 93]
HDLT	ANU, Surrey Space Center	R&D Prototype	[94]
HPH.com	EU Collaboration	R&D Prototype	[95]
mHT	MIT	R&D Prototype	[96]
PM-HPT	Tohoku Univ. & ANU	R&D Prototype	[82]
VASIMR (VX-10)	Ad Astra	Developed (Current)	[97, 98]
Lab model	Georgia Tech	R&D Prototype	[88]

with an ion cyclotron heating (ICH) acceleration stage that has achieved thrust efficiencies in excess of 70% [90]. However, this system was designed with the goal of transporting humans to Mars and thus operates at power levels several orders of magnitude higher than conventional EP systems (100 kW - MW versus 1-10 kW). On a moderate power scale (below 10 kW), other researchers have recently investigated more traditional ion acceleration mechanisms, such as adding an anode and cathode to create an electrostatic potential near the exit [91], to achieve high thrust efficiency at the expense of forfeiting "erosionless" operation. The performance gains realized from such a system are yet to be quantified.

The few helicon data points that have been obtained will be included in the performance comparison section and in the appendix. The systems considered are outlined in Table 2.8.

Additionally, a few analytically predicted thrust efficiencies are included for reference [99–101], though it is expected that unaccounted for loss mechanisms would make these a presently unachievable upper limit. It is important to note that helicon system operating powers and efficiencies often consider the RF input power only and ignore the power into electromagnets used to create the magnetic field. It is hypothesized that these fields could be generated with superconducting magnets at negligible power cost.

2.5 Performance Comparison

The data presented for each technology individually in the preceding section is combined and compared to deduce trends across thruster type. This comparison allows one to assess the broad state of the art for all systems that may enable near-term deep space missions under current cost and power constraints. The demonstrated performance is assessed against mission needs detailed in Section III. For example, mission designers relying on REP asserted a need for thrusters that operate at efficiencies in excess of 65% below 3 kW. Those proposing missions with SEP desire high efficiency up to 5 kW, and require a wide operating range.

In Fig. 2.13, the thrust efficiency, specific impulse, and thrust are shown as a function of input power for all thrusters surveyed. Some of the systems that have demonstrated the highest thrust efficiencies at each power level are labeled in Fig. 2.13(a). As expected, the highest efficiency systems are generally ion engines, with both DC and RF systems present on the front. From Fig. 2.13(b), the presently achievable specific impulses are presented and are found to be clearly delineated by thruster architecture. From Fig. 2.13(c), it is clear that Hall thrusters provide the highest thrust-to-power output, with other systems following in the reverse order as specific impulse. The trends in thrust and specific impulse combine so that the thrust efficiency is not so clearly delineated by thruster type, with ion engines having only a slight edge. It is obvious that helicon thrusters will need significant development and improvement before they will be competitive with state of the art systems at these power levels. Even the analytically predicted thrust efficiencies, shown with the “x” markers, fall on or below the performance curve at best. It remains to be seen if implementing secondary acceleration stages can raise thrust efficiencies to competitive levels, as the VASIMR system has achieved at the 100 kW power scale.

Presently, there are no systems that exceed 65% thrust efficiency below 3 kW. The only system that exceeds this metric below 5 kW is the RIT-22 ion engine, achieving 72% efficiency at 4.5 kW. Its range of operation and performance variation with power are not known. There are many thrusters that have operated at or near the 500 W input of interest to REP missions. The thrust efficiencies near this operating point are varied, ranging from about 20-60%. Ion engines have achieved the highest thrust efficiency near 500 W, though Hall thrusters are not far behind. For example, the BHT-200 demonstrated 50% efficiency at 400 W. Systems such as NEXT and NSTAR may not demonstrate the highest efficiency at any one power level since they have been designed to operate over a wide range of input power. For reference, the NEXT thruster has a thrust efficiency of 30% at 0.62 kW and 67% at

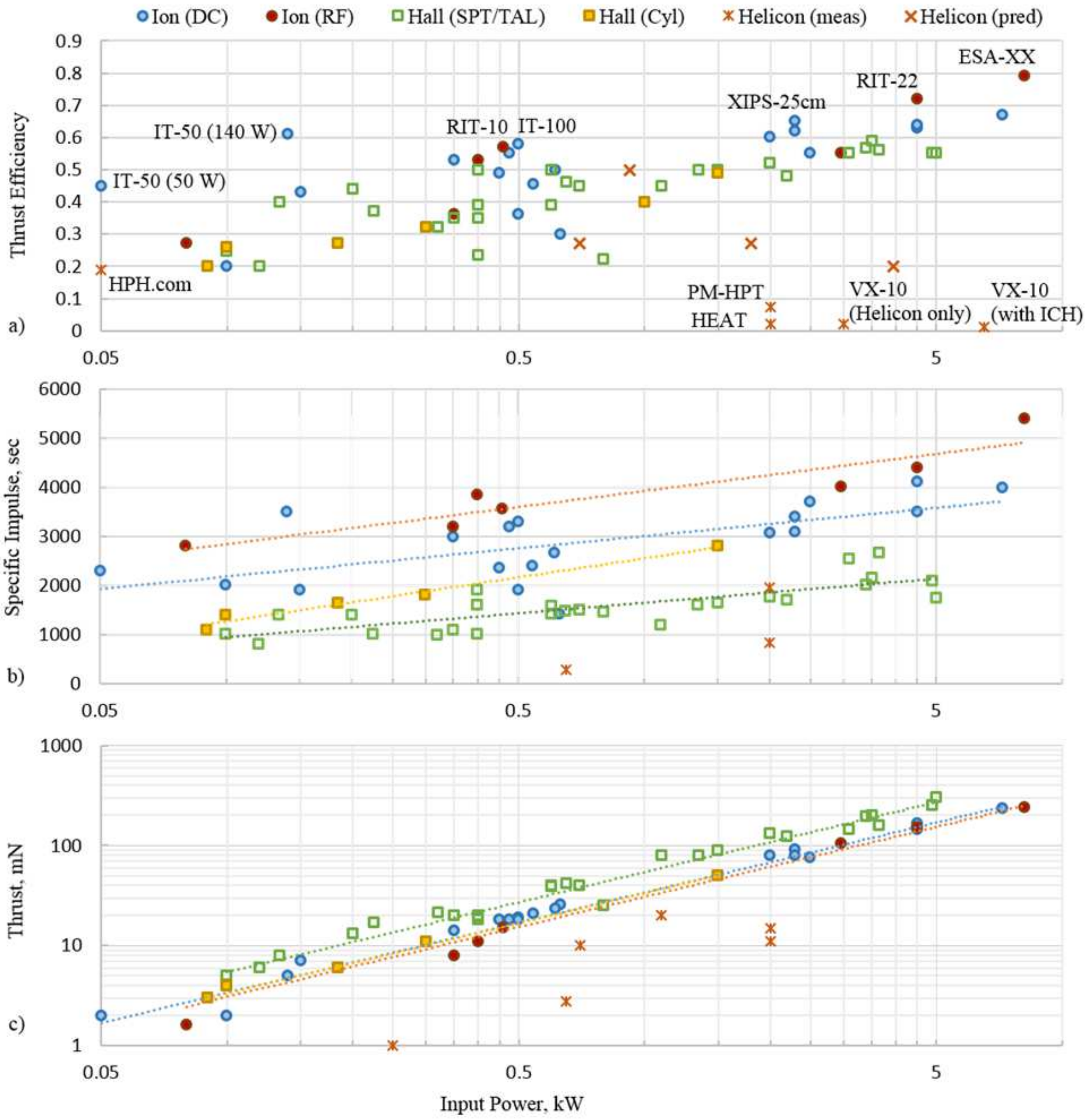

Figure 2.13: Plots of versus input power of a) thrust efficiency (semi-log), b) specific impulse (semi-log), and c) thrust (log-log) for all EP systems surveyed.

7.2 kW.

An alternate representation of the performance data is presented in Fig. 2.14 with thrust-to-power plotted against specific impulse for all of the systems surveyed. Lines of constant efficiency are also included. If an optimal specific impulse has been determined for a mission or maneuver, it is straightforward to compare the systems which meet that requirement. For maneuvers which require a specific impulse below 3000 seconds, annular Hall thrusters emerge as the clear choice, provided the input power is greater than 100 W. Many deep space exploration missions have an optimal specific impulse in excess of 3000 seconds and thus would be better suited to adopt ion engines in their architectures.

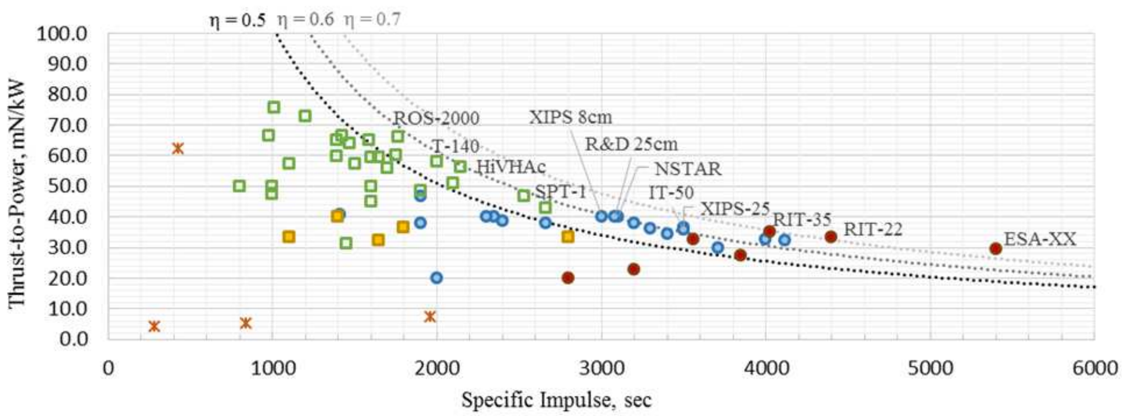

Figure 2.14: Plot of thrust-to-power versus specific impulse for all EP systems surveyed.

2.6 Summary

An extensive survey of the state of the art in moderate power electric propulsion systems is presented. In contrast to previous surveys, this study organizes detailed performance data for a subset of the broad field of EP, directed at a specific mission application. All EP systems that satisfy the requirements of near-term REP and SEP deep space exploration missions are included. A review of previous and proposed EP enabled exploration missions was performed to constrain the survey. It was concluded that thrusters must operate between approximately 0.1 and 10 kW and produce mN level thrust and an Isp on the order of 1000 seconds. The types of systems that meet these requirements are ion engines, Hall thrusters, and helicon thrusters. It is acknowledged that the former two systems are much further developed than the latter.

It is found that thrust, specific impulse, and thrust efficiency increase with input power for all developed systems. For both ion engines and Hall thrusters, thrust increases linearly with input power, and thus logarithmic increases in specific impulse are mirrored in thrust efficiency trends. Averaged thrust-to-power ratios for each thruster subsystem are 54 mN/kW for annular Hall thrusters, 33 mN/kW for cylindrical Hall, 34 mN/kW for DC ion engines, and 31 mN/kW for RF ion engines. Ion engines demonstrate the highest thrust efficiencies across input power, though differences in thrust efficiency are not at clear as in thrust and specific impulse, individually. For missions optimized with specific impulse below 3000 seconds, Hall thrusters provide the most efficient operation, provided that the input power is sufficiently high. For a desired specific impulse above 3000 seconds, which is more common to deep space exploration, both DC and RF ion engines achieve efficiencies between 60 and 70%. For all thruster types, this survey indicates there is room for performance improvement at power levels below 3 kW, which will benefit both SEP and REP missions. All performance data collected for this survey and accompanying references are included in Appendix A.

Chapter 3: Single Stage Performance Analysis

3.1 Overview

This chapter has been published in the *Journal of Propulsion and Power* according to the following citation. At the time of this thesis publication, it has been cited 6 times!

Petro, E. and Sedwick, R.,
Effects of Water-Vapor Propellant on Electrodeless Thruster Performance,
Journal of Propulsion and Power, Vol. 33 (6), 2017.
`https://doi.org/10.2514/1.B36389`

The performance of an electrodeless thruster operating on water vapor propellant is evaluated and compared to noble gas propellants. Cross-section data for electron interactions with water molecules are employed to predict the ionization cost as a function of electron temperature. The ionization cost model incorporates energy loss mechanisms such as dissociation and excitation of rotational modes that are not present for noble gas propellants. The ionization cost for water is compared to that of traditional noble gas propellants, such as argon. The characteristics of a water vapor plasma sheath are discussed and incorporated, along with the ionization cost, into an overall thrust efficiency analysis.

Nomenclature

A = cross-sectional area, m^2

B_0 = constant axial magnetic field, T

e = elementary charge, C

E_c = ionization cost, eV

E_{ICH} = ICH energy, eV/amu

E_j = electron energy lost in j^{th} electron-neutral interaction, eV

g = acceleration due to gravity at Earth's surface, m/s^2

Γ = particle flux, m^2/s

Isp = specific impulse, s

k = Boltzmann constant, J/K

κ = reaction rate constant, m^3/s

m_e = mass of an electron, kg

m_{H_2O} = mass of a water ion/neutral, kg

n_e = number density of electrons, $particles/m^3$

n_i = number density of (positive) ions, $particles/m^3$

n_{i-} = number density of negative ions, $particles/m^3$

n_n = number density of neutral particles, $particles/m^3$

n_0 = bulk plasma density, $particles/m^3$

R_m = magnetic mirror ratio, B/B_0

ϕ = electrostatic potential, V

σ = cross-section, m^2

θ_{cr} = half-angle of particle loss-cone in velocity space, $radians$

T = thrust, N

T_e = electron temperature, eV

T_{i-} = negative ion temperature, eV

u_e = exit velocity, m/s

v = velocity, m/s

v_b = Bohm velocity, m/s

3.2 Introduction

While other researchers have demonstrated that water vapor can be relatively easily ionized with a helicon source [102,103], the theory behind operation is incomplete. Thus we have developed a water vapor ionization model that predicts plasma characteristics such as the molecular composition and energies of ions created as a function of the electron energy. These plasma characteristics determine the achievable thrust and specific impulse. The predicted plasma composition and energy loss mechanisms are incorporated into a power balance analysis to predict thruster efficiency. In Section II, we derive model assumptions with a comprehensive literature review and calculations specific to water vapor. In Section III, these assumptions are implemented in a zero-D model to predict thruster performance. While most of what is presented is applicable to any electrodeless thruster with magnetic expansion, much of the referenced work draws from helicon research. In comparison to the thruster modeling framework presented in [8], the present work seeks further insight into the dominant processes in a water vapor discharge that will impact thruster performance. Additionally, while other authors have developed quasi-1D [86] and 2D [101] performance models for electrodeless thrusters, a zero-D model is sufficient for the present purpose of comparing the operation with a molecular propellant to a noble gas propellant. The framework developed in the aforementioned models could be readily adapted to a molecular propellant such as H_2O using the appropriate collision frequencies and the ionization costs presented in Section II of this paper.

3.3 Characteristics of a Low Temperature Water Vapor Plasma

A water vapor plasma differs significantly from a noble gas plasma. In a noble gas plasma, electron collisions will result in either elastic scattering, ionization, or electronic excitation. In a water vapor plasma, many more electron-molecule interactions must be considered. For example, water molecules may dissociate into component molecules and dissociated species may form both positively and negatively charged ions, which will affect the plasma characteristics. In considering water vapor as an alternative propellant, several key questions arise and are answered through this analysis. We seek to understand:

1) How does the presence of negative ions (H^-, O^-, OH^-) affect the operation?

2) What are the properties of a plasma sheath with multiple positive (and negative) ions?

3) Can water vapor be ionized as efficiently as traditional propellants?

These questions are critical for predicting the thrust efficiency of an electrodeless thruster operating with water vapor. The assumptions employed in this study may also be applicable to other oxygen containing molecular propellants such as N_2O and CO_2. In this section, a review of the plasma literature pertinent to each of these questions is presented, along with conclusions drawn for a low-temperature, low-pressure plasma.

3.3.1 Impact of Negative Ions

Plasmas containing sufficiently high populations of negative ions are referred to as electronegative and are still an area of active research [104, 105]. A water vapor plasma supports the production of negative ions through dissociative attachment electron-ion collisions. The production of negative ions is of interest because they could alter the steady-state accelerating potential in the magnetic nozzle or represent a loss mechanism if trapped in the bulk. At low electron temperatures, the cross-sections for the production of negative ions far exceed those for positive ions [106]. Using these cross-section data, the rate constants, κ, for electron interactions are calculated for a Maxwellian electron population according to Eq. (3.1).

$$\kappa = \langle \sigma(E_e) v(E_e) \rangle = \sqrt{\frac{8e}{\pi m_e T_e^3}} \int_0^\infty E_e \sigma(E_e) e^{-\frac{E_e}{T_e}} dE_e \tag{3.1}$$

where m_e is the electron mass and $v(E_e)$ is the electron velocity.

The rate constants for plasma (electron) temperatures between 1 and 10 eV are given in Fig. 3.1. The lines representing each species are labeled at the right-hand border of the figure. For low pressure discharges, H_2O^+ is predicted to be the dominant positive ion. The discharge becomes strongly electropositive around 3 eV. From this calculation it is predicted that negatively charged ions (mainly H^-) will readily form at plasma temperatures below 2 eV. However, quasi-neutrality must still be satisfied ($n_i = n_{i^-} + n_e$) globally. For temperatures of 3 eV and above, the production of negative ions quickly becomes negligible in relation to positive ions. For reference, electron temperatures between 1 and 10 eV are typical for helicon plasmas [107, 108] and similar or even higher temperatures may be possible in ECR discharges [109].

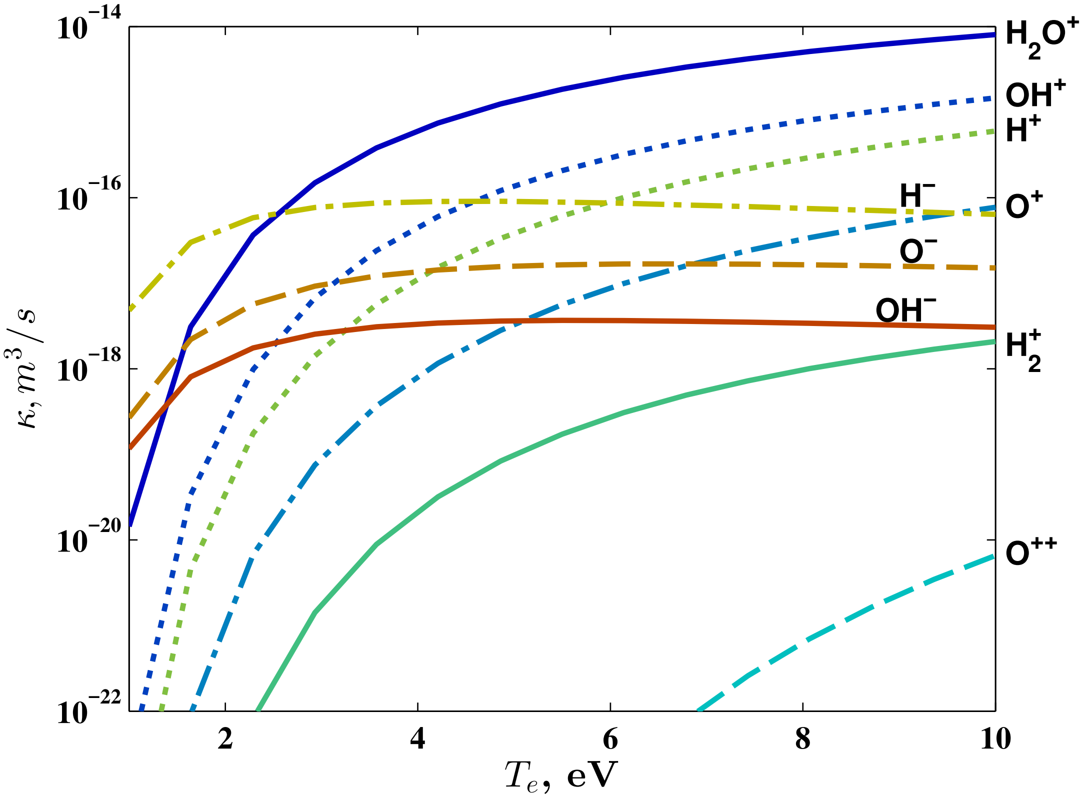

Figure 3.1: Rate constants, $\kappa = \langle\sigma(E)v(E)\rangle$, for ions generated in a water vapor plasma as a function of electron temperature.

Although cross-section data suggest that negative ions readily form at low electron temperatures, there is both theoretical and experimental evidence to suggest that they may not have a significant impact on thruster operation. Numerical simulations [105, 110, 111] and experimental observations [112] of low-temperature electronegative plasmas indicate that negative ions will remain trapped in the center of the plasma due to their inability to traverse sheath potentials that form near the wall. Assuming the potential structure keeps negative ions confined to the center of the plasma, the generation rate will be balanced by the rate lost via electron detachment *(e + A^- → A + e + e)* resulting in a steady-state population [113]. The particle balance principle employed in plasma coronal equilibrium models [114] can be used to determine the steady-state ratio of negative ions to neutral molecules. In steady state, neglecting ion-ion recombination at electron temperatures on the order of 1 eV or higher, the negative ion particle balance is given by Eq. (3.2), with detachment being the dominant loss process.

$$\frac{dn_{i-}}{dt} = n_e n_n \langle \sigma_{attach} v \rangle - n_e n_{i-} \langle \sigma_{detach} v \rangle = 0 \tag{3.2}$$

Thus, the steady-state ratio of negative ions, n_{i-}, to neutral molecules, n_n, is given by Eq. (3.3), where both the numerator and denominator vary with electron temperature.

$$\frac{n_{i-}}{n_n} = \frac{\langle \sigma_{attach} v \rangle}{\langle \sigma_{detach} v \rangle} \tag{3.3}$$

Using the cross-section data given in [106], this ratio is calculated and plotted (Fig. 3.2) for the plasma temperatures of interest. It is found that the negative ion population should remain less than 1 part in 1000 of the neutral population. If a resonant wave heating mode can be achieved for water vapor, as has been demonstrated with argon in helicon sources, positive ion fractions exceeding 1 part in 10 are possible [87]. Thus, it is assumed for this analysis that the water vapor plasma can be modeled as electropositive with the negative ions confined to the interior of the plasma and contributing only as an energy loss mechanism.

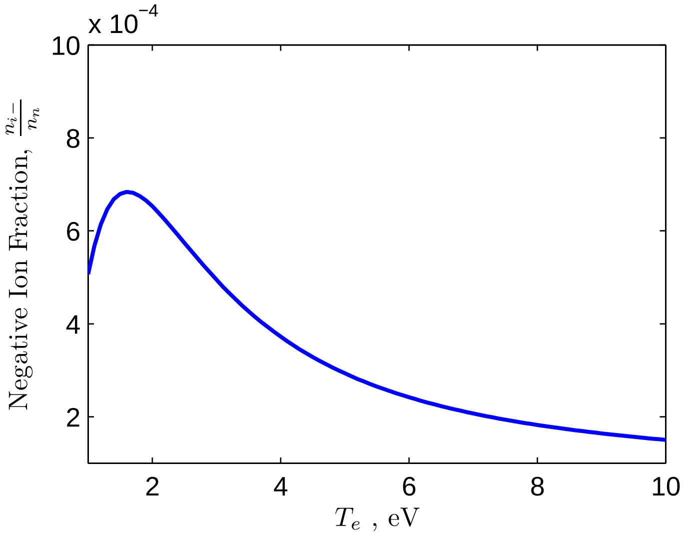

Figure 3.2: Steady-state ratio of negative ions to neutral particles as predicted by the particle balance model (Eq. (3.2)).

3.3.2 Plasma Sheath Properties

There has been considerable theoretical investigation into the effect of multiple positive ion species and negative ion species on sheath formation and characteristics [115]. For electronegative plasmas, the sheath potential is a function of the electronegativity, $\frac{n_{i-}}{n_e}$, and the negative ion to electron temperature ratio $\frac{T_{i-}}{T_e}$ [116]. For sufficiently low values of each, an electropositive sheath forms and negative ions are confined. This theoretical result agrees with experiments cited in the previous section. Per the assumption that negative ions do not contribute to sheath formation processes, the question is reduced to the effect of multiple species of positive ions (i.e. $\mathrm{H_2O^+}, \mathrm{H^+}, \mathrm{O^+}$) on the sheath characteristics. The multi-species electropositive sheath Bohm velocity, v_b, is not constrained to a unique solution, but two interesting results are possible [117]; each species is either accelerated to its own sound speed, or to a system averaged sound speed across the pre-sheath region. The latter result has been observed experimentally even at low pressures [118] when population densities of each ion species are comparable. However, another group [119] showed that if one species far outnumbers another ($\frac{n_1}{n_2} \gg 1$), the former result prevails wherein each species travels at its own sound speed ($v_{b,i} = c_{s,i} = \sqrt{\frac{T_e}{m_i}}$). In addition to affecting particle fluxes to the walls, it is generally assumed the plasma flux out of the exit of electrodeless thrusters is given by $\Gamma = 0.5 n_0 v_b$, where n_0 is the bulk plasma density [99]. Thus, the relative populations of positive ions in an H_2O plasma are needed to predict the Bohm velocity and thereby the exhaust characteristics.

The relative fractions of positive ions are predicted to first order using the generation rate constants for ions versus electron temperature (introduced in Section II(a) above). The relative population densities are predicted by assuming the flux of each species, Γ_i, out of a control volume is equal to its generation rate ($\Gamma_i = n_n n_e \langle \sigma_{ion} v \rangle = n_e n_n \kappa_i$). Recombination reactions that could result in different loss rates for each species are neglected for low pressures. The steady-state densities are thereby coupled to the loss rates through the sheath, but a self-consistent solution can be found for the latter case discussed above, with H_2O^+ ions far outnumbering all other positive ions. In this case, ion fractions for each species are a function of the relative generation rates and Bohm velocities as given by Eq. (3.4).

$$\frac{n_i}{n_{total}} = \frac{\frac{\Gamma_i}{v_{b,i}}}{\sum \frac{\Gamma_i}{v_i}} = \frac{\kappa_i \sqrt{m_i}}{\sum \kappa_i \sqrt{m_i}} \tag{3.4}$$

The ion fractions for the dominant positive species are shown in (Fig. 3.3) for

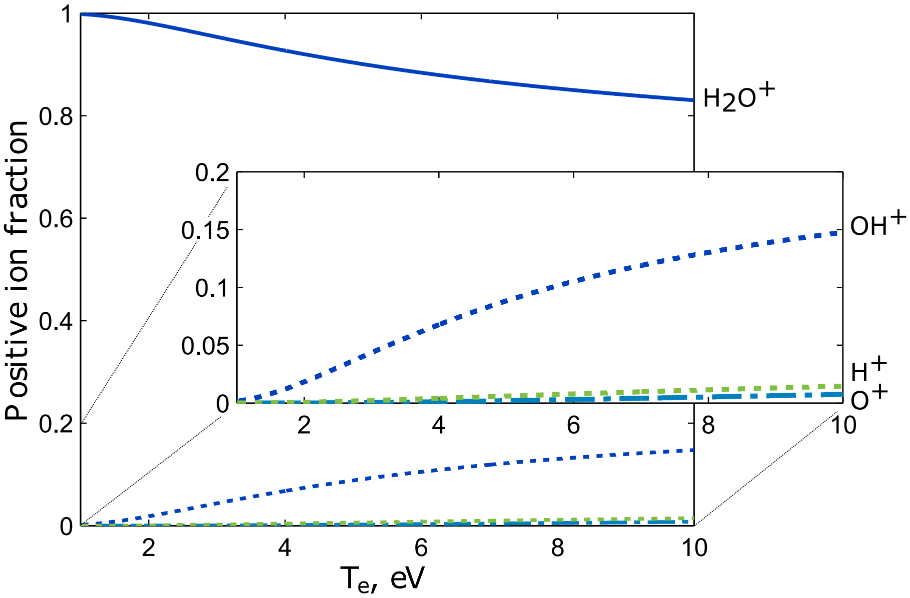

Figure 3.3: Distribution of positive ions in a H_2O plasma.

temperatures below 10 eV. H_2O^+ ions are found to comprise 83% or greater of the total positive ion population in this energy range. The next highest population is OH^+ ions, contributing up to 15% of all positive ions at 10 eV. Thus we assume that each species is accelerated to its individual sound speed. We conclude that the plasma sheath in a water vapor system is largely unaffected by additional ion species (both positive and negative) and reduces to the result for a single, species H_2O^+ plasma. Assuming the positive ions contribute the majority of the momentum transfer ($m_{H_2O^+} \approx m_{OH^+} \gg m_e$), a simple expression for thrust, T, is given by Eq. (3.5).

$$T = m_{H_2O}\frac{n_0}{2}v_b u_e A_0 \tag{3.5}$$

where u_e is the exit velocity, determined by the magnetic nozzle expansion, and A_0 is the constant cross-sectional area before expansion, which determines the mass flow rate out of the thruster. There is no electron pressure term as the electrons are assumed to cool in the expansion process [120].

As discussed in Section I, although many different models of the acceleration region exist, most predict ions gain energy approximately equal to that of a Debye sheath drop. Thus, the kinetic energy of the exhaust is given by Eq. (3.6) and the Isp is given by Eq. (3.7). Here, —$\Delta\Phi_{sh}$— represents the potential drop in both the downstream nozzle and at any closed boundaries upstream.

$$\frac{1}{2}m_{H_2O}u_e^2 = e|\Delta\Phi_{sh}| = \frac{1}{2}eT_e\left(1 + ln\left(\frac{m_{H_2O}}{2\pi m_e}\right)\right) \tag{3.6}$$

$$Isp = \frac{u_e}{g} = \frac{1}{g}\sqrt{\frac{eT_e\left(1 + ln\left(\frac{m_{H_2O}}{2\pi m_e}\right)\right)}{m_{H_2O}}} \tag{3.7}$$

When compared to argon, a water vapor exhaust beam will have a 43% higher Isp due to its lower molecular weight.

3.3.3 Ionization Cost

The ionization efficiency plays an important role in determining overall thruster efficiency. The ionization cost is the total energy required to form an ion, accounting for other simultaneous electron-neutral interactions. The ionization cost can exceed the threshold energy (12.6 eV for H_2O^+) for ionization to occur by several orders of magnitude. Note that in this treatment, we consider *only* loss mechanisms associated with electron-neutral interactions, not the cost of ions lost to the walls or in recombination reactions.

An expression for the ionization cost, E_c, of a noble gas is given below by Eq. (3.8), which depends on the reaction rate constants, κ, and energy losses, E_j, for ionization, electronic excitation, and elastic energy transfer between electrons and neutral atoms [121]. For a molecule, many more reactions, such as dissociation and excitation of vibrational and rotational modes must also be included.

$$\kappa_{ion} E_c = \kappa_{ion} E_{ion} + \kappa_{exc} E_{exc} + \langle \sigma_{elas} v \cdot 2 E_e \frac{m_e}{m_{H_2O}} \rangle \tag{3.8}$$

Note that the elastic scattering term in Eq. (3.8) is represented slightly differently than in the original source to emphasize that any energy term that is a function of E_e should be averaged with the interaction cross-section across the Maxwellian electron population. For energy losses that do not vary with electron energy, the threshold energy for the reaction is used.

The ionization cost is calculated for water vapor using the same framework as in Eq. (3.8), but adding in all dominant electron energy transfer mechanisms (elastic collisions, vibrational and rotational mode excitations, dissociative attachment, dissociation, ionization, and radiation), i.e. $\kappa_{ion} E_c = \sum_j \langle \sigma_j v E_j \rangle$. For completeness, the ionization cost was computed to take into account both the additional energy deposition into OH^+ creation and the additional ions formed as a result. Thus in the form of Eq. (3.8) for water, the left-hand side is modified such that: $\kappa_{ion} = \langle \sigma v_e \rangle_{H_2O^+} + \langle \sigma v_e \rangle_{OH^+}$. In this case, the ionization cost represents the cost to form $(1-\chi)\,H_2O^+$ and χH_2O^+ ions where $\chi = \langle \sigma v_e \rangle_{OH^+} / \left(\langle \sigma v_e \rangle_{H_2O^+} + \langle \sigma v_e \rangle_{OH^+} \right)$.

The cross-sections for the dominant reactions used in this analysis are shown in Fig. 3.4. Cross-section data was compiled from Itikawa [106], Thorn [122], and Khakoo [123]. The cross-sections for molecular energy dissipation mechanisms such as rotational and elastic scattering are orders of magnitude higher than the ionization cross-sections. However, it is important to note that the energy lost through these processes is also orders of magnitude lower than the ionization potential. The wide variations in cross-sections, energy losses, and effects of averaging over a Maxwellian population result in non-trivial contributions by each process to the overall energy balance, the results for which are shown in Fig. 3.5.

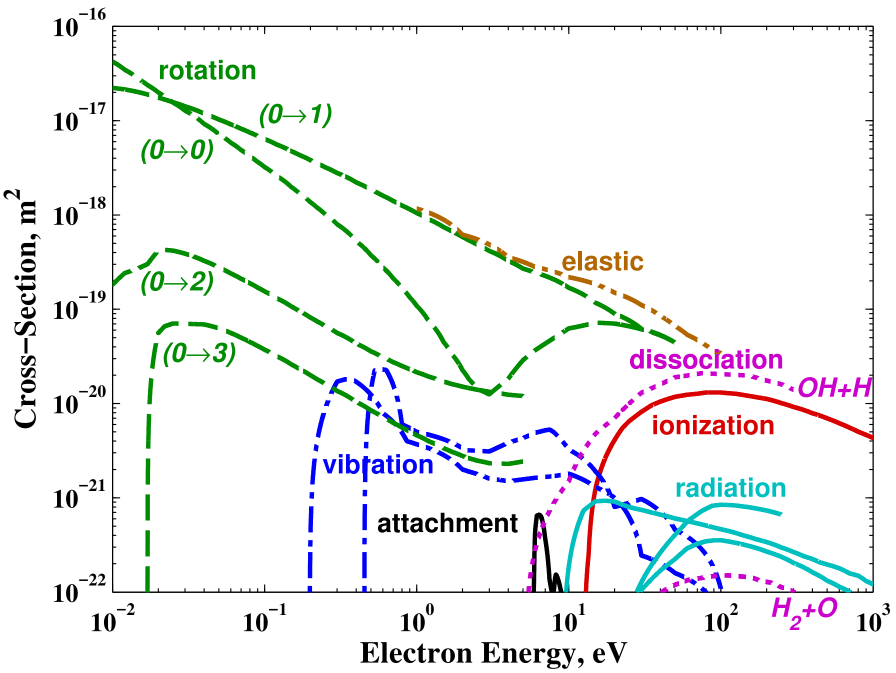

Figure 3.4: Cross-sections for dominant electron interactions with water vapor used in ionization cost calculations.

A comprehensive list of reactions considered, associated energy losses, and references are given in Table 3.1. For rotational transitions, the average value of each reported energy range is used to estimate ionization cost. Of the many possible electronically excited states of H_2O, the cross-sections for the a^3B1 and A^1B1 states were found to be dominant [122], and thus other states are neglected in comparison. Likewise, while all radiation cross-sections given by Itikawa [106] are included, the first three (*OH(A-X), H Lyman* α*, and H Balmer* α) dominate the electron energy lost to radiation. It is also assumed that the OH products resulting from these three radiation reactions, along with the *H Balmer* β reaction and a^3B1 and A^1B1 states of H_2O, are also captured in the *OH(X)* dissociation cross-section. Thus, to avoid double-counting the dissociation energy loss, 5.1 eV is subtracted from the energy transferred in each of the above mentioned reactions ($E_j = E_{threshold} - 5.1\ eV$), as they each ultimately dissociate via this pathway. Lastly, it is noted that the creation of other positive ions (e.g. H^+, etc) are neglected as they are expected to be far outnumbered by H_2O^+ ions.

The distribution of electron energy loss among different reactions with neutrals is shown in Fig. 3.5 as a function of Maxwellian temperature. The fractional distribution of energy loss by process is given by Eq. 3.9 as a function of Maxwellian electron temperature. In this case, *electronic excitation* includes radiating and non-radiating dissociation reactions.

$$\left(\chi_j = \frac{\langle \sigma v E_j \rangle}{\sum\limits_j \langle \sigma_j v E_j \rangle} \right) \tag{3.9}$$

It can be seen that at low temperatures, the majority of electron energy is lost via rotational and vibrational excitations. At higher temperatures, electron energy is split predominately between ionization and both radiating and non-radiating dissociation reactions. At 6.8 eV, electrons give up equal amounts of energy to excitation and ionization processes. Above this temperature, ionization becomes the leading energy transfer pathway. It should be noted that the present results, shown

Table 3.1: Electron-neutral interactions in water vapor

Collisional process		Energy loss	Ref.
Elastic scattering		$2E_e\frac{m_e}{m_{H_2O}}$	[106]
Rotational excitation	*0-0: Elastic*	$2E_e\frac{m_e}{m_{H_2O}}$	[106]
	0-1: Inelastic	4.6-5.2 meV	[106]
	0-2: Inelastic	8.7-16.9 meV	[106]
	0-3: Inelastic	17.6-35.4 meV	[106]
Vibrational excitation	*100+001: Inelastic*	0.45 eV	[106, 123]
	010: Inelastic	0.20 eV	[106, 123]
Dissociative attachment		E_e (electron captured)	[106]
Dissociation *(into non-radiating fragments)*	*OH(X)+H(n=1):*	5.1 eV	[106]
	$O(^3P) + H_2(X)$[1]	5.0 eV	[106]
	$O(^1D) + H_2(X)$[2]	7.0 eV	[106]
	$O(^1S) + H_2(X)$	9.2 eV	[106]
Electronic excitation	a^3B1	7.14 eV	[122]
	A^1B1	7.49 eV	[122]
Radiation *(from fragments)*	*OH(A-X) transition*	9.15 eV	[106]
	H Lyman α	15.3 eV	[106]
	H Balmer α	17.2 eV	[106]
	H Balmer β	18.6 eV	[106]
	O 844.7 nm	14.6 eV	[106]
	O 777.4 nm	15.7 eV	[106]
	O 130.4 nm	14.7 eV	[106]
Ionization	H_2O^+	12.6 eV	[106]
	OH^+	18.1 eV	[106]

in Fig. 3.5, differ from those given by Fridman and Kennedy in [113] for a water vapor plasma with a Maxwellian electron population. Particularly, the fraction of energy lost to dissociative attachment reactions is expected to be much lower than indicated in the referenced work.

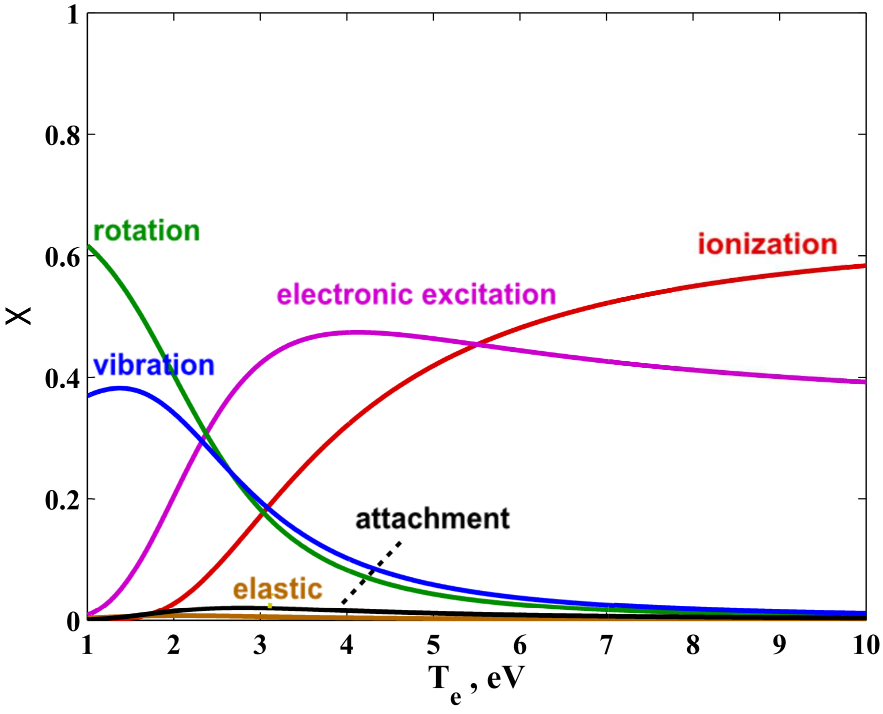

Figure 3.5: Fractional distribution of energy loss by process as a function of Maxwellian electron temperature.

Using the reactions given in Table 3.1 and the framework given by Eq. (3.8), the ionization cost is calculated for a range of Maxwellian electron temperatures. A brief review of the literature on helicon source electron energy distribution functions (EEDFs) revealed that electrons found in such systems are most likely Maxwellian distributed [108, 124, 125]. Cannat [109] showed that rate constants using measured ECR EEDFs closely matched those calculated with a Maxwellian assumption. For comparison with water, the ionization cost of argon with Maxwellian electrons is also calculated using the cross-sections employed in [126]. Argon is chosen because it has been the primary gas used in laboratory RF plasma experiments. The results are plotted in Fig. 3.6. Results will be compared with independent calculations for the ionization cost for water performed by Kovtun [127] with Maxwellian electrons at 3 eV and above.

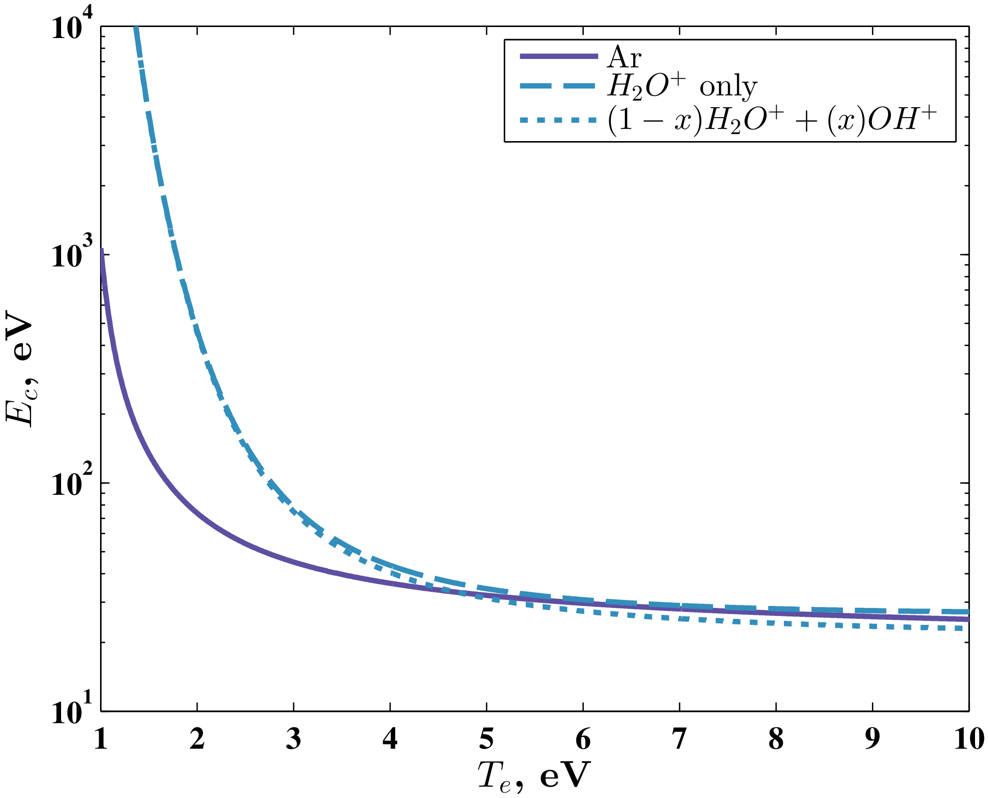

Figure 3.6: The ionization cost for H_2O compared with Ar for Maxwellian electrons between 1 and 10 eV.

This analysis indicates that while the ionization cost for water is substantially higher than that of argon at low temperatures, it becomes comparable at just a few eV. For example, at 3.2 eV, both the present model and the Kovtun model estimate an ionization cost of 65 eV for water while 43 eV is predicted for argon. Furthermore, the ionization cost for water predicted in this analysis becomes equal to that of argon at around 5 eV, and beyond this point, the ionization cost for water is predicted to be even lower than that of argon. At 10 eV, the production of a water ion is predicted to require 23 eV while an argon ion would require 25.2 eV. At high temperatures ($T_e = 100\ eV$), likely unreachable with a laboratory plasma, the ionization cost of a water molecule asymptotes to 20.8 eV in the present work, and 16.9 eV in the Kovtun model. It is believed that discrepancies between the present work and that of Kovtun are largely due to treatment of dissociation reactions, particularly the inclusion of the *OH(X)* generation cross-sections in this analysis. Note that this work also includes the energy cost for OH^+ ions but the difference between the ionization cost calculated in this formulation and considering H_2O^+ ion creation only is below 5 % for the electron temperature range considered. For example, at 10 eV, the ionization cost in this formulation is 23.0 eV whereas the result for H_2O^+ ions only would be 23.9 eV.

Curve fits of the ionization cost are provided for use in future analyses. Different fits are provided for the regions between 1-3 eV (Eq. 3.10) and from 3 eV to 100 eV (Eq. 3.11). For the latter region, a similar functional form as is presented for fits in [127] is also employed here. Curve fit constants for both water and argon are given in Tables 3.2 and 3.3.

$$E_{c,low}(T_e) = c_0 e^{c_1 T_e^{c_2}} + c_3 T_e^{c_4} + c_5 \tag{3.10}$$

Table 3.2: Curve fit parameters for ionization cost results: $1 \leq T_e \leq 3$ eV

Species	c_0	c_1	c_2	c_3	c_4	c_5
Water	0.4202	13.72	-0.9948	-9.343×10^{-3}	7.115	52.23
Argon	72.78	2.673	-3.195	-0.01939	5.606	-25.86

Table 3.3: Curve fit parameters for ionization cost results: $3 \leq T_e \leq 100$ eV

Species	k_0	k_1	k_2	k_3	k_4
Water	32.93	2.051	-13.20	2163	-6.925
Argon	-42.42	-0.935	60.58	579.3	-4.316

$$E_{c,high}(T_e) = \frac{k_0 T_e}{T_e - k_1} + \frac{k_2 T_e}{T_e + k_1} + \frac{T_3 - k_3}{(T_e - k_4)^2} \tag{3.11}$$

3.4 Efficiency of a water vapor plasma thruster

The conclusions drawn from the preceding section are used to develop a model for thrust efficiency as a function of electron temperature. The efficiency of an electrodeless thruster with ion acceleration in an expanding magnetic field is considered for both propellants. The thrust efficiency model is derived from existing frameworks [86, 99, 101]. Efficiency improvements enabled by the addition of an upstream magnetic mirror are also considered. The assumptions and pertinent equations are discussed below.

This model predicts efficiency by comparing the energy required to generate and accelerate the plasma to the thrust power contained in the exhaust beam. Ions are considered to be monoenergetic and electrons to be isotropically Maxwellian distributed. There are two primary sources of energy deposited into each electron-ion pair that leaves the plasma, (1) the energy required to create the ion, E_c and (2) the energy associated with particle acceleration across a wall-sheath or magnetic nozzle (assumed to be equivalent). Each is a function of the electron temperature. Additionally, each electron deposits $2T_e$ across the sheath.

Thus, the energy per particle comprising the exhaust beam is given as:

$$E_{beam} = e|\Delta\phi_{sh}(T_e)| \tag{3.12}$$

and the total energy for each ion-electron pair lost to the exhaust or to a wall is given by:

$$E_{total} = e\left[|\Delta\phi_{sh}(T_e)| + 2T_e + E_c(T_e)\right] \tag{3.13}$$

The thrust efficiency can be calculated by combining the energies above with the particle flow rates out of the exit and to the upstream wall. Whether particle loss to the radial walls represents a significant energy sink in these systems is still somewhat of an open question. Ahedo [101] showed that even for a very narrow (1 cm radius) source and a modest (200 Gauss) magnetic field, the particle density at the radial wall should be reduced by a factor of 10 to 100. For a 600 Gauss axial field in the same source, they justify neglecting lateral losses altogether. Similarly, Fructhman's cross-field diffusion model [128] predicts radial diffusion to be orders of magnitude lower than in the axial direction at typical operating conditions. LaFleur [86] cites empirical data which indicates that when the source radius is at least 5 times greater than the ion cyclotron radius, the plasma edge density will be 10% or less of that in the center. For weak magnetic fields or large length to radius ratios, radial fluxes can contribute non-negligible power losses, but for this model idealized radial confinement is assumed. As a result, the ion generation rate is assumed to be exactly equal to the sum of the (magnetic field dependent) upstream and downstream loss rates. Power losses associated with unimpeded charged particle transport upstream have been shown in previous models to significantly limit the thrust efficiency of electrodeless thrusters [99, 101]. An upstream magnetic mirror can be created, for example, by the addition of a permanent ring magnet at the front wall [100] to reduce losses. The reduction in electron transport is a function of the mirror ratio between the constant axial field in the bulk of the discharge and the high field region near the front wall. The upstream electron flux, Γ_{wall}, in a converging magnetic field can be found by taking the first moment of the Boltzmann distribution function projected along the axis of travel. According to the conservation of the magnetic moment and energy, only particle velocities within a loss cone of half-angle $\theta_{cr} = sin^{-1}\left(\sqrt{1/R_m}\right)$ are allowed, where R_m is the ratio of the upstream magnetic field at the wall, B_{max}, to the constant axial field, B_0.

$$\Gamma_{wall} = \int_0^{\theta_{cr}} d\theta \int_0^{2\pi} d\phi \int_0^{\infty} dv \left[n_0 \left(\frac{2\pi e T_e}{m_e} \right)^{\frac{3}{2}} e^{-\frac{\frac{1}{2}m_e v^2 + e\Delta\phi}{eT_e}} v^3 \sin\theta \cos\theta \right] = \frac{1}{R_m} \frac{n_0}{4} \bar{c}_e e^{\frac{\Delta\phi}{T_e}} \tag{3.14}$$

Thus the upstream electron flux is reduced from the typical 1D result by the factor of B_0/B_{max}. The ion flux in a converging magnetic field is treated differently due to their low collisionality. Martinez-Sanchez and Ahedo [129] showed that electrostatic potentials forming near the last closed magnetic field lines will focus ions into the cusp region of the converging field and will prevent them from impacting the wall elsewhere. The flux, however, even in the case of magnetized Maxwellian ions, is found to be approximately equal to that into a planar wall sheath ($\Gamma_i \approx 0.5 n_0 v_b$). Thus, though the flux of ions is not reduced, the potential structure acts to limit the wall area exposed to the flux. The exposed area, A_{wall} can be found from the magnetic field ratio ($A_{wall} = A_0/R_m$), where A_0 is the cross-sectional area of the cylindrical discharge chamber. This is also the area exposed to the reduced electron flux.

A sheath structure is still expected to form along the wall where electrons and ions impact to maintain zero net current in steady-state. The required potential can be found by equating the ion and electron currents at the wall. Because the exposed wall area is the same for electrons and ions, this is equivalent to equating the upstream fluxes described above. The sheath is treated as a discontinuous jump in potential such that the magnetic field at the pre-sheath sheath boundary is approximately equal to the field at the wall.

$$\Gamma_i = \Gamma_e \tag{3.15}$$

$$0.5 n_0 v_b = \frac{1}{R_m} \frac{n_0}{4} \bar{c}_e e^{\frac{\Delta\phi_{mirror}}{T_e}} \tag{3.16}$$

It can be shown that the magnitude of the required potential difference between the wall and plasma is thereby reduced in the presence of a magnetic mirror, as given by Eq. (3.17).

$$|\Delta\phi_{mirror}| = |\Delta\phi_{sh}| - T_e ln\left(R_m\right) \tag{3.17}$$

The above results can be combined into a zero-D thrust efficiency model to compare theoretical operation with water vapor to argon. The thrust efficiency, η_T, is defined as the ratio of the beam power to the power required to sustain and accelerate the plasma $\left(\eta_T = \frac{P_{beam}}{P_{in}}\right)$. A well-matched antenna can transfer RF power very efficiently ($\eta_{RF} \approx 0.9$ in [130]) and thus RF losses are neglected here. It is assumed that an antenna can couple to a water plasma as efficiently as argon, though this could be an interesting venue for future study. Losses associated with divergence in the exhaust plume are neglected, though a constant multiplicative factor ($\eta_D \approx 0.7 - 0.85$ [131]) could be added. Again, it is not expected that the divergence efficiency will differ substantially between argon and water vapor. Thus to account for RF and divergence losses, the idealized thrust efficiencies presented below could be simply scaled by a factor of $\eta_{RF}\eta_D$. It is assumed that the magnetic field can be generated with a combination of permanent and superconducting magnets at no power cost.

$$\eta_T = \frac{\Gamma_i e A_0 |\Delta\phi_{sh}|}{\Gamma_i e A_{wall}\left(2T_e + |\Delta\phi_{mirror}| + E_c\right) + \Gamma_i e A_0\left(2T_e + |\Delta\phi_{sh}| + E_c\right)} \tag{3.18}$$

Eq. (3.18) simplifies to:

$$\eta_T = \frac{|\Delta\phi_{sh}|}{\left(1 + \frac{1}{R_m}\right)\left[2T_e + |\Delta\phi_{sh}| + E_c\right] - \frac{T_e}{R_m} ln(R_m)} \tag{3.19}$$

The thrust efficiency from the above expression is plotted as a function of electron temperature for both water and argon, for several magnetic field ratios in

Fig. 3.7, and as a function of magnetic field ratio for several electron temperatures in Fig. 3.8, both for water vapor (dashed lines) and argon (solid lines). It is apparent that the efficiency of a water propelled thruster tracks quite closely with that of a traditional argon system for electron temperatures above 5 eV. For sufficiently high mirror ratios and electron temperatures, thrust efficiencies above 50% may be possible with strong radial and upstream confinement.

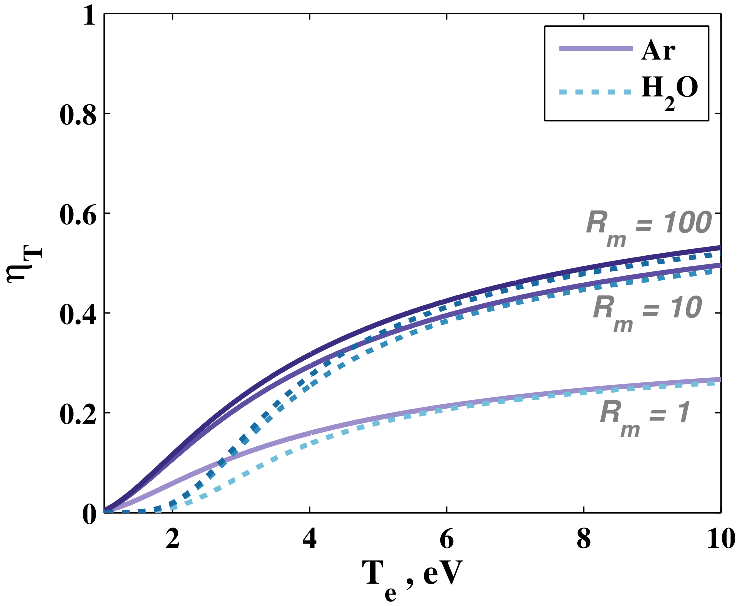

Figure 3.7: Thrust efficiency for an electrodeless thruster operating with water vapor versus electron temperature

The dependence on the mirror ratio shown in Fig. 3.8(b) indicates that negligible additional gains are achieved for mirror ratios greater than 20. For reference, the mirror ratio of the design proposed in [100] is on the order of 10. Much higher ratios may be hard to achieve experimentally while maintaining good radial confinement and reasonable magnet masses. Furthermore, for electron temperatures below 2 eV,

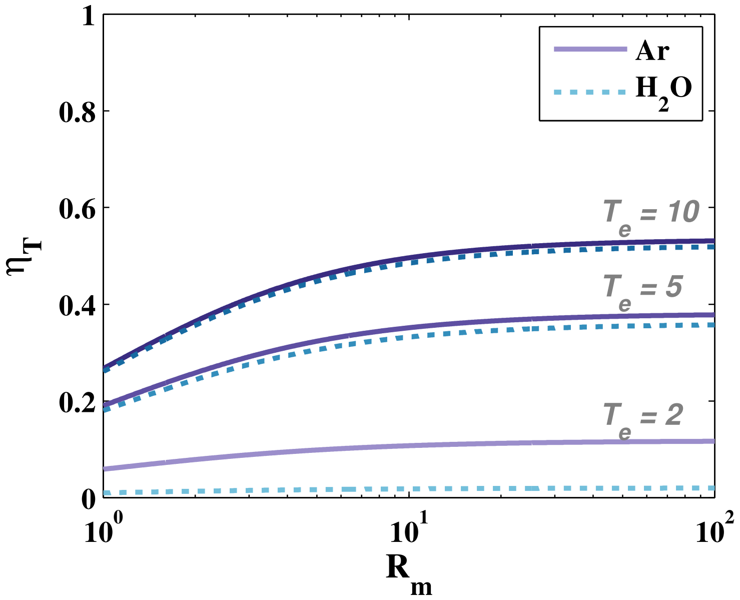

Figure 3.8: Thrust efficiency for an electrodeless thruster operating with water vapor versus upstream magnetic field ratio.

the thrust efficiency of the water vapor system is extremely poor, regardless of the upstream mirror effects. However for a 10 eV electron population, the addition of a sufficiently strong magnetic mirror could essentially double the thrust efficiency. The electron temperatures measured for RF water vapor plasmas in previous studies [102, 103] are between 1 and 9 eV. Thrust efficiencies demonstrated to date in helicon plasma thrusters have typically been less than 10%, as would be expected for a low temperature (1-3 eV) discharge without upstream mirror. Thus it will be necessary to verify experimentally whether good upstream confinement and high electron temperatures (above 5 eV) can be attained for argon and for water vapor. Additionally, this model neglects heavy particle collisions that could result in more complex plasma chemistry. One such reaction, $H_2O^+ + H_2O \longrightarrow H_3O^+ + OH$ could result in non-negligible hydronium ion, H_3O^+, populations depending on plasma densities and device length scales. Similar to OH^+, the H_3O^+ ion would behave in a manner dynamically similar to the H_2O^+ population. In Chapter 5, a more detailed plasma chemistry model is implemented to assess the impact of potential ion-ion and ion-neutral reactions on plasma composition and thrust efficiency.

3.4.1 Conclusions

The suitability of water vapor as a propellant in electrodeless RF thrusters has been investigated from an analytical perspective, with model assumptions constrained by relevant theoretical and experimental results. Major conclusions from the literature affecting the efficiency model include (1) the ability to neglect negative ions except as an ionization energy loss pathway, (2) the behavior of the discharge as electropositive, dominated by H_2O^+ ions, and (3) the approximation of wall sheaths and magnetic nozzle potentials as 1D single-species Debye sheaths. Ionization costs for Maxwellian electrons are calculated and compared to argon, with curve fits provided for follow-on analyses. Though the ionization cost for water far exceeds argon at low temperature, it becomes comparable around 5 eV. As a result, the efficiency of a water propelled electrodeless thruster also becomes comparable above 5 eV. Thrust efficiency increases with both electron temperature and upstream mirror ratio, with diminishing gains achieved above a factor of 20 for the latter. Thus, per a zero-D analysis, water vapor appears to be a suitable propellant if a Maxwellian electron temperature above 5 eV can be sustained. As the physics of the the RF wave propagation is omitted, these results are relevant to any electrodeless configuration with Maxwellian electrons provided that radial wall losses can be mitigated.

Chapter 4: Helicon Thruster Performance with Acceleration Stage

4.1 Overview

Sections 4.2 and 4.4 of this Chapter have been published in conference proceedings according to the following citations:

Petro, E. and Sedwick, R.,
Effects of Water Vapor Propellant on Helicon Thruster Performance,
52nd AIAA/SAE/ASEE Joint Propulsion Conference, 25-27 July, Salt Lake City, Utah, AIAA 2016-4735, published online 22 July 2016,
`https://doi.org/10.2514/6.2016-4735`

Petro, E. and Sedwick, R.,
Ion Cylotron Heating in an Eletrodeless Water Vapor Thruster,
35th International Eletric Propulsion Conference, 8-12 October, Atlanta, Georgia
IEPC-2017-468, published online 12 October 2017.

While the thrust efficiencies of the single-stage system are greatly improved by the addition of an upstream magnetic mirror, it was shown in the previous chapter that the above (idealized) results are still below many state-of-the-art Hall thrusters and ion engines [132]. Thus, the performance gains that can be realized through the addition of an acceleration stage are investigated. An electrodeless acceleration stage is preferred due to additional grid degradation that would be expected in a water plasma environment. The electrodeless acceleration stage investigated here is an ion cyclotron heating (ICH) stage. This concept has been demonstrated in the VASIMR system [133] to effectively increase the energy of the exhaust by resonantly heating the ions. The ions gain a large rotational energy which is converted to translational energy as the plasma expands through a diverging magnetic nozzle.

In this chapter, the principles and physics of ion cyclotron heating are introduced, along with a summary of previous studies on ion cyclotron heating in plasma thrusters. Then the thrust efficiency analysis that was developed in Chap. 3 is extended to capture the addition of an ion cyclotron heating acceleration stage in the context of a water plasma thruster. This model is used to evaluate the parameter space over which such a design modification would be desirable. Finally, a particle-based model is presented as a means of studying the detailed response of plume ions to ICH heating.

Nomenclature

B = magnetic field strength

d = distance between parallel plate electrodes

ϵ = dielectric constant

ε_{ICH} = ion cyclotron energy

E = electric field strength

I = current

I_{sp} = specific impulse

g = acceleration due to gravity

m = mass

μ_0 = permeability of free space

N = number of cyclotron oscillations

n_{turns} = numbers of turns of wire

n_e = electron density

ϕ_0 = electric field phase

q = plasma shielding parameter

r = radius

R_m = magnetic field (mirror) ratio

t = time

t_{wire} = thickness of wire

T_e = electron temperature

T_i = ion temperature

V_0 = potential difference

ω_{ce} = electron cyclotron frequency

ω_{ci} = ion cyclotron frequency

ω_{pe} = electron plasma frequency

4.1.1 Physics of Ion Cyclotron Heating

It is well known that a particle of charge, q, traveling perpendicular to a magnetic field with some velocity, $v_\perp$, will experience a centripetal acceleration due to the Lorentz force ($\vec{F} = q\vec{v} \times \vec{B}$) that causes it to gyrate about the magnetic field lines (Fig. 4.1).

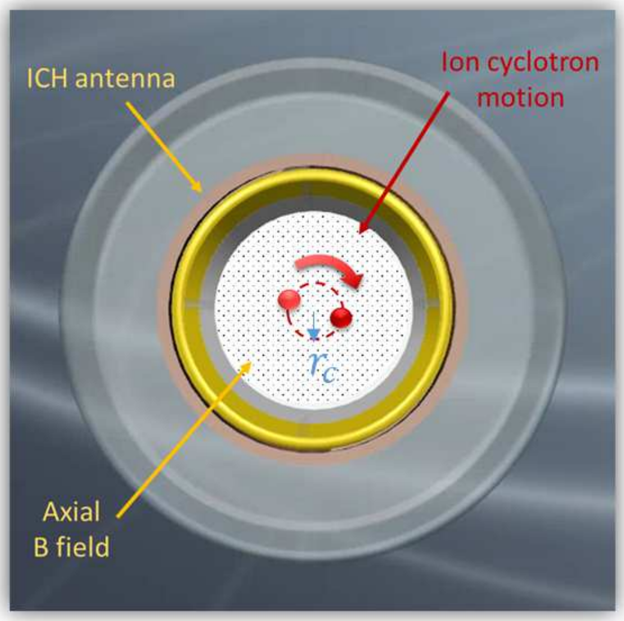

Figure 4.1: Diagram showing ion cyclotron motion for a charged particle.

The gyro orbit (Larmor) radius, r_L and cyclotron frequency, ω_c are determined by the particle's velocity perpendicular to the magnetic field, the magnetic field strength, B, and the particle mass, m.

$$r_L = \frac{qv_\perp}{mB} \tag{4.1}$$

$$\omega_c = \frac{qB}{m} \tag{4.2}$$

Ion cyclotron heating is the process by which an external electric field is applied to accelerate the particles in the direction perpendicular to the magnetic field. The accelerating field must oscillate at the same frequency as the particle orbits the magnetic field lines. Thus in practice, an RF antenna is tuned to the ion cyclotron frequency and used to resonantly increase the perpendicular kinetic energy of the charged particles.

Many different types of antennas have been employed to heat ions in this way. For example, Ilin et. al. [134] compared the heating efficiency of various antenna geometries and eventually settled on a 1/4-turn antenna that launches left-hand polarized waves at the ion cyclotron frequency. Other groups have studied the use of antennas as simple as parallel plates to create a perpendicular electric field oscillating at the ion cyclotron frequency [135].

Ion cyclotron heating has been employed for various applications including fusion experiments [136], mass spectrometry [137], and high specific impulse electric propulsion. When implemented in a plasma thruster, the ICH process is referred to as "single pass" where the ions will travel through the heating region only once. Other implementations may have plasma confined between magnetic mirrors where ions oscillate axially and pass through the heating regions many times. In either case, it is desirable to have the ion experience several gyro-orbits while in the heating region. This requirement impacts the design of the antenna and is addressed in

Section 4.4 of this Chapter.

4.1.2 Ion Cyclotron Heating in Plasma Thrusters

In a plasma thruster, the plasma is generated upstream then diffuses into a second stage where ions are heated resonantly via an external antenna tuned to the ion cyclotron frequency. In this region, the plasma may remain quasi-neutral but the ions are heated such that $T_i >> T_e$ and heating frequencies are magnetic field dependent, but typically in the MHz range.

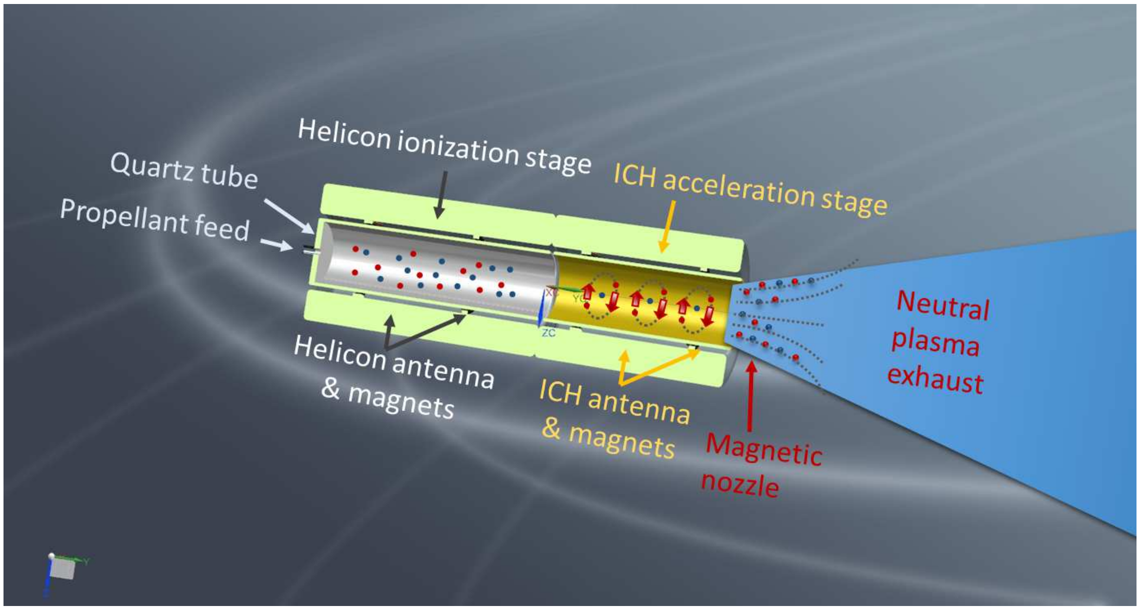

Figure 4.2: Diagram of plasma thruster with an ion cyclotron heating stage.

The high rotational energy gained in the ICH process must be converted into directed kinetic energy to produce useful thrust. This conversion occurs as the plasma exits along a diverging magnetic field beyond the ICH region. The diverging magnetic field forms a magnetic nozzle that guides the expansion of the plasma and the energy conversion. The principle behind energy conversion in a magnetic nozzle is the conservation of the magnetic moment, μ, (Eq. 4.3), and conservation of energy (Eq. 4.4).

$$\mu = \frac{mv_\perp^2}{2B} \tag{4.3}$$

$$v_0^2 = v_\perp^2 + v_\parallel^2 = const \tag{4.4}$$

As the axial magnetic field strength drops across the magnetic nozzle, the perpendicular velocity drops proportionally and the parallel (directed) kinetic energy increases. The VASIMR group [138] has demonstrated ICH energy conversion efficiencies $> 90\%$ in their design. They have also demonstrated the efficacy of ion cyclotron heating for a range of propellants (H_2, D_2, Ar) and have demonstrated overall thrust efficiency in excess of 70% at high power levels (200 kW) [90]. The goal of the present analysis is to assess the scalability of this process for a small scale, moderate power water-propelled thruster.

4.2 Quasi-1D Efficiency Analysis

In the second stage, the cold ion approximation no longer applies, though the ions are still assumed to be monoenergetic in the idealized case. The magnetic field in the ICH region must be large enough that it keeps ions sufficiently magnetized so that they are not lost to the walls as their rotational energy increases. However, it must also be lower than the mirror field at the upstream wall.

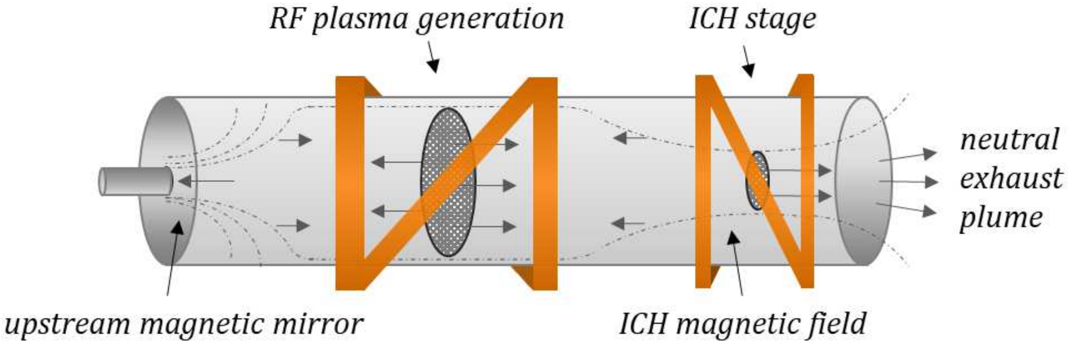

Figure 4.3: Diagram of charged particle fluxes in a two-stage electrodeless plasma thruster employed in a thrust efficiency analysis [1].

4.2.1 Efficiency without Wall Losses

First, the thrust efficiency is evaluated naively assuming that the downstream magnetic field is strong enough to confine the ions such that they are not lost to the walls at high rotational energies. This could potentially be accomplished with a diverging chamber geometry (though the magnetic field strength is usually inversely proportional to the magnet radius). If 100% RF power coupling into the plasma is assumed, then the thrust efficiency can be determined from the upstream and downstream particle flow rates and energies. Per the same conclusions drawn above for the upstream field, ion flux is assumed to be independent of magnetic field strength, but the effective area will decrease by the inverse of the mirror ratio. Thus, an expression for the thrust efficiency with the addition of ion cyclotron heating is given in Eqn. 4.5 where $R_{m,1}$ and $R_{m,2}$ are now the respective upstream and downstream magnetic mirror ratios, and $|\Delta\phi_{1,2}|$ are the respective upstream and downstream potential differences required for equal ion and electron currents in steady-state. E_{ICH} is the additional (initially rotational) energy (in eV) deposited per particle by the ICH antenna.

$$\eta_T = \frac{\Gamma_i e \frac{A_0}{R_{m,2}} \left(E_{ICH} + |\Delta\phi_2| + \frac{1}{2}T_e \right)}{\Gamma_i e \frac{A_0}{R_{m,1}} \left(\frac{1}{2}T_e + 2T_e + |\Delta\phi_1| - T_e ln(R_{m,1}) + E_c \right) + \Gamma_i e \frac{A_0}{R_{m,2}} \left(\frac{1}{2}T_e + 2T_e + |\Delta\phi_2| + E_c + E_{ICH} \right)} \tag{4.5}$$

Eqn. 4.5 can be simplified to:

$$\eta_T = \frac{\left(E_{ICH} + |\Delta\phi_{sh}| - T_e ln(R_{m,2}) + \frac{1}{2}T_e \right)}{\frac{R_{m,2}}{R_{m,1}} \left(\frac{1}{2}T_e + 2T_e + |\Delta\phi_{sh}| - T_e ln(R_{m,1}) + E_c \right) + \left(\frac{1}{2}T_e + 2T_e + +|\Delta\phi_{sh}| - T_e ln(R_{m,2}) + E_c + E_{ICH} \right)} \tag{4.6}$$

In the limit that the upstream magnetic mirror is much larger than the downstream mirror ($R_{m,2}/R_{m,1} \ll 1$), the thrust efficiency further simplifies to:

$$\eta_T = \frac{\left(E_{ICH} + |\Delta\phi_{sh}| - T_e ln(R_{m,2}) + \frac{1}{2}T_e \right)}{\left(\frac{1}{2}T_e + 2T_e + |\Delta\phi_{sh}| - T_e ln(R_{m,2}) + E_c + E_{ICH} \right)} \tag{4.7}$$

Eq. (4.7) is evaluated for 3 downstream magnetic field ratios ($R_{m,2}$ = 1,5,10) for varying amounts of ICH energy deposited. In this simplified case, the only effect of the downstream magnetic mirror is to decrease the accelerating electrostatic potential. The results, shown in Fig. 4.4, indicate that thrust efficiency could potentially be improved to values competitive with state-of-the-art systems in a two-stage configuration.

Argon results are shown in Fig. 4.4(a)-(c) and water vapor in Fig. 4.4(d)-(f). Lines represent constant ICH energy addition from $E_{ICH} = 0$ up to $E_{ICH} \approx 50$ eV/amu. Thus the lowest efficiency curve in each case represents perfect reflection upstream with no ICH energy deposition. For both argon and water vapor, minimal improvements in efficiency are gained beyond the addition of 12.5 eV/amu, corresponding to the 6^{th} line on each plot and an Isp of approximately 5000 seconds.

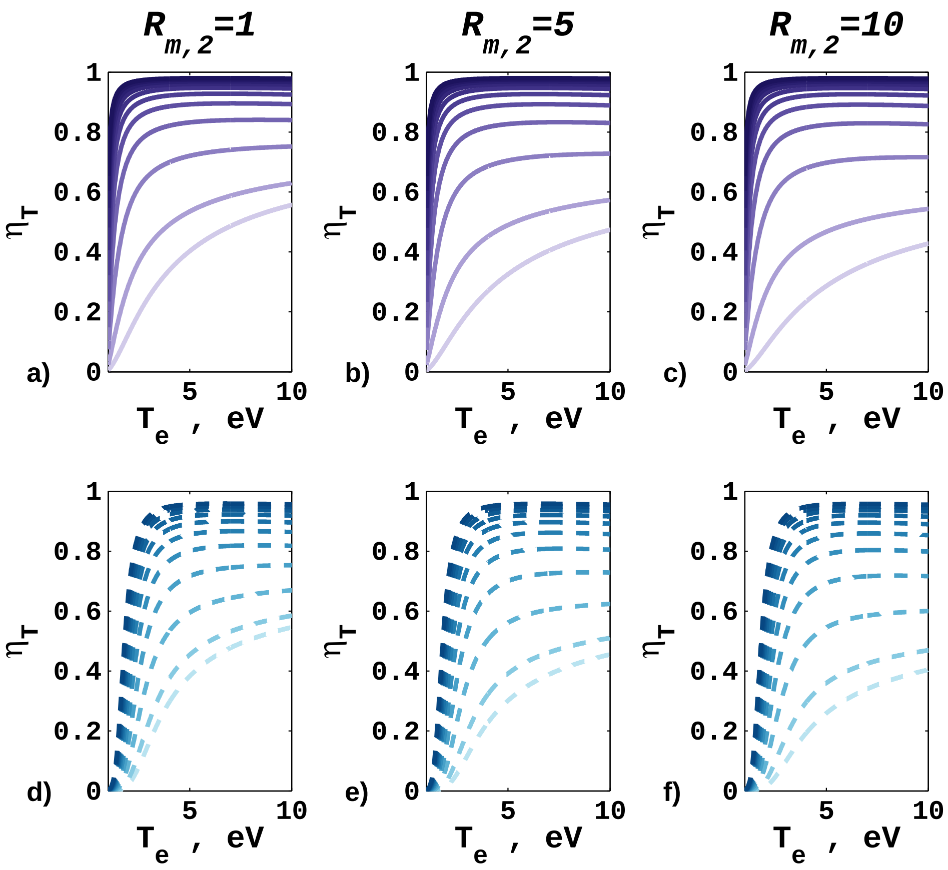

Figure 4.4: Thrust efficiency of a two-stage helicon thruster for varying downstream magnetic mirror ratios.

While these results seem to indicate that higher efficiencies can be achieved given the same ICH power for lower downstream magnetic fields, higher fields will be desirable to actually confine the particles when more realistic geometry and achievable field strengths are taken into account.

4.2.2 Efficiency with Wall Losses

The results given in Fig. 4.4 are optimistic as they do not couple the downstream magnetic field strength to the ion gyro radius. Anticipating that relatively strong fields will be required for confinement, we return to Eq. (4.6) and relax the assumption that ($R_{m,2}/R_{m,1} \ll 1$). Instead, based on the results of Chapter 3.4, $R_{m,1}$ is set to 20, above which diminishing improvements in efficiency are seen. The downstream mirror ratio must be sufficiently smaller than $R_{m,1}$ so that ions will preferentially travel downstream. As before, values of $R_{m,2} = 1,\ 5$, and 10 are evaluated. Now, the ion Larmor radius in the ICH stage, $r_{L,2}$, is allowed to vary with E_{ICH} and B_2:

$$r_{L,2} = \frac{m_i v_{i,\perp}(E_{ICH})}{eB_2} \tag{4.8}$$

For this analysis, a more realistic assumption of a constant wall cross-section is assumed (especially in light of the need for higher magnetic fields). To more accurately model efficiency, particles with Larmor radii that would impact the original chamber wall at radius a_0 are considered lost from the exhaust beam (see Fig. 4.5). The maximum transmission radius, r_t, is the plasma radius in the ICH stage, a_2.

The loss of particles in the ICH stage can be captured by defining a transmission area, A_t, such that:

$$A_t = \pi r_t^2 \tag{4.9}$$

with $r_t = a_2 = a_0/\sqrt{R_{m,2}}$ if no particles are lost, i.e. $r_{L,2} < (a_0 - a_2)$, and $r_t = a_0 - r_{L,2}$ otherwise (until $r_t = 0$ for $r_{L,2} > a_0$). In this analysis, the flux of the particles is assumed to be uniform across the transmission cross-section.

The efficiency of the two-stage system is then given by:

$$\eta_T = \frac{\Gamma_i e A_t \left(E_{ICH} + |\Delta\phi_2| + \frac{1}{2}T_e\right)}{\Gamma_i e \frac{A_0}{R_{m,1}} \left(\frac{1}{2}T_e + 2T_e + |\Delta\phi_1| - T_e ln(R_{m,1}) + E_c\right) + \Gamma_i e \frac{A_0}{R_{m,2}} \left(\frac{1}{2}T_e + 2T_e + |\Delta\phi_2| + E_c + E_{ICH}\right)} \tag{4.10}$$

To evaluate Eq. (4.10) according to the constraints on A_t, an initial magnetic

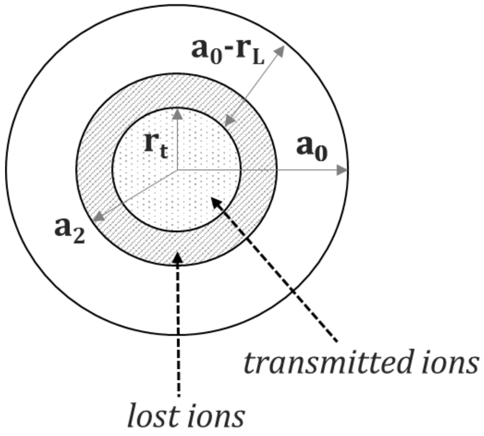

Figure 4.5: Diagram of particle transmission area and loss area based on ion Larmor radius.

field, B_0 and discharge chamber radius, a_0 must be specified. Results are generated and presented in Fig. 4.6 for $B_0 = 200\ G$ and $a_0 = 10\ cm$. The results are given for downstream mirror ratios of $R_{m,2} = 1,\ 5,$ and 10. Argon results are shown in Fig. 4.6(a)-(c) and water vapor in Fig. 4.6(d)-(f). Lines represent increasing amounts of ICH energy deposition to achieve $v_{ICH} = 0$ up to $v_{ICH} =$ 10,000 m/s. The faintest efficiency curve in each case represents the case of no ICH energy deposition, and in (a) and (d) this curve represents a single-stage helicon thruster with a strong upstream magnetic mirror.

The results shown in Fig. 4.6 demonstrate the importance of considering radial particle loss in the ICH efficiency analysis. Fig. 4.6(a) indicates that any resonantly heated ions would be lost to the walls without a stronger downstream confining field. In this case, the single-stage thruster outperforms a two-stage system because the energy is stored only in the axial direction. Figs. 4.6(b) and (c) show the improvements in efficiency possible for increasing magnetic field strengths in the

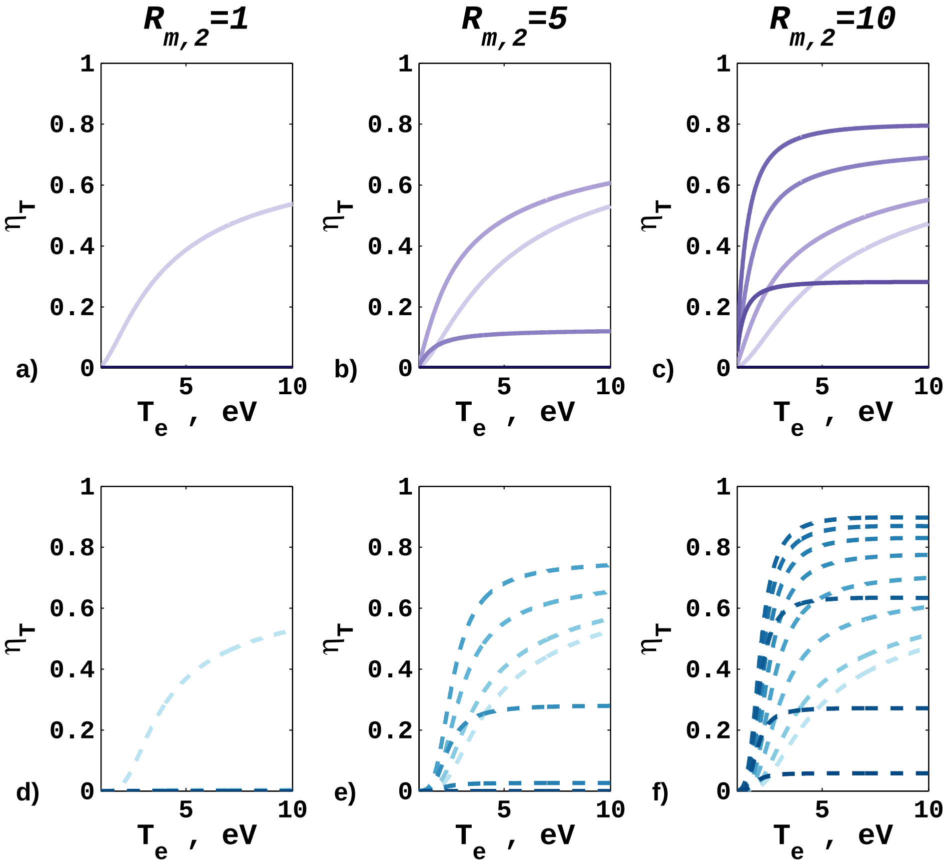

Figure 4.6: Thrust efficiency of a two-stage helicon thruster for varying downstream magnetic mirror ratios accounting for ion loss to the radial walls when $r_{L,2} > a_0$ when $B_0 = 200\ G$.

ICH region. In comparison, for the same discharge geometry and mirror ratios, Fig. 4.6(d)-(f) indicate that water vapor can achieve comparable efficiencies for a lower downstream mirror ratio due to the lower mass of the water ion.

For sufficiently strong downstream mirror ratios, it is found that there is an optimal Isp (e.g. amount of ICH energy deposited) that maximizes thrust efficiency. For the results shown in Fig. 4.6 the values of Isp that maximize thrust efficiency are as follows: (b) 1,000 s (c) 3,000 s (e) 3,000 s (f) 7,000 s.

For both propellants, once a sufficient population of the ions is confined, a higher downstream mirror ratio results in a lower thrust efficiency for a given amount of energy deposited per particle. This is due to the effect of the mirror ratio decreasing the maximum possible transmission area. This result is important with regard to the ability of the ICH stage to control specific impulse. If the downstream magnetic field strength cannot be changed, efficiency will suffer when operating off design conditions. There should exist an optimum downstream mirror ratio for a given upstream mirror ratio, specific impulse, and electron temperature that maximizes efficiency. If the mirror ratios are fixed (e.g. $R_{m,1} = \alpha R_{m,2}$), there should exist a specific impulse that maximizes efficiency for each electron temperature.

Fig. 4.6(a) and (d) conveniently indicate the performance of a single-stage helicon thruster. In comparison, the ICH-enhanced thruster curves only offer marked improvement for strong downstream magnetic fields. For both argon and water, thrust efficiencies near 80% are predicted, but only for a narrow band of ICH energies. The benefits of the ICH stage are more pronounced for low electron temperatures.

With the assumed discharge parameters, $R_{m,2}$=10 for water vapor allows for two-stage efficiencies between 60 and 90%. The required power, P_{in}, for such a system is estimated using the assumed 10 cm discharge radius and the energy sink terms in the denominator of Eq. (4.10). The total reduced input power, $\bar{P}_{in} = P_{in}/n_{0,19}$ as a function of electron temperature corresponding to the efficiency results in Fig. 4.6(e), are given in Fig. 4.7 ($n_{0,19}$ is the plasma density normalized by $10^{19}\ m^{-3}$). Lines represent constant ICH energy addition from $E_{ICH} = 0$ (bottom curve) up to

$E_{ICH} \approx 50$ eV/amu (top curve). It is worth noting that the curves corresponding to efficiencies above 60% also correspond to input powers above approximately 10 kW. These results also demonstrate the concept that for a given mirror ratio, there is an electron temperature that minimizes the input power required to obtain a particular specific impulse. For a given $R_{m,2}$, each line of constant E_{ICH} corresponds to a particular specific impulse.

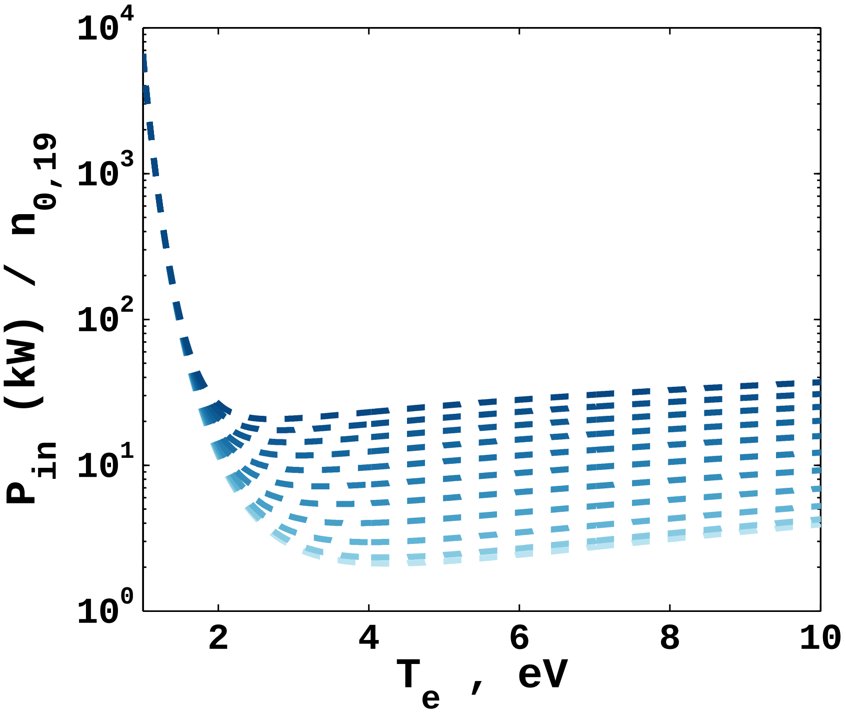

Figure 4.7: Reduced input power for a water propelled two-stage helicon thruster with $R_{m,1} = 20$, $R_{m,2} = 10$, $B_0 = 200\ G$ and $a_0 = 10\ cm$.

4.2.3 Quasi-1D Analysis Summmary

A two-stage thruster with an ICH heating stage is evaluated as a means of increasing the thrust efficiency to levels comparable with state-of-the-art electric propulsion systems. While a first-cut analysis neglecting particle losses in the acceleration stage indicated performance improvements for all ICH powers, a more careful analysis was required to impose physical limits on ion trajectories. The results of the latter analysis indicate that an optimum downstream magnetic field ratio exists. Below this ratio, too many particles are lost to the walls and the ICH system decreases efficiency when compared with single-stage operation. Above the optimum mirror ratio, the beam current is reduced due to the effective area reduction. All discharge parameters being equal, the optimum mirror ratio occurs earlier for water vapor due to its lower molecular weight. For a plasma density on the order of 10^{19} m^{-3}, the total power required to achieve thrust efficiencies above 60% is tens of kW. Thus, with the quasi-1D models developed, water vapor appears to be a suitable propellant in both single-stage and two-stage systems if a Maxwellian electron temperature above 5 eV can be sustained. As the physics of the helicon wave propagation has been omitted, these results are relevant to any similar electrodeless configuration with Maxwellian electron temperatures.

For the ICH stage, a more in-depth analysis may reveal additional loss mechanisms not accounted for here, such as those due to inter-particle collisions and thermalization effects.

4.3 Parameter Space Analysis

In this section, the model developed in the previous section is evaluated over a wide parameter space in order to identify favorable design points. The results presented in the previous section illustrated the benefits of ion cyclotron heating at various power levels for a particular design point (fixed heating stage radius, fixed magnetic field strength). Results presented in this section indicate maximal efficiencies for a range of device radii and magnetic field strengths assuming uniform heating and full RF field penetration into the plasma. This analysis will inform the design landscape over which ion cyclotron heating could be implemented to improve efficiency in an electrodeless water-propelled thruster. Then, particle-based analyses will be used to further explore particular design points.

4.3.1 Design Variables

The thrust efficiency model for a two-stage system developed in the previous section (Eqn. 4.10) is included again here for reference.

$$\eta_T = \frac{\Gamma_i e A_t \left(E_{ICH} + |\Delta\phi_2| + \frac{1}{2}T_e \right)}{\Gamma_i e \frac{A_0}{R_{m,1}} \left(\frac{1}{2}T_e + 2T_e + |\Delta\phi_1| - T_e ln(R_{m,1}) + E_c \right) + \Gamma_i e \frac{A_0}{R_{m,2}} \left(\frac{1}{2}T_e + 2T_e + |\Delta\phi_2| + E_c + E_{ICH} \right)} \tag{4.11}$$

There are a total of 6 design variables that affect the thrust efficiency in this model:

- The cross-section of the first stage section, A_0
- The magnetic field in the first stage section, B_0
- The ratio between the magnetic field in the first stage section and the maximum field at the upstream wall, $R_{m,1}$
- The ratio between the magnetic field in the second stage section and the maximum field at the upstream wall, $R_{m,2}$

- The energy deposited per particle via ion cyclotron heating (which ultimately determines the Isp), E_{ICH}
- The electron temperature, T_e

A few constraints on the above variables are applied to appropriately refine the parameter space. First, in the analysis performed in Chap. 3, it was shown that additional efficiency gains from the magnetic mirror at the upstream wall are negligible beyond $R_{m,1} = 20$, so the upstream mirror ratio is fixed at this value. At this value, 95% of the plasma flow to the upstream wall is reflected and the potential difference is reduced by a factor of $1 - \frac{ln(20)}{\Delta\phi_{sh}}$ or to 40% of its full value (see Section 3.4). Based on the analysis performed in Section 4.2.2, the ICH magnetic field strength is constrained to be 1/2 of the maximum field strength in the system (found at the upstream wall). This places the second constraint: $R_{m,2} = 10$.

These constraints leave us with 4 design variables to explore: [A_0, $R_{m,2}$, E_{ICH}, T_e].

4.3.2 Optimal Efficiency

As was observed in the previous section, the trade between improvements in specific impulse and losses due plasma expansion into the thruster walls results in a particular operating point that optimizes efficiency in a two-stage configuration. As the amount of energy deposited per particle via ion cyclotron heating is increased, the thrust efficiency curve over electron temperature will rise, until the energy is increased up to the point that a substantial fraction of the particles are lost to collisions with the wall. For each ICH energy-dependent η *vs.* T_e curve, there is a particular value of electron temperature that maximizes the thrust efficiency. This represents a balance between the decreases in ionization cost and the increases in energy transport to the walls with T_e. For a given magnetic field profile and thruster radius, the efficiency is found for a range of ICH energies for an electron temperature range between 1 and 10 eV. Across this 3D parameter space, the optimal efficiency and the associated ICH energy (presented in terms of Isp) are selected. Example results are shown in Fig. 4.8 for $B_0 = \textit{200 Gauss}$, $B_1 = \textit{4000 Gauss}$, and $B_2 = \textit{4000 Gauss}$. Note that, in this example, the magnetic field strength at the upstream wall is below the maximum allowable value as discussed in the previous section.

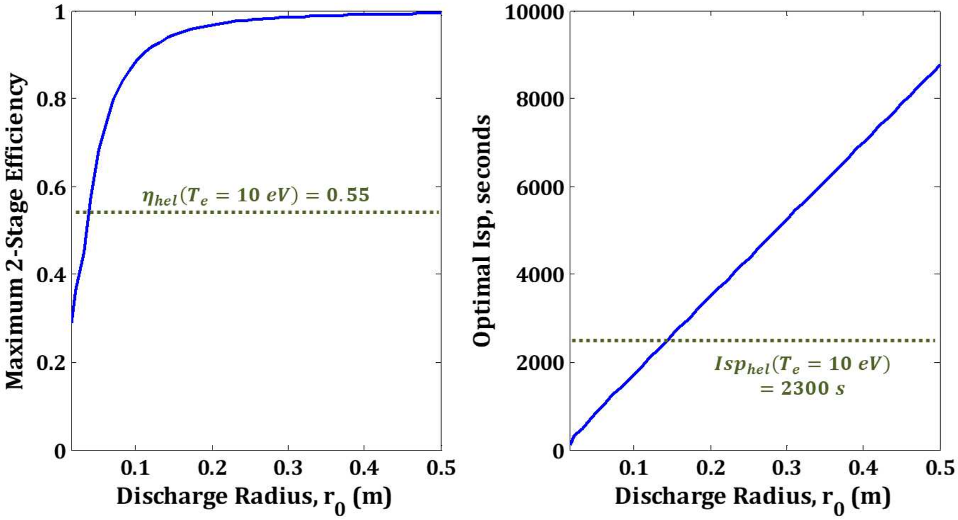

Figure 4.8: Optimal thrust efficiency (left) and associated specific impulse (right) as a function of thruster radius.

In general, the two-stage system would be worth implementing in the design space where the optimal efficiency exceeds the maximum efficiency possible with a single-stage thruster. In the single-stage model, the thrust efficiency increases monotonically with electron temperature but asymptotes to approximately 55% beyond T_e=10 eV. Thus any two-stage solutions allowing for $\eta > 0.55$ will be considered viable design points.

Additionally, it is interesting to note the specific impulse (and thus ICH energy) that maximizes the efficiency for each thruster radius. As shown in Fig. 4.8 the optimal Isp in the two-stage system is found to increase scale linearly with the radius. In some cases, the two-stage system is able to achieve a higher efficiency than the single stage thruster with a lower specific impulse. This is possible as the Isp in the single-stage system is determined by the electron temperature and higher electron temperatures result in higher power fluxes to the walls. In a two-stage system, the ions are heated directly instead of accelerated by ambipolar fields and thus the gains in efficiency with Isp are not offset by coupled electron losses. This allows for operation at lower electron temperatures and high efficiency at lower Isp values.

4.3.3 Parameter Space Results

The optimal efficiency of the two-stage system is found over a range of thruster radii and ICH magnetic field strengths. The constraints discussed in Section 4.3.1 are applied. The results are shown in Fig. 4.9.

A dashed line shows the 55% efficiency operating point of a single-stage system. Thus, only designs to the right of this line are considered desirable. This analysis

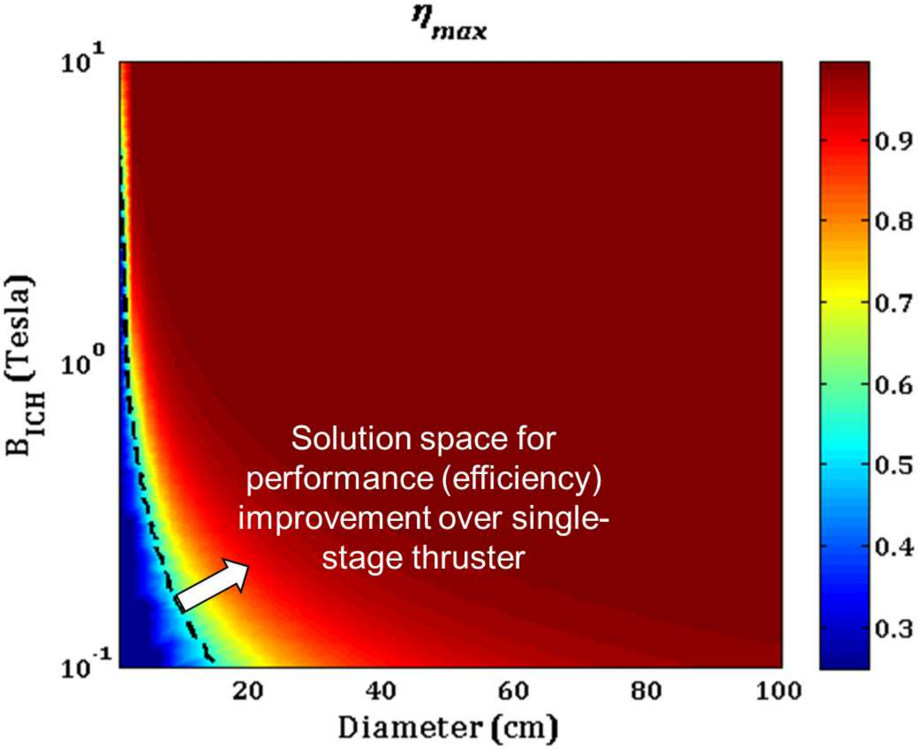

Figure 4.9: Contour plot of two-stage efficiency as a function of ICH field strength and thruster radius.

emphasizes the difficulty of implementation for small scale devices (D < 10 cm). For example, a thruster with a 10 cm diameter requires a magnetic field greater than 1500 Gauss in the ICH region and a maximum magnetic field strength beyond 3000 Gauss at the upstream wall. With traditional electromagnets, it is difficult to create uniform magnetic fields beyond 1000 Gauss. The possibility of creating these fields with small-form factor superconducting tape is discussed in the next section.

4.4 Ion Cyclotron Heating Particle Analyses

4.4.1 Goal of Particle Studies

The present analysis seeks to better capture the physics of the second stage heating and acceleration through 3D particle trajectory modeling. The system parameters (magnetic mirror ratios, ICH energy) from the quasi-1D model are used as inputs in the present analysis and implications for heating efficiency are predicted. In future work, the particle trajectory model presented here will be used to narrow down the design space for efficient implementation of ion cyclotron heating at a small scale. Once a design point has been selected, the system will be modeled using particle-in-cell methods to capture interactions between plasma particles and external electric and magnetic fields.

4.4.2 Magnetic Field Model

A strong axial magnetic field is required for ion heating and confinement. The 3D components of the magnetic field are calculated in the simulation domain using a Biot-Savart solver implemented in MATLAB. Azimuthal current densities and wire dimensions are specified and the Biot-Savart law is numerically integrated over discretized current segments to calculate $\vec{B}(\vec{x})$.

The centerline axial magnetic field strength in the heating region is constrained by:

1. Specified strength ratios between the ICH field and the upstream mirror field

identified in the quasi-1D analysis

2. Properties of state-of-the-art high temperature superconducting (HTS) tape

It is important that the magnetic field at the upstream wall be higher than the magnetic field in the ICH system so that the plasma preferentially flows downstream toward the exit. In the previous analysis, several magnetic field strength ratios were evaluated. Each ratio is defined with respect to the magnetic field in the plasma generation region, as defined in Fig. 4.10. For the 10 cm radius case previously considered, thrust efficiency over 80% was predicted with the magnetic field ratios $R_{m,1} = 20$ and $R_{m,2} = 10$. Thus these ratios are chosen to constrain the ICH stage magnetic field strength for the present analysis.

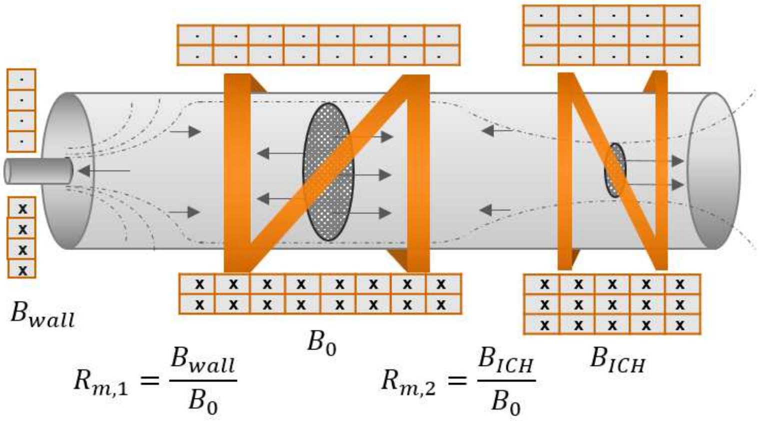

Figure 4.10: This diagram shows the three distinct magnetic field regions and defines the mirror ratios, $R_{m,1}$ and $R_{m,2}$.

The magnetic field, B_{wall}, that creates the upstream magnetic mirror is chosen to be the maximum field that can be created using currently available HTS tape [139]. It is assumed that the magnetic field is generated using a multi-turn current loop with the inner radius set equal to the minimum bend radius of the wire ($r_{min} = 5$ mm), carrying the maximum superconducting current at 77 K ($I = 300A$). This wire can be made in lengths up to 500 m [140], thus the number of turns in the current loop is calculated under this constraint. The thickness, t_{wire}, of the wire is 0.1 mm.

The magnetic field on-axis at the center of the current loop can be approximated using Eq. (4.12).

$$B_{center} \approx \frac{\mu_0 I}{2\bar{r}} \tag{4.12}$$

with $\bar{r} = (r_{min} + n_{turns}\frac{t}{2})$.

The maximum magnetic field upstream is thus estimated to be **3.5 T**. Note that the actual field could be reduced from this value due to (1) the need to operate below the critical current to remain superconducting and (2) the effects of magnetic fields at the wire location on the critical current value [141].

Using the mirror ratios defined above, we thus require a centerline magnetic field strength of approximately **1.75 T** in the ICH section. The ICH magnetic field should be constant under the antenna to maintain resonance at the ion cyclotron frequency. Thus the field should be generated with an HTS solenoid or Helmholtz coils (the latter only if the device radius and antenna length are of comparable dimensions). The relationship between the ICH field strength and antenna sizing will be discussed in Section 4.4.5.

Examples of both a solenoid and Helmholtz coil field for a 5 cm radius ICH chamber are shown in Fig. 4.11 and Fig. 4.12. It is suggested for future analysis to compare the efficiency of both heating and magnetic nozzle expansion in these two magnetic field configurations.

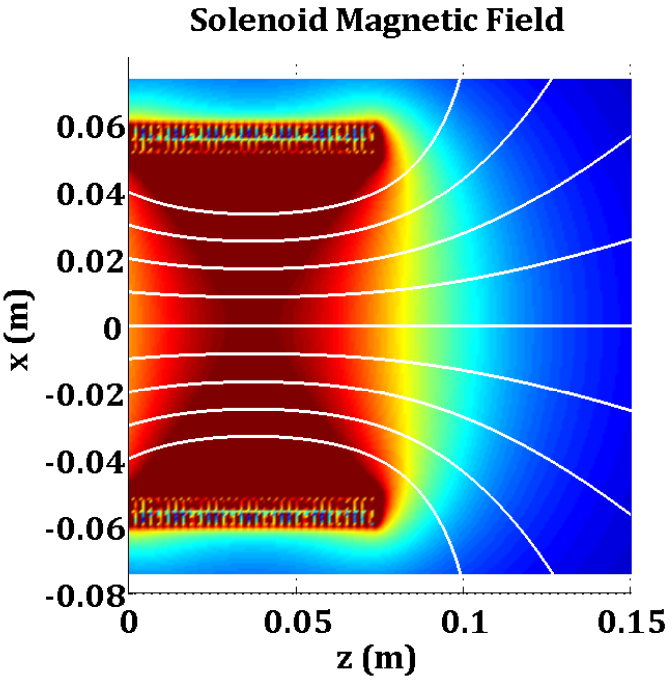

Figure 4.11: Magnetic field generated by solenoid of 5 cm inner radius, 7.5 cm length, and 55 layers of wire carrying 300 A.

4.4.3 Electric Field Model

Despite the depiction of the ICH antenna in Figs. 4.3 and 4.10 as helical, the electric field implemented for these calculations is actually more simplified. A uniform, linearly polarized electric field is implemented for this analysis. The accelerating electric field is modeled as the 1D electric field between two parallel plates separated by a distance, $d \approx 2r$, with a potential difference, V_0, oscillating at the ion

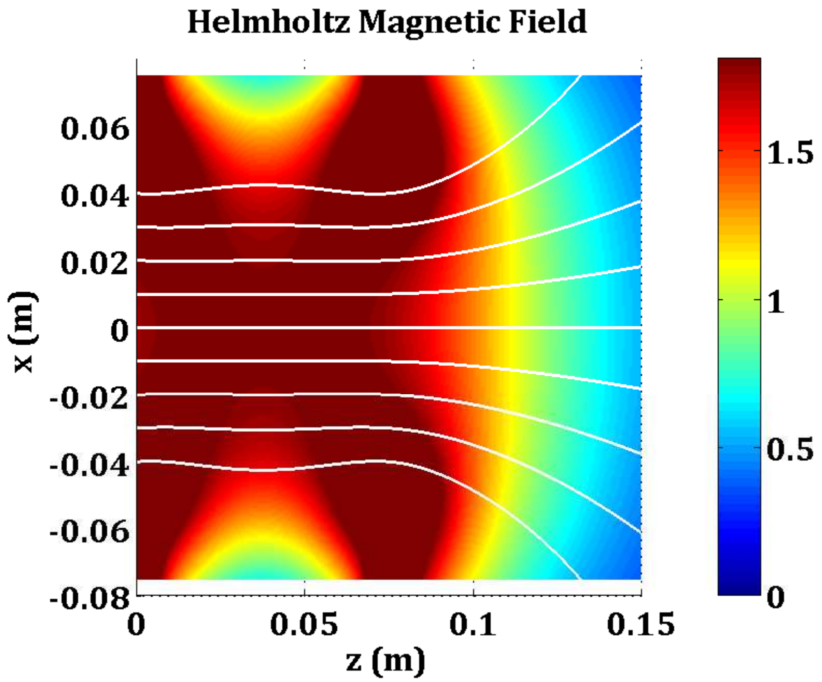

Figure 4.12: Magnetic field generated by Helmholtz coils of 5 cm inner radius with 500 layers of wire carrying 300 A, located 7.5 cm apart.

cyclotron frequency. For the selected magnetic field strength, the vacuum electromagnetic wavelength ($\frac{2\pi c}{\omega_{ci}}$) is 33 meters and thus much larger than the device radius. Additionally, assuming the strong magnetic field increases the skin depth beyond the size of the radius, a 1D, electrostatic approximation may be applied [142].

Plasma shielding of the electric field is accounted for using the model developed by Matsuoka [143]. In this model, the plasma is separated into 3 regions with different dielectric properties, as depicted in Fig. 4.13. The dielectric constant of the bulk plasma is given by the perpendicular component of the cold plasma dielectric tensor, where ω_{pe} is the electron plasma frequency and ω_{ce} is the electron cyclotron frequency. Poisson's equation is solved across all three regions to find the electric field inside the plasma.

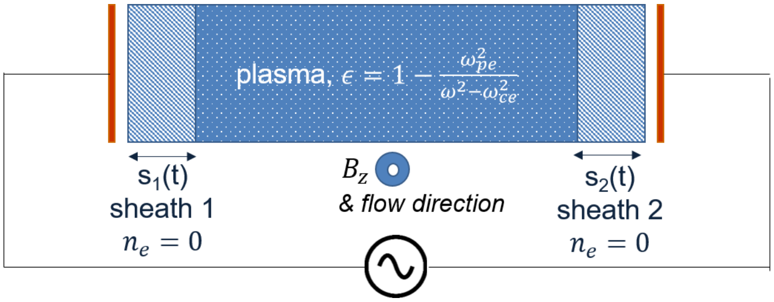

Figure 4.13: This diagram shows the three plasma regions between parallel plate electrodes.

The electric field inside the plasma can then be related to the vacuum electric field ($E_{vac} = V_0/d$) as given in Eq. (4.13), through the non-dimensional shielding parameter, q, which depends on the plasma and electrode properties.

$$E_p = E_0 \left(\frac{2\sqrt{1+q} - 1}{q} \right) \tag{4.13}$$

When $q \ll 1$, the electric field within the plasma is indistinguishable from the vacuum field created by parallel plates. The shielding parameter is calculated for a range of parameters that could be expected in the ICH stage and the results are shown in Fig. 4.14. In the strong magnetic field case, the shielding parameter remains negligible for all plasma densities. Thus, according to this model, the parallel plate electric field should fully penetrate the plasma. The electric field in the region under the antenna is therefore modeled as a spatially uniform and sinusoidally time-varying field of arbitrary phase, ϕ_0, between parallel plates located at the radial edges of the plasma (Eq. (4.14)).

$$\vec{E}(\vec{x}, t) = \frac{V_0}{d} cos(\omega_{ci} t + \phi_0)\hat{y} \tag{4.14}$$

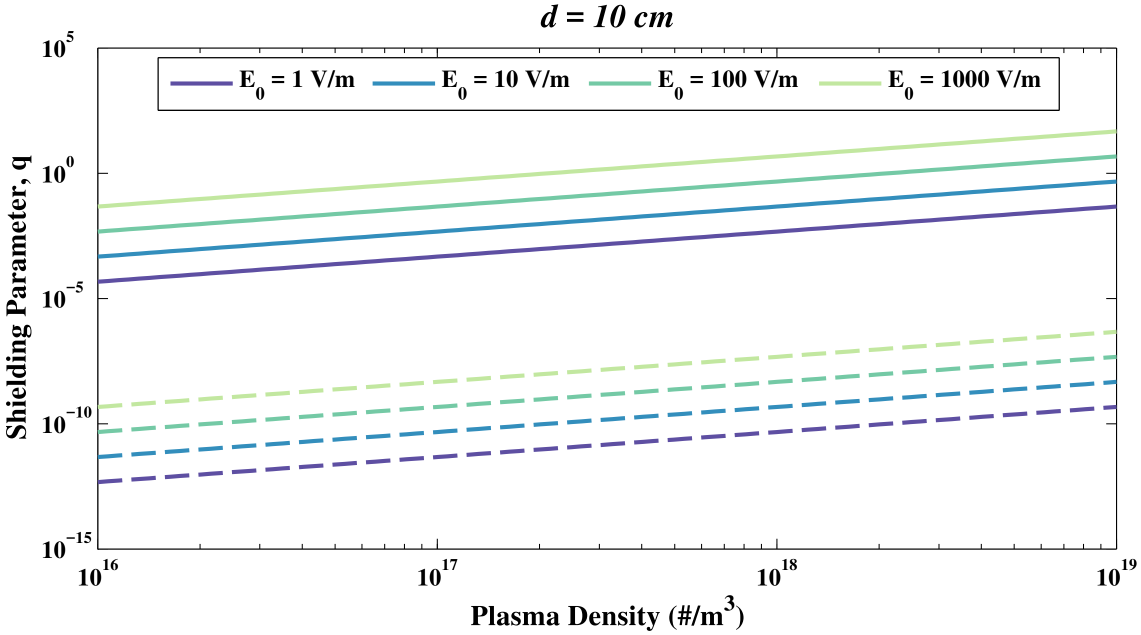

Figure 4.14: Shielding parameter for magnetic field strengths of 100 Gauss (solid lines) and 1 Tesla (dotted lines) for a range of electric field strengths and plasma densities.

4.4.4 Particle Trajectory Model

The trajectories of individual test particles are calculated throughout the ICH heating and magnetic nozzle regions. The inputs to the trajectory model are the particle's initial conditions $(\vec{x_0}, \vec{v_0})$, the external electric field in the solution domain, and the magnetic field profile. The particle trajectory is calculated via numerical integration using the Boris Method [144]. In this case, the only forces that act on the particles once they enter the ICH stage are due to the applied electric and magnetic fields. No forces due to internal plasma fields nor pressure gradients are captured.

4.4.5 Simulation Constraints and Input Parameters

The strength of the electric field, magnetic field, and the antenna length are coupled through the desired performance parameters. The process by which each parameter is determined for the simulation is outlined below:

1. **Performance Parameters:** The desired specific impulse, I_{sp} and device radius, r, are specified. Water ions (H_2O^+) are assumed in this analysis as they are expected to be the primary ion generated in the upstream discharge [145]. The desired final kinetic energy is calculated from the I_{sp}:

$$KE_f = \frac{1}{2} m_i I_{sp}^2 g^2 \tag{4.15}$$

2. **Antenna Length:** The antenna must have an axial extent that allows a plasma ion to complete several cyclotron revolutions as it passes through. As a starting point, ten revolutions are required. This allows for any initial phase difference between the incoming ion velocity vector and the electric field to be corrected within the first few cycles and then several cycles of maximally efficient heating when aligned. This parameter may be adjusted and optimized through future analyses. It is assumed that the ions travel across the constant magnetic field region (representing the throat of a magnetic nozzle) at their acoustic speed ($v_{0||} = \sqrt{\frac{eT_e}{m_i}}$).

The antenna length, L_{ant}, is thus given by:

$$L_{ant} = 10 \left(\frac{2\pi}{\omega_{ci}} \right) v_{0||} \tag{4.16}$$

This is also the length over which the magnetic field should be approximately constant and thus determines the solenoid length (or Helmholtz coil sizing). For this analysis, an electron temperature of 5 eV is assumed, which leads to an antenna length of **3.4 cm**.

3. **Electric Field:** The strength of the electric field required to heat the particles can be related to the desired final kinetic energy, the number of cycles under the antenna, and the antenna frequency. A simple expression for the electric field can be derived for the case where the particle and electric field are in phase at the start of the antenna region:

$$\varepsilon_{ICH} = \frac{1}{2} m_i \left(v_{f\perp}^2 - v_{0\perp}^2 \right) = eE_p(\frac{2\pi}{\omega_{ci}}) \left(\frac{v_{f\perp} - v_{0\perp}}{N} \right) \int_0^N cos^2(2\pi N')N'dN' \tag{4.17}$$

where N is the number of revolutions completed by the particle while transiting the heating region. Note that for the conditions analyzed in this study, phase-matching is typically achieved within two periods of oscillation.

When $v_{f\perp} \gg v_{0\perp}, v_{0||}$, Eq. 4.17 can be simplified to solve for E_0 as a function of the desired Isp ($v_{f\perp} \approx I_{sp}g$). Recall that in this case, $E_0 = E_p = \frac{V_0}{d}$.

$$E_0 \approx \frac{B_{ICH} I_{sp} g}{4\pi} \left(\frac{N}{\alpha(N)} \right) \tag{4.18}$$

with $\alpha(N) = \int_0^N cos^2(2\pi N')N'dN'$.

A plot of the resulting specific impulse as a function of the electric field across the plates is shown in Fig. 4.15, for three different antenna sizes. The middle antenna length, 3.4 cm, corresponds to N = 10 cycles when the particle enters in phase with the electric field.

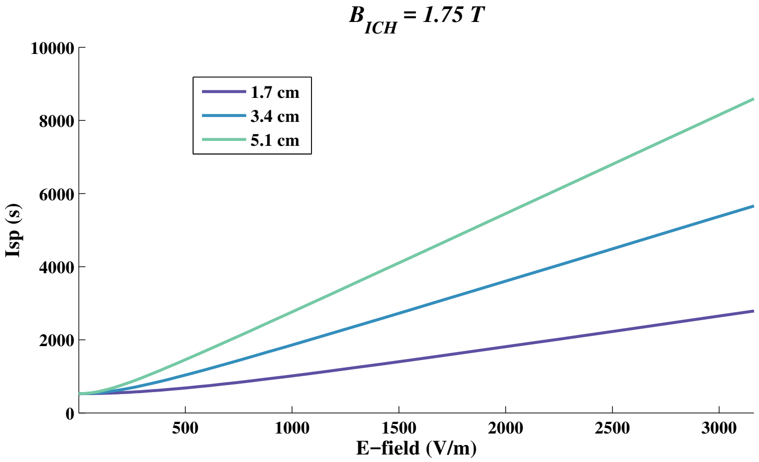

Figure 4.15: Specific impulse as a function of oscillating electric field strength for three different antenna lengths.

4. **Magnetic Field:** A time-invariant magnetic field that is approximately constant in the heating region can be generated using a solenoid or Helmholtz coil. The coil current, number of turns, and axial extent are specified and the 3D components of the magnetic field are calculated throughout the simulation domain. For the present analysis, the solenoid magnetic field shown in Fig. 4.11 is used.

5. **Particle Trajectory:** Initial conditions are specified for each particle at the beginning of the ICH region. The particles are assumed to have an initial per-

pendicular velocity, $v_{i\perp,0} = \sqrt{\frac{eT_{i,0}}{m_i}}$ where $T_{i,0} = 0.025$ eV. Cases are evaluated where the particle velocity is both in and out of phase with the electric field when entering the antenna region to assess the influence of phasing on heating efficiency. The particle trajectory is integrated out to 7.5 cm past the last magnetic field coil in these analyses, although the solution domain could be easily extended further.

4.4.6 Simulation Results

The simulated particle trajectory is shown in Fig. 4.16 for the input parameters specified in Table 4.1. Magnetic field contour and streamlines are shown in the background. The evolution of the particle's perpendicular velocity as it traverses the ICH region is also shown in Fig. 4.17. The particles simulated in this case start approximately on axis (offset by the particle's initial Larmor radius).

Table 4.1: Simulation parameters: on-axis, in-phase

B_{ICH}	T_e	L_{ant}	$z_{0,ant}$	*Desired* I_{sp}	E_0	$\vec{x}_0$	$\vec{v}_0$
1.68 T	5 eV	3.4 cm	2.05 cm	5000 s	3000 V/m	(0, 56.8, 0) μm	(-365, 0, 5160) m/s

A second particle is simulated for this case with initial conditions that are phase-shifted 180^o from the previous particle. The final increase in total kinetic energy for the in-phase particle differs from that of the out-of-phase particle by less than 0.1 %. Therefore we conclude that for these conditions, the effect of particle

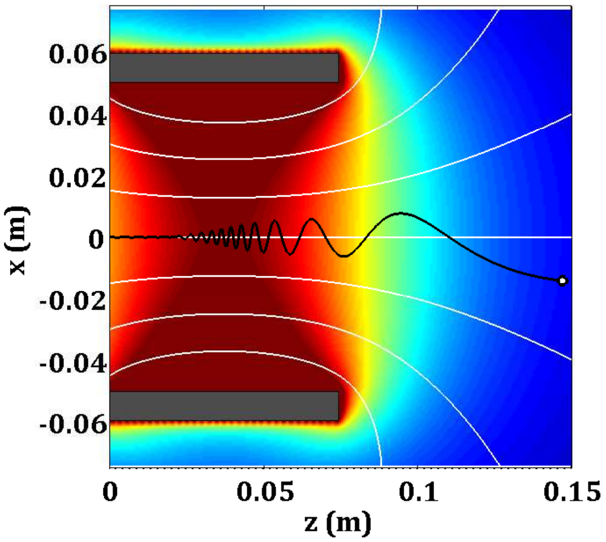

Figure 4.16: Trajectory traced out by a charged water ion with simulation parameters listed in Table 4.1.

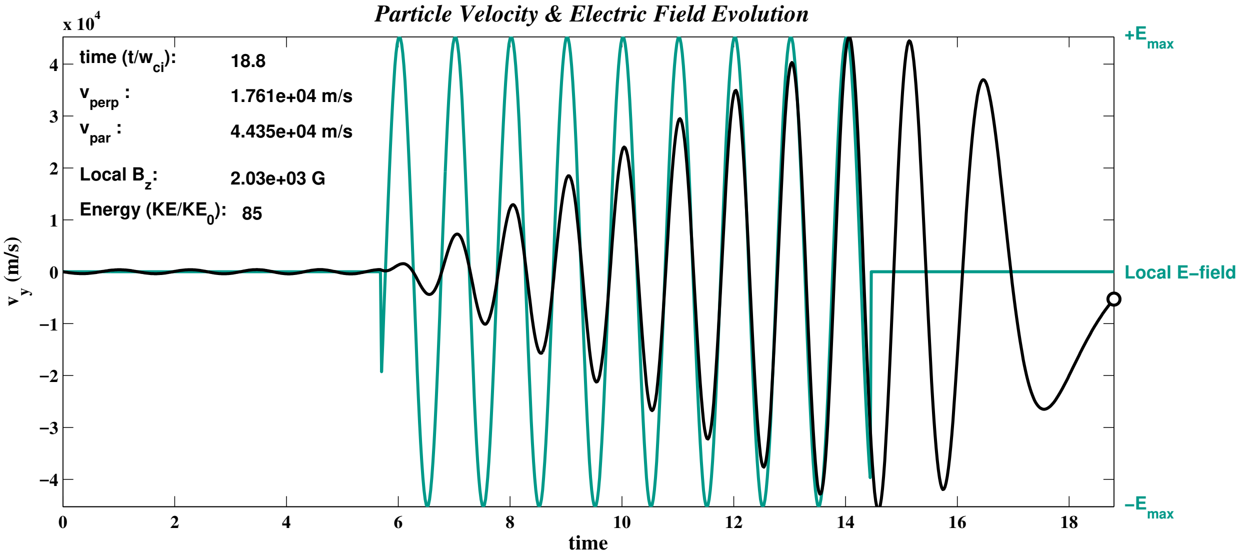

Figure 4.17: Plot of evolution of charged water ion velocity for simluation parameters listed in Table 4.1.

phasing is negligible.

At the final simulation time, the parallel velocity of the particle is 44,350 m/s.

If the particle were able to follow the magnetic field line until all perpendicular kinetic energy could be converted to parallel energy, the particle Isp would be 4870 s. The Isp falls short of the 5000 s design point because of imperfect RF energy absorption.

The Larmor radius of the particle as a function of z-position is shown in Fig. 4.18. At the end of the simulated region, the magnetic field is still quite high (2030 Gauss) and the Larmor radius has grown to only 1.6 cm. Future analyses could include trajectory calculations for particles at the radial edges of the plasma to assess the effects of both wall losses and magnetic field divergence on efficiency.

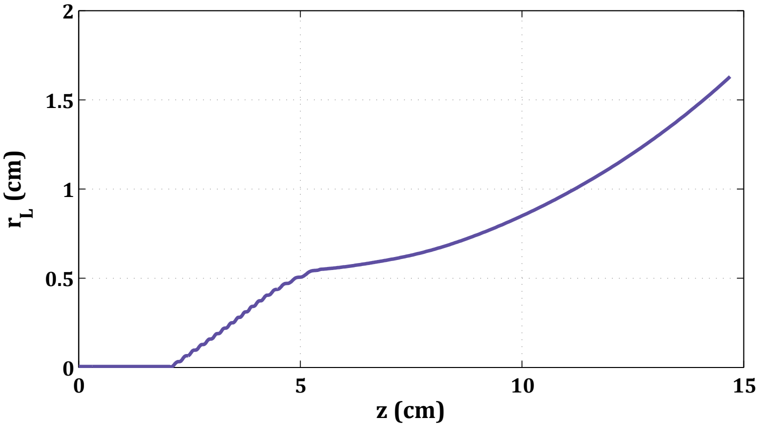

Figure 4.18: Evolution of the Larmor radius as the particle traverses the ICH stage into the magnetic nozzle region.

4.4.7 Summary of ICH Particle Analysis

A tool has been developed to study the trajectories of plasma particles in the ion cyclotron resonance heating stage of an electrodeless plasma thruster. Externally applied electric and magnetic fields are specified in the simulation region. The position and velocity of the charged particle, a water ion in this case, is integrated across the simulation domain for a set of initial conditions. The kinetic energy absorption and conversion of perpendicular to parallel velocity are captured through these calculations.

A test case for a particle starting at the centerline of the thruster is presented. Future work should include expansion to particles at all starting radial locations. The results could be generalized to a thruster configuration by incorporating common radial density distributions for electrodeless thrusters.

Further development of the model should take into account collisions between water ions and background plasma and neutral species. Particle-in-cell or magnetohydrodynamic methods are required to properly model electric field penetration and ion plume evolution and are discussed in the next chapter.

Chapter 5: Effects of Plasma Chemistry on Acceleration Efficiency

This Chapter has been accepted to and will be published in the following conference proceedings:

Petro, E., Brieda, L., and Sedwick, R.,
PIC Simulations of Chemistry Effects
in an Electrodeless Water Plasma Thruster,
55th AIAA/SAE/ASEE Joint Propulsion Conference,
19-22 August, Indianapolis, Indiana

5.1 Overview

In earlier analyses, second order plasma chemistry reactions were ignored under the assumption that in a low pressure discharge, ions would leave the system before colliding with other particles. In this chapter, this assumption is relaxed and the effects of secondary collisions with neutrals and electrons on ion populations are considered. First, a zero-D particle balance analysis is performed for the bulk plasma to predict the ion species fractions as a function of the neutral density. Next, particle-in-cell simulations are employed to predict the effect of plasma chemical reactions, specifically charge exchange, on acceleration efficiency in an electrodeless thruster.

5.2 Relevant Work

Nakamura et. al. [146] performed particle-in-cell simulations of heating and plasma generation for a CubeSat scale microwave (ECR) water plasma thruster which indicate a similar composition as was predicted in Chap. 3 of this work. Their simulations predict the dominant ions in the discharge to be H_2O^+ (∼80%) and OH^+ (∼15%) for conditions that include neutral densities $\sim 10^{20}$ particles/m^3 and electron temperatures varying spatially between 3 and 16 eV.

However when pressures are higher or diffusion conditions different than those above, the formation of the hydronium ion, H_3O^+, is known to be important. For example, a water plasma discharge has been studied for the purposes of environmentally-friendly UV light source via OH excitation wherein higher pressures are considered (150 Pa or $n_{H_2O} \approx 10^{22}$ particles/m^3) [147]. In this regime, H_3O^+ becomes the dominant positive ion, created in the fast charge exchange reaction: $H_2O^+ + H_2O \longrightarrow H_3O^+ + OH$ [148]. Here H_3O^+ outnumbers H_2O^+ and other ions by over an order of magnitude. The steady-state densities will depend both on the rates of formation and the transport properties of different species, which are unique to the discharge characteristics and geometry.

The study in [146] also included the charge exchange reaction [149] in their MCC chemistry modeling but did not find a substanial population in the plasma generation region. However, they only consider an axial distance of 4 mm from the ECR antenna and thereby do not resolve the acceleration and expansion regions where chemical reactions such as charge exchange are known to be important to the evolution of plasma plumes. For example, the reaction rate for this process from [149] is predicted to be as large as $10^{-19}\ m^2$ and thus is on the same order of magnitude of the Xe-Xe$^+$ charge exchange reaction [150]. Charge exchange has been studied extensively in Hall thrusters and ion engine plumes. Charge exchange ions will reduce thrust efficiency and Isp when formed in the acceleration region and can lead to unwanted spacecraft-plume interactions when formed downstream. In a single-stage helicon thruster it will affect the linear acceleration efficiency. In a two-stage thruster with ion cyclotron heating, it will cause losses in rotational ion energy and will therefore negatively impact heating efficiency. Thus a more thorough look at the H_3O^+ charge exchange reaction across the elecrodeless thruster operating space is critical for accurately predicting and optimizing performance.

5.3 Plasma Composition

5.3.1 Importance of Collisions

In the plasma regimes common to electric propulsion, collisions of interest include (1) electron-neutral, (2) ion-neutral, and (3) ion-ion, roughly in order of descending rates. The most common ion-neutral reaction studied in plasma thrusters is charge exchange. When the plasma is generated using a noble gas, the charge exchange process is always symmetric with respect to mass and composition. A fast ion collides with a slow neutral and the charge is transferred to the slow particle. The result is a slow ion and fast neutral (e.g. $A^+(\text{fast}) + A(\text{slow}) \longrightarrow A(\text{fast}) + A^+(\text{slow})$). This process is unimportant for noble gases in the plasma generation region as all particles are relatively slow moving in this region and thus the composition of ions extracted into the acceleration region is unchanged. It does have significance when occuring in the plume as slow moving ions created here are the ones that return to the spacecraft due to stray fields, resulting in backscatter.

In a molecular plasma, the charge exchange process has several pathways, both symmetric and asymmetric with respect to mass and composition. In a water plasma, the H_2O-H_2O^+ collision can proceed through one of two channels (shown also in Fig. 5.1):

$$\text{(I) } H_2O^+ + H_2O \longrightarrow H_2O + H_2O^+;\ \textit{“symmetric charge exchange”}\ \text{(II)}$$

$$H_2O^+ + H_2O \longrightarrow H_3O^+ + OH;\ \textit{“proton transfer”}$$

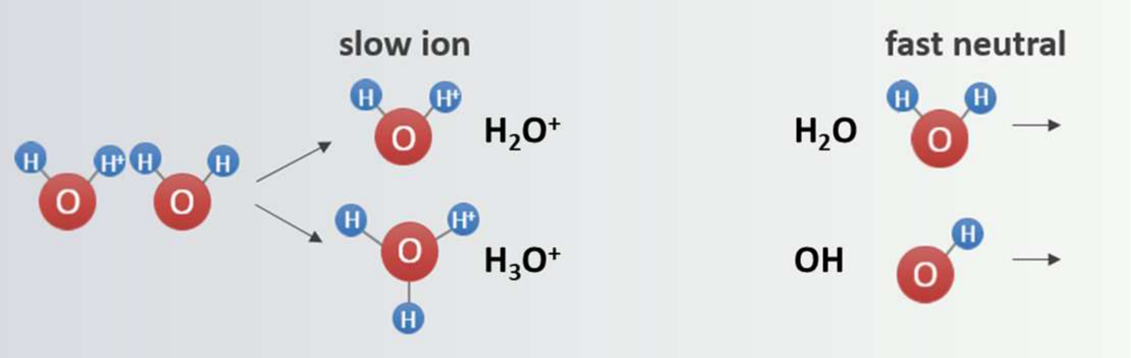

Figure 5.1: H_2O-H_2O^+ collisions resulting in I: symmetric charge exchange or II: proton transfer.

In channel II, there are two possible results. Either the ion may transfer an H^+ proton to the neutral (resulting in a fast OH neutral and slow H_3O^+ ion) or the ion can pick up a proton from the neutral, leaving as a fast H_3O^+ ion. The cross-sections for both pathways have been measured and the former (resulting in a slow ion) is found to occur about 1 order of magnitude more frequently [149]. The cross-sections between the two channels (I & II) overall are comparable, with channel I being slightly higher but unimportant for predicting plasma composition.

Note that there are two types of reaction rates from the literature for the proton transfer reactions. There is a thermal rate (measured by various sources as indicated later in the chapter) for ions and neutrals colliding when around room temperature in a thermalized distribution. This rate is appropriate for collisions in the bulk of the plasma discharge and is the rate used to predict plasma composition. In this case, the rate for channel II is the only rate of interest as the collision of a slow ion and a slow neutral has no effect on the composition. Another set of rates (specifically cross-sections) are reported for collisions between fast ions and a neutral population [149]. This dataset is used in the acceleration efficiency section where ions have gained substantial momentum. Fig. 5.2 shows the rates ($k = \langle \sigma v \rangle$) reported in various sources as a function of the collision velocity.

Another collision of unique importance in molecular plasmas is the dissociative recombination reaction between electrons and ions. In the noble gas plasmas, recombination of ions can typically be neglected to first order as it is a 3-body process that occurs infrequently in the density regime of interest for plasma thrusters. In contrast, molecular ions may be destroyed in the 2-body collision between an electron and a water (or hydronium) ion, e.g. $\mathrm{e} + \mathrm{AB}^+ \longrightarrow \mathrm{A} + \mathrm{B}$. This process may limit the overall plasma density achievable in a water-based discharge.

Thus, the effects of these and other pertinent plasma-chemical reactions are considered in the context of predicting the plasma composition and acceleration

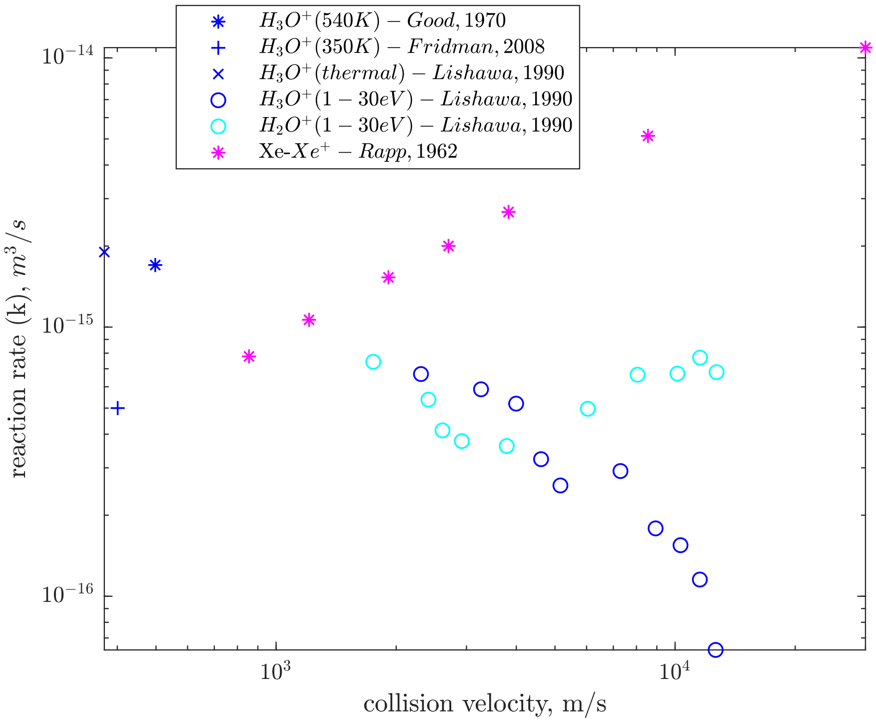

Figure 5.2: H_2O-H_2O^+ reaction rates from various datasets for both thermal and suprathermal ion energies.

efficiency.

5.3.2 Preliminary Analysis

To motivate the more detailed analysis and briefly assess the parameter space of neutral density and ionization fraction, a zero-D estimation of water discharge charge-exchange effects has been performed. Rate equations are developed for the ion species considering the charge exchange pathway in which a proton is transferred to the neutral: $H_2O^+ + H_2O \longrightarrow H_3O^+ + OH$:

$$\frac{\partial n_{H_2O^+}}{\partial t} = n_e n_{H_2O} k_{H_2O^+}(T_e) - C_{H_2O^+} n_{H_2O^+} - n_e n_{H_2O^+} k_{H_3O^+}(T_e) - n_e n_{H_2O^+} k_{diss,H_2O^+}(T_e) \tag{5.1}$$

$$\frac{\partial n_{H_3O^+}}{\partial t} = n_e n_{H_2O^+} k_{H_3O^+}(T_e) - C_{H_3O^+} n_{H_3O^+} - n_e n_{H_3O^+} k_{diss,H_3O^+}(T_e) \qquad (5.2)$$

where the C_i is the ion-specific diffusion coefficient for thermal diffusion in a cylindrical discharge as described in [147] and $k_{diss,i}$ is the reaction rate for the dissociative recombination process. These equations are solved in steady state for a range of ionization fractions and neutral particle densities. Results (Fig. 5.3) indicate that H_3O^+ could indeed form in non-negligible concentrations in discharge conditions of interest to the thruster community. The neutral density conditions of several relevant studies [87, 102, 147] are highlighted in the plot.

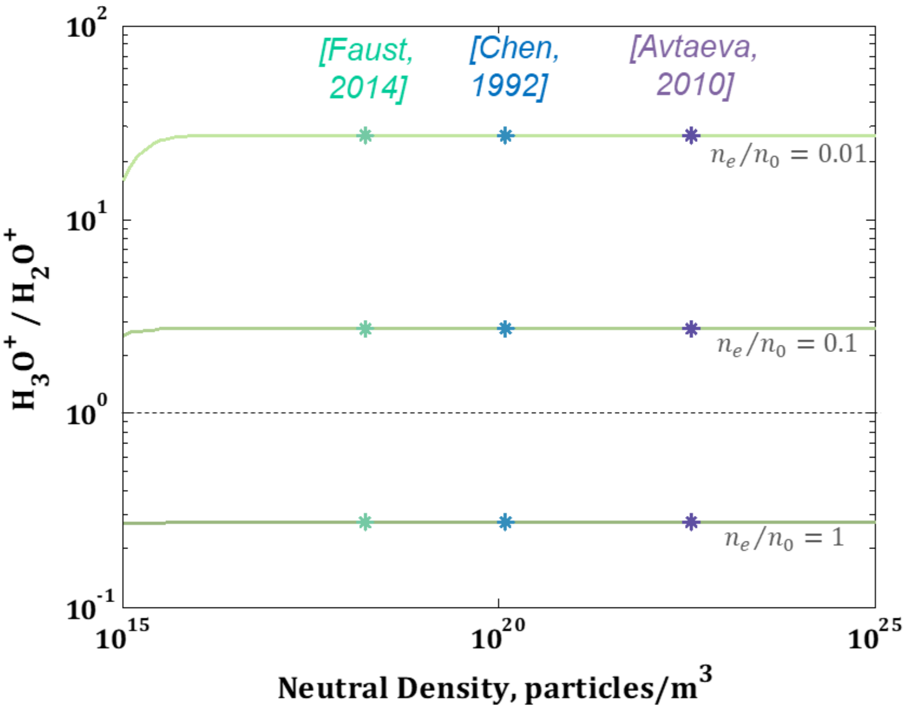

Figure 5.3: Predictions for steady-state H_3O^+/H_2O^+ ion fractions for a range of discharge conditions.

5.3.3 Matrix Approach

The analysis presented in the previous section is extended to consider a wider range of reactions and to test the assumption that H_2O^+ and H_3O^+ are indeed the dominant ions. The complete set of reactions involving the highest order positive and negative ions are listed in Table 5.1 below.

The set of volume rate equations is written for each positive and negative ion as:

$$\frac{\partial n_i}{\partial t} = \sum_{j=1}^{j=n} (source(n_j) - sink(n_j)) - n_i C_i \tag{5.3}$$

where the *source* and *sink* reactions come from Table 5.1 and C_i is again the ion-specific diffusion term. Note that this formulation is an extended version of the analysis performed in Section 5.3.2.

In steady state ($\frac{\partial n_i}{\partial t} = 0$), a set of linear equations can be formed such that:

$$\begin{bmatrix} n_e n_0 < \sigma_i v_e > \\ \vdots \\ n_e n_0 < \sigma_n v_e > \end{bmatrix} = \begin{bmatrix} C_i + n_e k_{e,i} + n_0 k_{0,i} & n k_j & n k_n \\ \vdots & \ddots & \vdots \\ C_n + n_e k_{e,n} + n_0 k_{0,i} & n k_j & 0 \end{bmatrix} \begin{bmatrix} n_i \\ \vdots \\ n_n \end{bmatrix} \tag{5.4}$$

where the terms on the LHS represent the creation of ions from neutrals (n_0 being the neutral density), and terms on the RHS represent the changes in populations due to collisions between ions of each type (n_j) and neutrals (n_0) or electrons (n_e).

The rates specified in Table 5.1 for electron temperatures of 5 eV are used and the matrix outlined in Eq. 5.4 is inverted to find the normalized species fractions

Table 5.1: Reaction rates used to determine plasma composition

ionization, $< \sigma v >$

reactant (fluid)	reactant (fluid)	product (fluid)	product (kinetic)	$T_e = 5$ eV	[Ref]
e	H_2O	2e	H_2O^+	1.36E-15	[106]
e	H_2O	2e	OH^+	1.37E-16	[106]
e	H_2O	2e	H^+	3.86E-17	[106]

dissociative attachment, $< \sigma v >$

reactant (fluid)	reactant (fluid)	product (kinetic)	product (kinetic)	$T_e = 5$ eV	[Ref]
e	H_2O	H	OH^-	3.63E-18	[106]
e	H_2O	H_2	O^-	1.59E-17	[106]
e	H_2O	OH	H^-	9.03E-17	[106]

detachment, $< \sigma v >$

reactant (fluid)	reactant (kinetic)	product (fluid)	product (kinetic)	$T_e = 5$ eV	[Ref]
e	OH^-	2e	OH	–	–
e	O^-	2e	O	1.05E-13	[151]
e	H^-	2e	H	1.50E-13	[152]
e	H^-	2e	H	3.07E-13	[148]

charge exchange and proton transfer, σ or k

reactant (fluid)	reactant (kinetic)	product (fluid)	product (kinetic)	thermal (k, m^3/s)	1 eV (σ, m^2)	30 eV (σ, m^2)	[Ref]
H_2O	H_2O^+	H_2O (fast)	H_2O^+ (slow)	1.90E-15	4.20E-19	6.00E-20	k: [149] σ: [149]
H_2O	H_2O^+	H_2O (fast)	H_3O^+ (slow)	1.70E-15 5.00E-16	3.00E-19	1.00E-20	k: [153], [148] σ: [149]
H_2O	OH^+	OH (fast)	H_2O^+ (slow)	3.00E-15			[154]
H_2O	H^+	H (fast)	H_2O^+ (slow)	3.00E-15			[154]
H_2O	H^-	H_2 (fast)	OH^- (slow)	3.80E-15			[154]

dissociative recombination, $< \sigma v >$

reactant (fluid)	reactant (kinetic)	product (fluid)	product (fluid)	$T_e = 5$ eV	Model	[Ref]
e	H_2O^+	H	OH	1.3E-16	0.66E-13×(0.01/Te)	[155]
e	H_2O^+	H_2	O	6E-17	0.3E-13×(0.01/Te)	[155]
e	H_2O^+	2H	O	4.8E-17	0.24E-13×(0.01/Te)	[155]
e	H_3O^+	H	H2O	2.4E-15	1.E-12×0.026/Te)	[155]
e	OH^+	O*	H	2.7E-15	0.6E-14/$T_e^{0.5}$	[156]

(n_i/n_0) for a range of ionization fractions (n_e/n_0). Results are shown in Table 5.2 for 3 different neutral densities: $n_0 = [10^{18}, 10^{20}, 10^{22}]$ and 3 different ionization fractions at each plasma density: $n_e/n_0 = [0.01, 0.1, 1]$.

Table 5.2: Ion densities from matrix solution

$n_0 = 10^{18}$

n_e/n_0	0.01	0.1	1
$n_{H_2O^+}$	4.3E-06	4.3E-05	4.3E-04
n_{OH^+}	3.1E-07	3.1E-06	3.1E-05
n_{H^+}	7.4E-09	7.4E-08	7.4E-07
n_{OH^-}	8.4E-09	8.4E-08	8.4E-07
n_{H^-}	1.7E-08	1.7E-07	1.7E-06
n_{O^-}	4.9E-08	4.9E-07	4.9E-06
$n_{H_3O^+}$	5.7E-10	5.7E-09	5.7E-08
$n_{H_3O^+}/n_{H_2O^+}$	0.00013	0.00013	0.00013
n_{i^+}/n_{i^-}	63	63	63

$n_0 = 10^{20}$

n_e/n_0	0.01	0.1	1
$n_{H_2O^+}$	1.8E-02	1.7E-01	1.3E+00
n_{OH^+}	3.8E-04	2.9E-03	8.1E-03
n_{H^+}	4.7E-05	4.7E-04	4.7E-03
n_{OH^-}	2.4E-04	1.4E-04	4.1E-05
n_{H^-}	1.4E-04	5.9E-04	8.6E-04
n_{O^-}	8.7E-05	1.0E-04	1.1E-04
$n_{H_3O^+}$	2.3E-02	1.4E-01	2.4E-01
$n_{H_3O^+}/n_{H_2O^+}$	1.24082	0.80781	0.17992
n_{i^+}/n_{i^-}	87	381	1569

$n_0 = 10^{22}$

n_e/n_0	0.01	0.1	1
$n_{H_2O^+}$	3.0E-02	2.8E-01	1.9E+00
n_{OH^+}	4.4E-04	3.2E-03	8.4E-03
n_{H^+}	1.3E-04	1.3E-03	1.3E-02
n_{OH^-}	1.8E-03	2.0E-04	4.2E-05
n_{H^-}	9.0E-04	9.0E-04	9.0E-04
n_{O^-}	1.1E-04	1.1E-04	1.1E-04
$n_{H_3O^+}$	6.3E-01	5.9E-01	4.0E-01
$n_{H_3O^+}/n_{H_2O^+}$	20.80049	2.08300	0.20833
n_{i^+}/n_{i^-}	234	727	2230

It can be seen from these results that, across the parameter space, H_2O^+ and H_3O^+ are the dominant positive ions in steady-state. Additionally, positive ions outnumber negative ions by over 1 order of magnitude for all cases. The ratio between H_2O^+ and H_3O^+ ions changes based on the conditions as expected and in the same way as was shown in the simplified preliminary analysis in Section 5.3.2. However, it is important to note that these results generally do not represent quasi-neutral solutions. A quasi-neutral solution requires:

$$n_e/n_0 = \sum n_{i^+}/n_0 - \sum n_{i^-}/n_0 \tag{5.5}$$

Thus while these are possible plasma states for non-neutral conditions, we expect quasi-neutrality to hold in the bulk of the ionization volume and thus are interested in finding self-consistent, quasi-neutral results. To demand quasi-neutrality, one must rewrite the electron density in the system of rate equations in terms of each ion species according to Eq. 5.5. This substitution results in a highly non-linear set of rate equations. Several approaches can be taken to solve this system:

1. Solve set of equations using *implicit* approaches

2. Propagate a time-dependent solution *explicitly* until reaching steady-state

3. Solve the matrix as above but iterate over n_e/n_0 until quasi-neutral solution is found

4. Reduce the variable space to solve a reduced set of equations

Both approaches (3) and (4) above were implemented. The results from both agree, but the approach in (4) allows for greater physical insight and is thus presented in the next section.

5.3.4 Reduced Problem

The results presented in Table 5.2, though non-neutral, confirm that H_2O^+ and H_3O^+ exceed all other positive and negative ions by at least 1 order of magnitude. Thus an approximate quasi-neutral solution is given by: $n_e \simeq n_{H_2O^+} + n_{H_3O^+}$. Likewise, the full non-linear problem may be reduced to consider just the rate equations for these two species. The reduced set of equations is given by Eq. 5.6 and Eq. 5.7.

$$\frac{\partial n_1}{\partial t} = (n_1 + n_2)\, n_0 k_{ion,1} - C_1 n_1 - n_1 n_0 k_{1\to 2} - n_1 (n_1 + n_2)\, k_{diss,1} = 0 \tag{5.6}$$

$$\frac{\partial n_2}{\partial t} = n_1 n_0 k_{1\to 2} - C_2 n_2 - n_2 (n_1 + n_2)\, k_{diss,2} = 0 \tag{5.7}$$

where species “1” is H_2O^+, species “2” is H_3O^+, $k_{1\to 2}$ represents the reaction rate for $H_2O^+ + H_2O \longrightarrow H_3O^+ + OH$, and $(k_{diss},\ k_{ion})$ represent reaction rates for dissociative recombination and ionization averaged over a Boltzmann electron population.

Though still nonlinear, this set of quasi-neutral equations can be combined and reduced to one variable and solved numerically, giving the ion densities of H_2O^+ and H_3O^+ for a range of neutral densities. The variable space over which solutions can be found is still wide. The dependence of the solution on diffusion (C_i) assumptions, reference-specific cross-sections, and electron temperatures is explored.

5.3.4.1 Diffusion Model Dependence

Results are shown in Fig. 5.4 for two different diffusion models for an electron temperature of 5 eV. The diffusion model shown in (a) is the same as assumed in previous sections: thermal diffusion through a background population of neutrals. The diffusion model in (b) is for a faster diffusion rate which matches the rate at which ions travel into sheaths at each boundary. The particular results shown assume a discharge tube of 5 cm in radius by 10 cm in length, similar to experimental prototypes being built [100, 102].

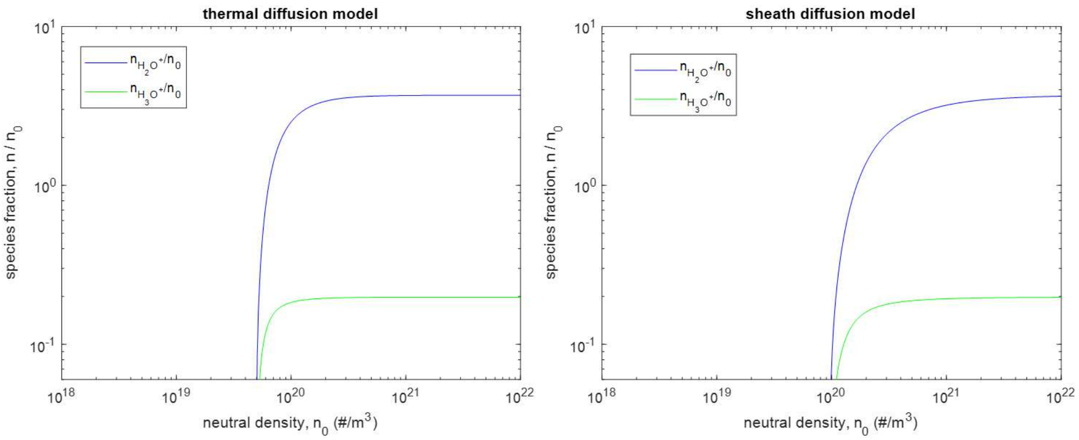

(a) (b)

Figure 5.4: Comparison of predicted H_3O^+ and H_2O^+ ion densities for different diffusion models.

The effect of the diffusion model is to determine the minimum cut-off density for which plasma can be sustained. Below this cut-off, plasma ions diffuse out of the system more quickly than they can be replenished. For both diffusion models, the solution evolves rapidly with neutral density beyond the cut-off and asymptotes to a particular value. In this regime, the losses of ions due to diffusion are overcome by losses due to the chemical processes in the plasma. In both cases, the diffusion rates of H_3O^+ and H_2O^+ ions are very similar and thus the predicted ion ratio is equivalent between the two cases: 18.6 H_2O^+ ions for each H_3O^+ ion.

5.3.4.2 Reaction Rate Dependence

The asymptotic solution above predicted a maximum ratio of 18.6 H_2O^+ to H_3O^+ ions when the thermal charge exchange rate in [148] is used. However, the predicted ion ratio is found to strongly depend on the cross-section used and various values are reported in the literature. If the value from another source [153] is used instead, the predicted asymptotic solution changes and the predicted maximum ratio is instead 2 H_2O^+ ions for each H_3O^+ ion. Fig. 5.5 comapres the solutions for the predicted thermal charge exchange cross sections using (a) 5e-16 m^3/s [148] and (b) 1.7e-15 m^3/s [153]. Thus a factor of ∼4 increase in the predicted reaction rate results in a factor of ∼10 difference in the predicted ion ratios.

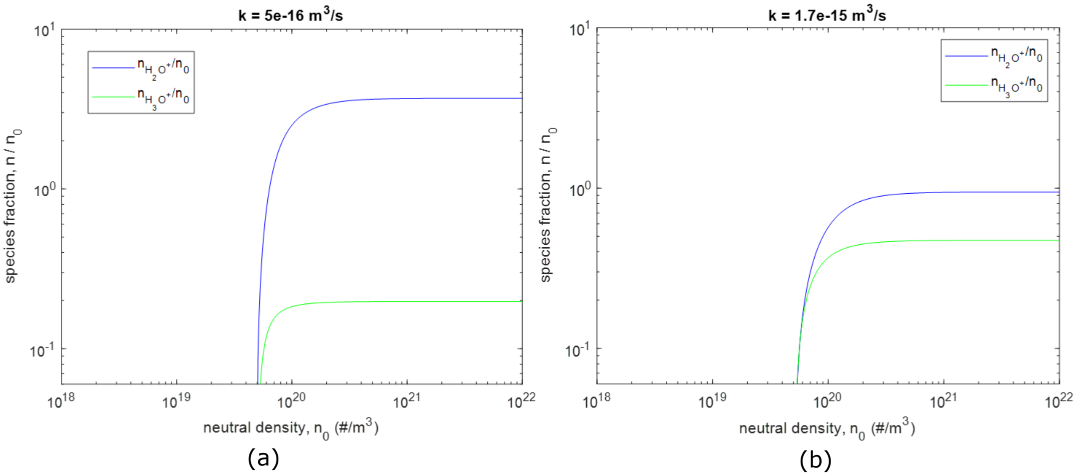

(a) (b)

Figure 5.5: Comparison of predicted H_3O^+ and H_2O^+ ion densities for different CEX rates.

5.3.4.3 Electron Temperature Dependence

While the charge exchange reaction rate depends on the energies of the H_2O^+ ions and the neutrals, all of the other rates depend on the electron temperature. All previous results in this chapter assumed an electron temperature of 5 eV. Recall from Chap. 3 that this electron temperature is desirable for good thrust efficiency in a single-stage system. Here the predicted ion composition is evaluated for 3 different electron temperatures: $T_e = [2, 5, 10]$ eV. Results shown in Fig. 5.6 give predictions of the plasma composition for the range of electron temperatures shown. Higher electron temperatures correspond to higher plasma densities, H_2O^+ ions dominating, and lower cutoff densities. For the lowest electron temperature (2 eV), H_3O^+ is found to far outnumber H_2O^+ by a factor of 35:1 (for $k_{H_3O^+} = 5\text{e-}16\ m^3/s$) and the total ionization fraction is 2 parts in 1000.

Fig. 5.7 shows the electron temperature dependence for the higher reaction rate predicted in [149]. In this case, the ratio at 2 eV changes to 120:1, H_3O^+ to H_2O^+, while the total ion density remains about the same.

5.3.5 Predicting Plasma Composition: Conclusions

The approach developed in this section lends critical insight into the range of expected water plasma discharge characteristics and the variation expected across key parameters. Within the range of possible charge exchange rates and electron temperatures, there is a wide variation in predicted plasma composition, both in terms of ion densities, and ratios between the dominant ions. The following conclusions are drawn:

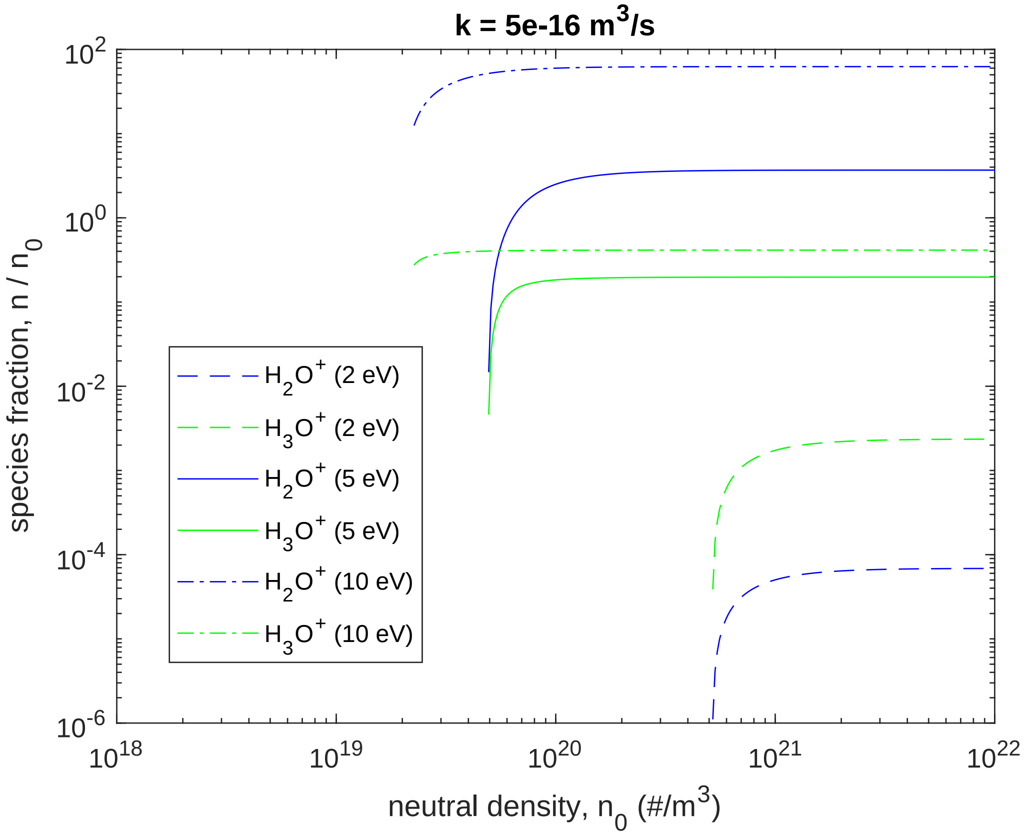

Figure 5.6: Comparison of predicted H_3O^+ and H_2O^+ ion densities for different electron temperatures ($k_{H_3O^+}$ = 5e-16 m^3/s).

- H_3O^+ ions will dominate the discharge at lower electron temperatures (below 5 eV).
- H_2O^+ ions become dominate at higher electron temperatures ($T_e \gtrsim$ 5 eV) and the cross-over point depends on the exact CEX reaction rate assumed.
- High ionization fractions ($n_i/n_0 \approx$1) are only possible for higher electron temperatures ($T_e \gtrsim$ 5 eV).
- In the quasi-neutral framework, the ratio between H_3O^+ and H_2O^+ does not depend explicitly on the neutral density.

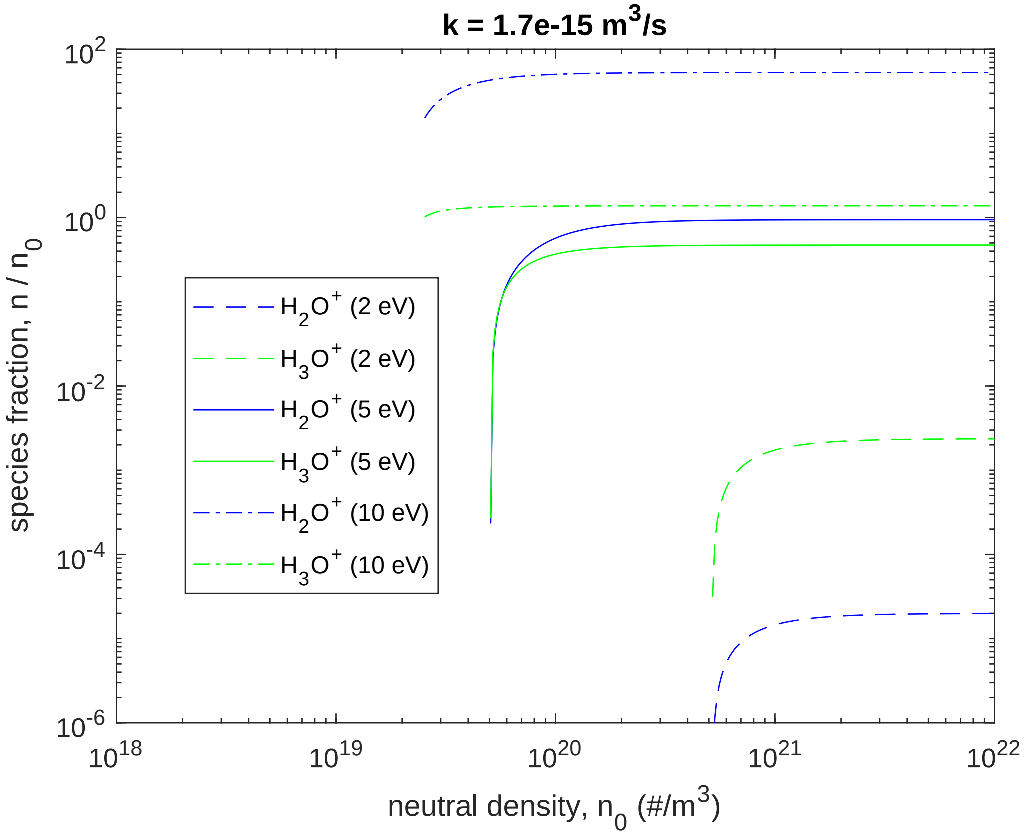

Figure 5.7: Comparison of predicted H_3O^+ and H_2O^+ ion densities for different electron temperatures ($k_{H_3O^+}$ = 1.7e-15 m^3/s).

- Second order plasma chemical reactions (e.g. ion-neutral and ion-electron reactions) are important to the discharge description and should be modeled appropriately.

The reduced order model developed here is a useful tool for predicting the plasma composition as a function of specified discharge conditions, the most important variable being the electron temperature. This model can be used to specify the plasma composition in the bulk of the discharge in place of significantly more complex approaches such as explicit time-evolution of the plasma breakdown. This model captures the impact of plasma chemistry and specifically the

($H_2O^+ + H_2O \longrightarrow H_3O^+ + OH$) reaction on plasma composition.

The compositions predicted with this model can be used to self-consistently specify ion and neutral densities leaving the ionization stage which serve as initial conditions for modeling the acceleration process. In a single-stage electrodeless thruster, acceleration is due to ambipolar forces. These initial plasma conditions could also be used to specify ion properties for gridded acceleration as in the design of [146]. Plume simulations presented in the next section will capture the effects of charge exchange on linear acceleration efficiency. In a two-stage thruster with ion cyclotron heating, knowing the dominant positive ion is critical for designing the resonant frequency. Likewise, the ionization fraction is critical for predicting the prevalence of charge-exchange, momentum reducing collisions in the cyclotron acceleration process. Thus the predictions by the reduced model could also be used as inputs in future ion cyclotron heating simulations.

The approach developed here has allowed us to decouple the plasma generation and acceleration processes and determine appropriate initial conditions for detailed studies of the plume evolution.

5.4 Acceleration Efficiency Studies

5.4.1 Approach

A 2D, axisymmetric particle-in-cell model was employed to investigate the effects of charge exchange and other pertinent chemical reactions in the acceleration and expansion region of water propelled plasma thruster. When charge exchange occurs in the bulk of the plasma it affects the plasma composition. When it occurs in the acceleration region, it affects the acceleration efficiency and thereby the thrust efficiency of the system. The particle-in-cell approach is particularly useful in this regime as it captures density gradients and geometrical effects that will be important for the acceleration efficiency. The open-source platform Starfish [157] v0.20 was used to perform the simulations. Simulations are performed in Cartesian coordinates due to limitations of the software with X representing the axial direction and Y representing the radial direction.

Table 5.3 lists several key reactions included and the collision model to be used for each. For reactions involving electrons and a fluid target (e.g. ionization of background neutrals), an electron temperature-dependent rate coefficient, $k(T_e)$, will be calculated. Reactions between a kinetic species (e.g. ions) and a fluid species (e.g. electrons, background neutrals) are calculated as a function of the ion collision energy assuming $v_e \gg v_i$ and $v_i \gg v_n$, respectively. In the latter case, the set of high energy collision cross-sections for the charge and proton transfer reactions [149] are sampled to calculate the reaction rate.

Two different types of acceleration are studied. The first (shown in Fig. 5.8a) is a gridded acceleration as in an ion engine where electrons are repelled and only ions and neutrals are present. The second (Fig. 5.8b) is an electrodeless acceleration region as in a helicon thruster. There are two main differences between the ambipolar and gridded acceleration cases: (1) the acceleration region is assumed to be longer in the former; and (2) the ambipolar acceleration process is current-free and thus electrons are present. Due to space-charge limitations in the gridded acceleration case, a higher potential difference must be applied to extract the same

Table 5.3: Relevant collisional processes in a water vapor discharge

Reaction	**Species Involved**	**Collisional Model**
Ionization	e, H_2O	$k(T_e)$
Dissociative recombination	e, H_2O^+	$k(T_e)$
	e, H_3O^+	$k(T_e)$
	e, OH^+	$k(T_e)$
Charge exchange	H_2O^+, H_2O	$k(v_i)$
	OH^+, H_2O	$k(v_i)$
	H^+, H_2O	$k(v_i)$
	OH^+, H_2O	$k(v_i)$
	H^-, H_2O	$k(v_i)$

current through the non-neutral acceleration region. The higher accelerating potential results in a higher maximum velocity of the ions. Thus, these two acceleration methods are not directly comparable, but it is of interest to know the effects of charge exchange in each case.

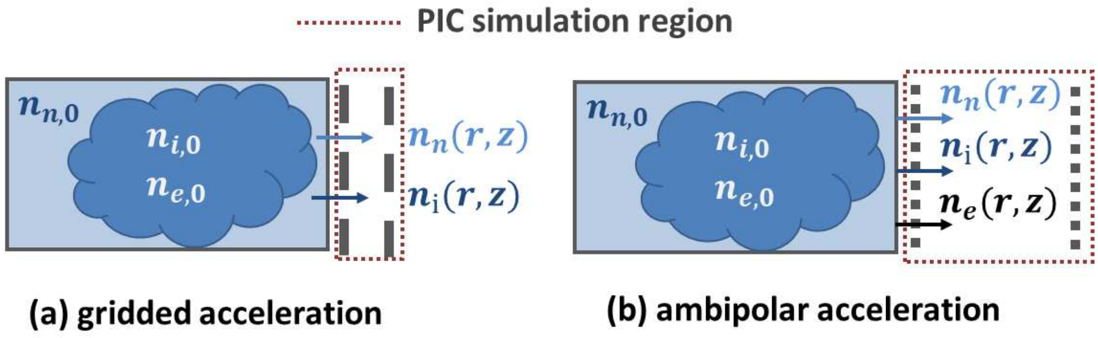

Figure 5.8: Acceleration regions studied using PIC simulations.

5.4.2 Gridded Acceleration

It is hypothesized that the effects of plasma chemistry and specifically charge exchange are less important in gridded thrusters as ions are accelerated over a shorter distance and thus experience fewer collisions with co-streaming neutrals and negligible collisions with electrons. A detailed study into gridded acceleration is not performed here, as it is outside the scope of this thesis. However, one case is presented as a brief look into the topic and to compare qualitatively with the ambipolar cases studied in greater depth.

The conditions simulated are informed by the water-propelled ion engine studied in [158]. The accelerating potential (which must be high due to space-charge limits) is set to **-800 V**. The acceleration grid spacing is **1 mm** which allows the ion density predicted in [158] ($n_i = \mathbf{10}^{16}\ m^{-3}$) to be extracted across the above potential drop in accordance with the Child-Langmuir limit. The initial neutral density is also set to match the value in [158] at $\mathbf{10}^{20}\ m^{-3}$. Note that in the study referenced, the authors did not consider the proton transfer reaction that creates H_3O^+ and thus do not predict any to be present. Ions and neutrals are injected into the simulation domain at the upstream wall with the initial densities listed and drift velocities as specified in Table 5.4.

The minimum simulation time is the time required for the slow neutrals injected at the upstream boundary to pass through the length of the simulation domain. The particle weighting is chosen such that there are many particles per grid cell and the simulation time step is set by the CFL condition ($\frac{1}{\Delta t} \leq \frac{\Delta z}{v_z} + \frac{\Delta r}{v_r}$).

Input files defining the simulation parameters for the above baseline case and the two comparison cases (without collisions, higher density neutrals) are included in Appendix B.

Results from the simulation are included below with Fig 5.9(a)-(c) showing

Table 5.4: PIC Simulation Parameters - Gridded Acceleration

	Parameter	**Value**	
Ions		*H_2O^+*	*H_3O^+*
	initial density	1×10^{16}	0
	initial drift velocity (H_2O^+)	5,000 m/s	–
	initial temperature (H_2O^+)	300 K	–
	particle weighting (H_2O^+)	1×10^{6}	1×10^{3}
Neutrals		*H_2O*	
	initial density	2×10^{20}	
	initial drift velocity	500 m/s	
	initial temperature	300 K	
	particle weighting	1×10^{10}	
Domain		*acceleration grid region*	
	domain size (r,L)	1 cm × 1 mm	
	grid spacing (Δr,Δz)	5×10^{-5}, 5×10^{-4} m	
	potential @ z = 0	0 V	
	potential @ z = L	-800 V	
	time-step (Δt)	5×10^{-10} s	
	total time simulated	50 μs	

the final neutral, H_2O^+, and H_3O^+ densities (top row) and axial velocities (bottom row). Note that contour plots are to scale as a cross-section of 1 mm (z) by 1 cm (r) is modeled.

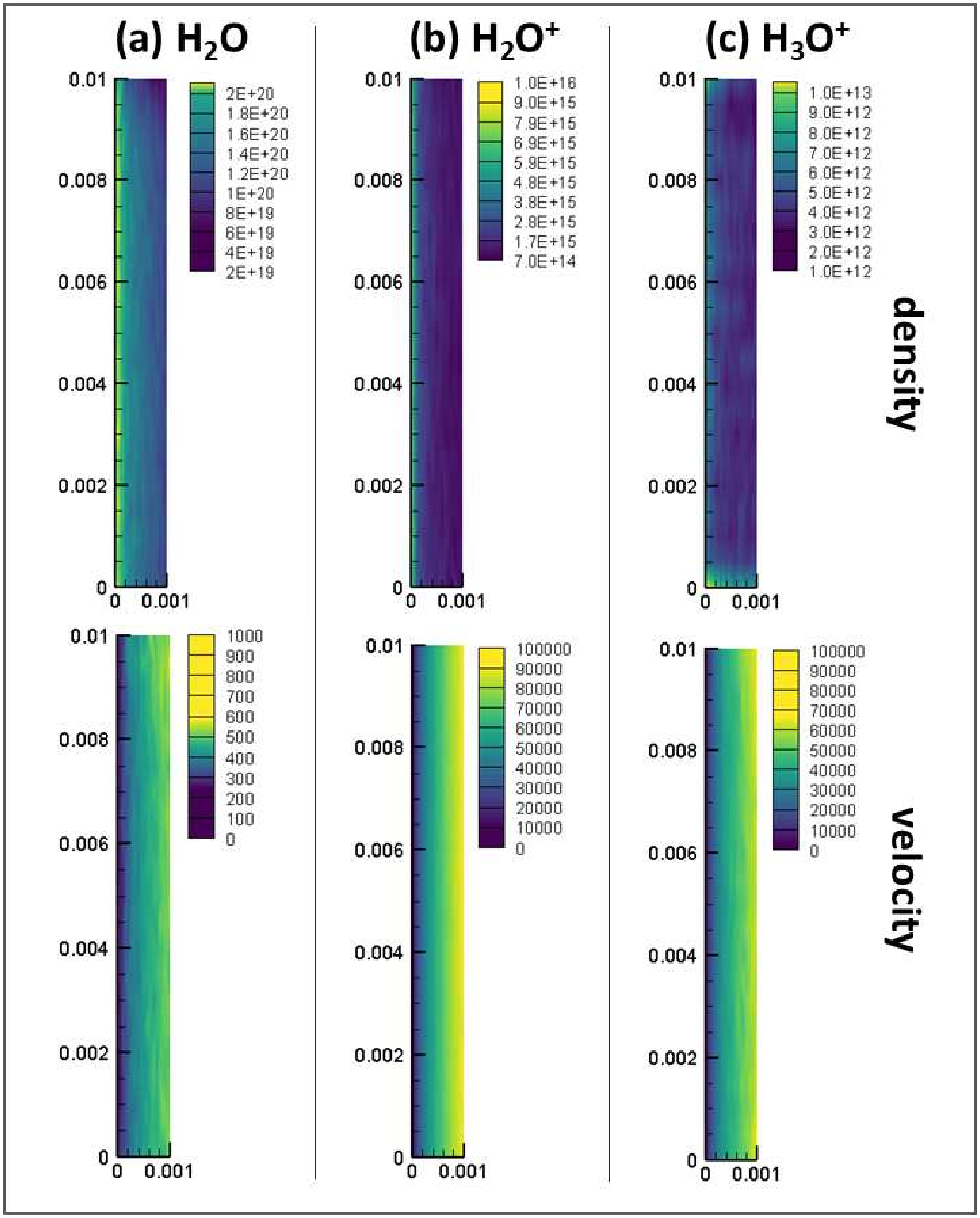

Figure 5.9: Results from PIC simulation of grid acceleration.

Table 5.5: Gridded Acceleration: Exit Plane Averages

Parameter	**Species**	*baseline*	*no collisions*	*high n_0*
average density, m^{-3}	H_2O	1.1×10^{20}	1.1×10^{20}	1.1×10^{22}
	H_2O^+	1.5×10^{15}	1.4×10^{15}	1.6×10^{15}
	H_3O^+	4.1×10^{12}	–	1.8×10^{14}
average velocity, m/s	H_2O	522	515	520
	H_2O^+	90,473	91,117	62,574
	H_3O^+	61,070	–	77,476
	all	524	515	520

Two other cases are simulated as points of comparison. First, the case above is re-run without charge and proton transfer collisions included. Next, collision are reintroduced and the neutral density is increased several orders of magnitude to $\mathbf{10}^{22}$ m^{-3}. The properties of the plume for each case are averaged across the exit plane and presented in Table 5.5. The velocity of each species is averaged across all N nodes at the exit plane according to:

$$\langle v \rangle = \frac{\sum_{i=1}^{N} n_i v_i}{\sum_{i=1}^{N} n_i} \tag{5.8}$$

Dividing the result of Eq. 5.8 by g gives the specific impulse of each species. Similarly, the combined specific impulse can be defined as:

$$\langle Isp \rangle = \frac{1}{g} \frac{\sum_{j=1}^{3} \sum_{i=1}^{N} n_{i,j} v_{i,j}}{\sum_{j=1}^{3} \sum_{i=1}^{N} n_{i,j}} \tag{5.9}$$

where j represents each of the ion and neutral species simulated.

This example indicates that charge and proton transfer between water ions and neutrals is not an important process in gridded acceleration. While some H_3O^+ ions are generated in the region, they are predicted to be two orders of magnitude lower than the H_2O^+ population. Thus the majority of the H_2O^+ ions pass through the acceleration region without colliding with a background neutral and the resulting exit velocity is largely unaffected. The specific impulse across all ions and neutrals forming the plume can be calculated by dividing the value in the bottom row of Table 5.5 by 9.8 m/s^2 to give **Isp ≈ 53 seconds** in all cases. The impact of the low ionization fraction and slow moving neutrals exiting the thruster is evident here. In all cases examined the specific impulse is driven by the neutral speed and is unacceptably low for an EP device. Note that even in the case that finite grid area is assumed to block some neutral transit while remaining transparent to ions due to electrostatic optics, the specific impulse will still be dominated by the neutral flux unless higher ionization fractions can be obtained. Thus in using water as a propellant in gridded ion thrusters, the important effects of plasma chemistry will occur in the upstream plasma generation region. Therefore it will be critical to better understand theoretically and demonstrate experimentally the plasma densities and ionization fractions that can be achieved in water-based discharges.

5.4.3 Ambipolar Acceleration

5.4.3.1 Ion-ion Reactions over Varying Length Scales

In these studies, the 5 eV electron temperature case is investigated for several different acceleration length scales. Per the analysis performed in Chap. 3, the accelerating potential is determined by the electron temperature as:

$$|\Delta\Phi_{sh}| = \frac{1}{2}eT_e\left(1 + ln\left(\frac{m_{H_2O}}{2\pi m_e}\right)\right) \tag{5.10}$$

Thus an accelerating potential drop of 21.4 V across the sheath region is imposed with another 2.5 V of acceleration coming from the Bohm acceleration into the pre-sheath. This accelerating potential is used for all cases. A range of length scales for the acceleration region has been found in helicon thrusters. On the small end, the acceleration could occur across a free-standing sheath that has a length scale on the order of a few Debye lengths. This situation would be analogous to the gridded acceleration case in that plasma chemistry does not have time to develop over the small length scales. However, other studies have measured potential drops over longer length scales, on the order of the device radius or greater [138,159,160]. Thus the first analysis looks only at the effect of charge exchange reactions on ion density and velocity evolution over a range of accelerating distances: **Case I: 1 mm, Case II: 1 cm, Case III: 5 cm**. Note that for Cases II & III, the difficulty of resolving the large axial distance is mitigated by reducing the radial dimension as the solutions from the previous cases showed minimal radial variation. To further reduce computation time for the 5 cm case, the initial drift velocity of neutrals into the domain is increased by a factor of 2, which is not expected to effect the collision rates or resulting densities. Case II (1 cm acceleration length) was run for both a 1 cm and 1 mm radial dimension to assess the effects of reducing the radial domain. A more detailed investigation of radial effects is presented in Appendix B.

In this first set of simulations, electron reactions such as ionization and dissociative recombination are not included. However, a background density of “Boltzmann” electrons that follows the potential distribution is introduced to allow for ambipolar acceleration. The density is updated spatially at each time step according to the *neutral-Boltzmann* scheme wherein Poisson's equation (Eq. 5.11) is numerically solved using a Newton-Raphson iterative approach.

$$\frac{\phi_{i-1,j} - 2\phi_{i,j} + \phi_{i+1,j}}{\Delta^2 x} + \frac{\phi_{i,j-1} - 2\phi_{i,j} + \phi_{i,j+1}}{\Delta^2 y} = -\frac{e}{\epsilon_0}\left[n_i - n_0 \exp\left(\frac{\phi - \phi_0}{kT_e}\right)\right] \tag{5.11}$$

The plume initial conditions are listed in Table 5.6. These conditions represent the properties of particles as they enter the domain at the left boundary. Simulation parameters are presented in Table B.1.

Table 5.6: Initial Conditions - Ambipolar Acceleration

	Parameter	**Value**	
Ions		H_2O^+	H_3O^+
	initial density	1×10^{16}	0
	initial drift velocity	5,159 m/s	–
	initial temperature	300 K	–
Neutrals		H_2O	
	initial density	1×10^{20}	
	initial drift velocity	*I,II:* 500 m/s	
	initial drift velocity	*III:* 1000 m/s	
	initial temperature	300 K	
Electrons		e^-	
	initial density	1×10^{16}	
	temperature (constant)	5 eV	

First, plots of (a) potential, (b) H_2O^+ density, and (c) H_2O^+ axial velocity (with streamlines), are shown in Fig. 5.10 for Case II (1 cm acceleration length × 1 cm radial extent). It is observed that the variations in H_2O^+ properties in this domain are again largely axial. A slight positive potential gradient and ion density gradient are observed just downstream of the entrance to the acceleration region.

Table 5.7: PIC Simulation Parameters - Ambipolar Acceleration

Parameter	*Case I: 1 mm*	*Case II: 1 cm*	*Case III: 5 cm*
potential @ z = 0		0 V *(all)*	
potential @ z = L		-21.4 V *(all)*	
domain size (r × L)	1 cm × 1 mm	1 mm × 1 cm *(1)* 1 cm × 1 cm *(2)*	1 mm × 5 cm
grid spacing (Δr,Δz)		5×10^{-5}, 5×10^{-5} m 5×10^{-5}, 2×10^{-4} m	*(I, II-1, III)* *(II-2)*
time-step (Δt)	2×10^{-9} s	2×10^{-9} s	3×10^{-9} s
particle weighting, H_2O	1×10^{11}	1×10^{11}	5×10^{10}
particle weighting, H_2O^+	1×10^{6}	1×10^{6}	1×10^{6}
particle weighting, H_3O^+	1×10^{4}	1×10^{5}	5×10^{5}

Variations in all values beyond this point are both gradual and minimal until near the exit plane where a relatively steep potential drop (and accompanying increase in ion speed) occurs.

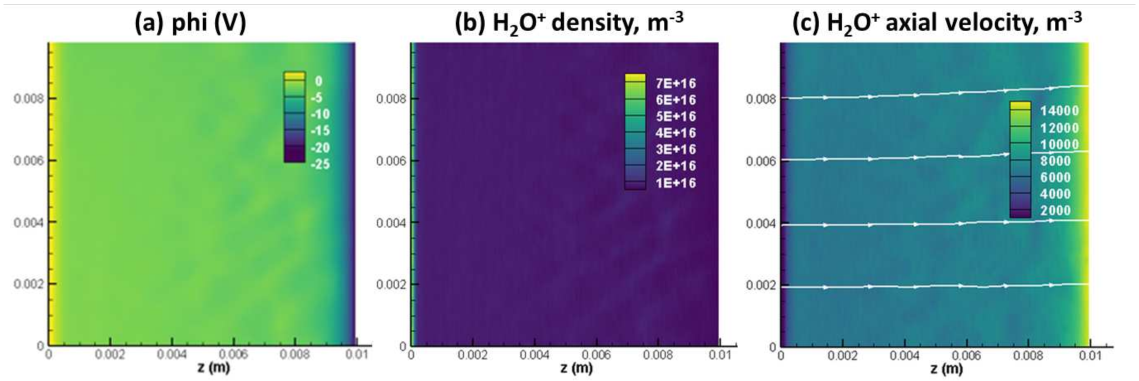

Figure 5.10: Results for 1 cm length ambipolar acceleration (Case II-A.2)

Next, for each simulation case, the densities and velocities of each species are averaged at the exit plane and summarized in Table 5.8. Values at the exit plane (z=L) are compared against entrance plane (z=0) conditions.

Table 5.8: Ambipolar Acceleration: Exit Plane Averages

Parameter	**Species**	*I: 1 mm*	*II: 1 cm*	*III: 5 cm*
density @ z = 0, m^{-3}	H_2O	2.2×10^{20}	1.7×10^{20}	1.3×10^{20}
	H_2O^+	8.1×10^{15}	1.1×10^{16}	9.7×10^{15}
density @ z = L, $\frac{n}{n_{H_2O}(x=0)}$	H_2O	3e-1	3e-2	3e-2
density @ z = L, $\frac{n}{n_{H_2O^+}(x=0)}$	H_2O^+	4e-1	2e-1	9e-2
	H_3O^+	2e-3	6e-4	3e-4
velocity @ z = 0, m/s	H_2O	221	277	757
velocity @ z = L, m/s	H_2O^+	15,420	15,758	16,107
	H_3O^+	13,883	13,248	14,314
	all	445	790	1068

Under all conditions, the percentage of H_3O^+ ions at the exit plane is small. The H_3O^+ ions which do reach the exit achieve a high velocity as most of the potential drop occurs near the exit plane. A more computationally efficient framework may allow for true 2D simulations wherein the radial domain can be extended and trajectories of slow ions can be captured more accurately.

To show the axial evolution of the plume, the potential, H_2O^+ density, and H_2O^+ axial velocity are averaged across the transverse direction and plotted as a function of the normalized axial distance in Fig. 5.11.

For longer acceleration length scales, a potential hump is observed just downstream of the inlet. This is due to space charge build-up in front of the entrance plane due to the slow charge exchange ions created there in the H_2O, H_2O^+ symmet-

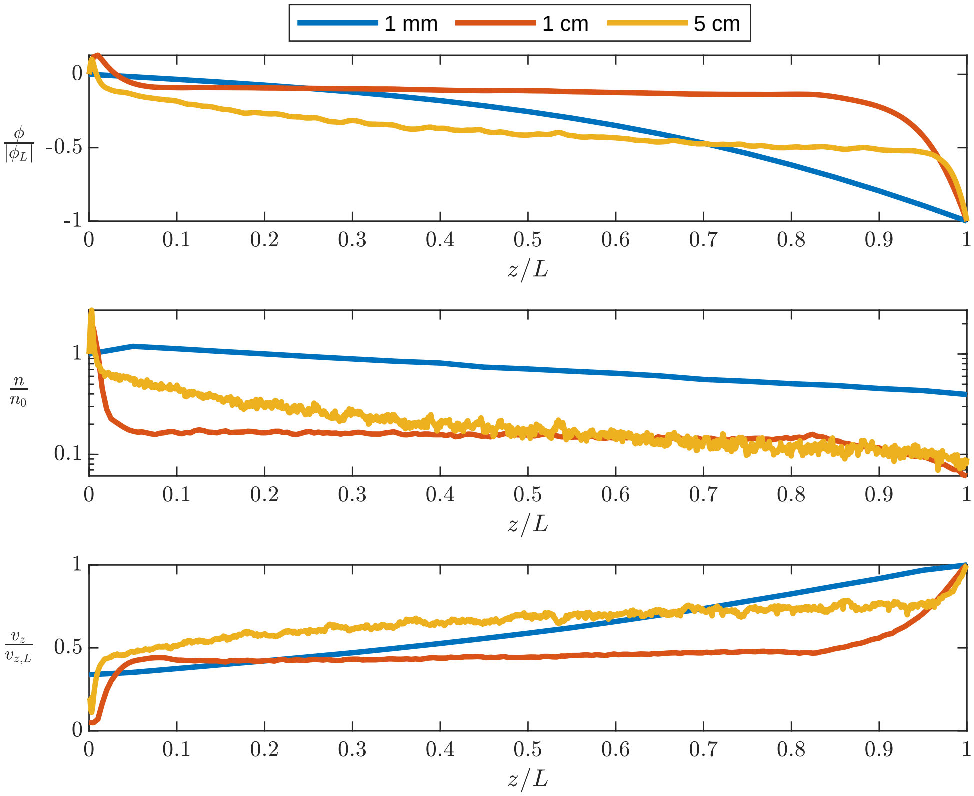

Figure 5.11: Normalized axial variation in plume properties

ric reaction (which has a cross-section ∼10X that of the proton transfer reaction). In these simulations, the local potential is not large enough to reflect the monoenergetic ion population entering from the bulk of the plasma. In reality, some spread in the energy of ions entering the plume region would be expected and those with lower energies would be reflected, thereby reducing the beam current. Thus even in cases where charge exchange reactions do not alter the beam composition significantly, they could lead to thrust and specific impulse reduction.

Based on these simulations, it is concluded that the proton transfer reaction does not significantly alter the exhaust beam composition during the ambipolar acceleration process for the primary ions in the beam at the length scales studied.

The main effect of charge exchange is likely to be in the reflection of low energy ions towards the spacecraft which could lead to surface charging and degradation. Effects may be more pronounced when integrated over a larger domain and for longer acceleration length scales. For reference, the potential drop in [159] occurs over a length scale greater than 10 cm. In cases such as this, care should be taken to ensure the neutral density profile follows an expected decay profile. Simulating large domains such as this would be a significant numerical undertaking and may be better approached with analytical methods.

5.4.3.2 Addition of Ion-Electron Reactions

Since electrons are assumed to be present in the ambipolar acceleration region, it is appropriate to also consider the effect that electron interactions can have on the evolution of the plume. The relevant interactions are those with the highest reaction rates based on their cross-sections and the densities of colliding species. At this point, only the following electron-neutral and electron-ion collisions are considered:

- ionization of H_2O: $e^- + H_2O \longrightarrow e + e + H_2O^+$
- dissociative recombination of H_2O^+: $e^- + H_2O^+ \longrightarrow$ (I) $e + (OH + H)$; (II) $e + (H_2 + O)$; (III) $e + (H + H + O)$
- dissociative recombination of H_3O^+: $e^- + H_3O^+ \longrightarrow$ (I) $e + (H_2O + H)$; (II) $e + (H_2 + OH)$

The only ion-ion collisions modeled are the proton and charge exchange collisions discussed in the previous section. Secondary collisions with neutral products other than H_2O are not considered. The electron density is again determined by the neutral-Boltzmann approach with initial conditions $n_e(\mathrm{z{=}0}) \approx n_i(\mathrm{z{=}0})$ and T_e **= 5 eV** for all cases. The reaction rates are calculated per cell according to the electron and ion densities within that cell and the velocity-dependent rate as:

$$\frac{\#\, collisions}{m^3 s} = n_1 n_2 \langle \sigma(v_{12}) v_{12} \rangle \tag{5.12}$$

Here n_1 is the fast species, which is the electron for all electron-neutral or electron-ion collisions. In ion-neutral collisions, n_1 is the H_2O^+ ion and $v_{12} \approx v_1$ as $v_n \ll v_i \ll v_e$. The collision cross-sections are energy dependent as described in the previous section and in [149]. In the case of adiabatic electrons as is assumed here, the collision rate coefficient $\langle \sigma(v_e) v_e \rangle$ is constant across the simulation domain for each process. Effects such as electron cooling in the plume and self-consistent evolution of the electron temperature may be considered in future work.

Simulation parameters are presented in Table 5.9. The addition of the electron reactions makes the problem more computationally challenging and thus the transverse extent of the domain is again reduced for numerical tractability. In these simulations, the H_2O^+ ions are tracked in two groups. The ions entering the domain at the left wall boundary represent one population. Ions created in ionization reactions ("iH_2O^+") represent a second group. Ions in each group have identical dynamics, undergo identical reactions, and interact electrostatically between groups. This construct provides additional insight into the contributions of each species to the plume evolution.

Table 5.9: PIC Simulation Parameters - Ambipolar Acceleration with Electron Reactions

Parameter		Value		
Ions		*H_2O^+*	*iH_2O^+*	*H_3O^+*
	initial density	$1{\times}10^{16}$	0	0
	initial drift velocity (H_2O^+)	5,159 m/s	–	–
	initial temperature (H_2O^+)	300 K	–	–
	particle weighting (H_2O^+)	$1{\times}10^{5}$	$1{\times}10^{3}$	$1{\times}10^{3}$
Neutrals		*H_2O*		
	initial density	$1{\times}10^{20}$		
	initial drift velocity	500 m/s		
	initial temperature	300 K		
	particle weighting	$1{\times}10^{8}$		
Domain		*acceleration grid region*		
	domain size (r x L)	0.5 mm × 1 cm		
	grid spacing (Δr,Δz)	$5{\times}10^{-5}$, $5{\times}10^{-5}$ m		
	potential @ z = 0	0 V		
	potential @ z = L	-21.4 V		
	time-step (Δt)	$2{\times}10^{-9}$ s		
	total time simulated	20 μs		

Plots of (a) potential, (b) H_2O^+ density, and (c) H_2O^+ axial velocity (with streamlines), are again shown in Fig. 5.12. Note that the axes are no longer to scale so the velocity streamlines in Fig. 5.12(c) are skewed substantially in the vertical dimension.

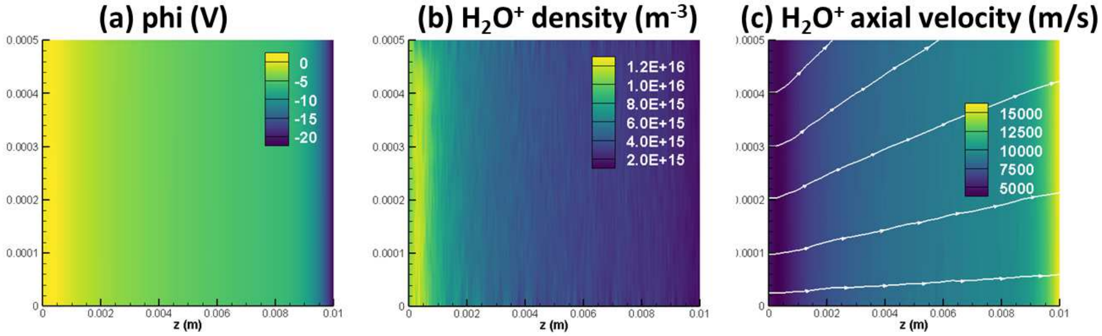

Figure 5.12: Results for 1 cm length ambipolar acceleration with charge exchange and electron interactions.

Fig. 5.13 shows the densities of H_2O^+ and H_3O^+ ions created in the plume due to ionization and proton exchange reactions, respectively. It can be seen that both populations of ions formed in the plume remain at least 2 orders of magnitude below the streaming ion population.

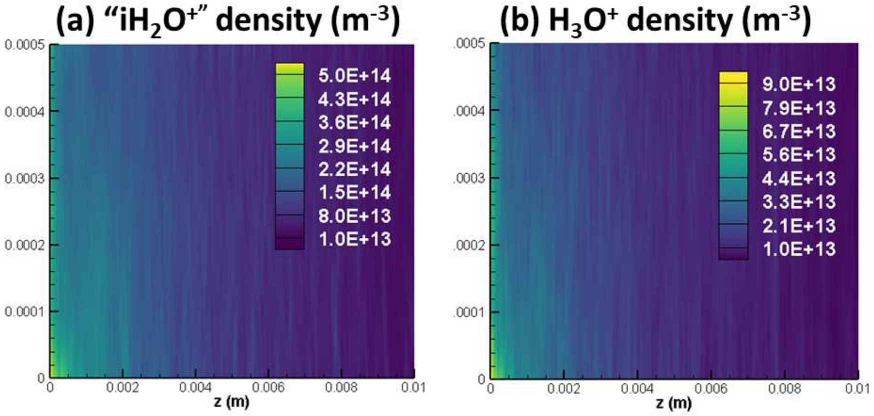

Figure 5.13: Densities of ions created in plume reactions.

Again, the densities and velocities of each species are averaged at the exit

Table 5.10: Ambipolar Acceleration with Electron Interactions: Exit Plane Averages

Parameter	**Species**	*ion reactions only*	*all reactions*
density @ z = 0, m^{-3}	H_2O	1.7×10^{20}	1.3×10^{19}
	H_2O^+	1.1×10^{16}	8.2×10^{15}
density @ z = L, $\frac{n}{n_{H_2O}(x=0)}$	H_2O	3e-2	2e-2
density @ z = L, $\frac{n}{n_{H_2O^+}(x=0)}$	H_2O^+	2e-1	2e-1
	iH_2O^+	–	3e-3
	H_3O^+	6e-4	3e-4
velocity @ z = 0, m/s	H_2O	277	323
velocity @ z = L, m/s	H_2O^+	15,758	15,687
	iH_2O^+	–	14,226
	H_3O^+	13,883	13,571
	all	790	835

plane and summarized in Table 5.10. Included again for reference are the results for the L = 1 cm case for ion (charge exchange and proton exchange) reactions only. Values at z=L are compared to entrance plane conditions in both cases.

Several observations are made with respect to the plume evolution when electron interactions are included. First, the density of ions created due to electron-neutral interactions in the plume is larger than that of H_3O^+ ions but still small in comparison to the injected ion population. Next, the addition of the recombination reaction which destroys both H_2O^+ and H_3O^+ ions does not appear to significantly affect the densities at the exit plane of either species. With electron reactions included, the exit velocity of the H_2O^+ ions is 97% of the maximal value of 16,296 m/s and thus reactions of both kind have little effect on plume evolution for these conditions.

5.4.3.3 Ambipolar Acceleration Conclusions

The effects of ion-ion and ion-electron reactions on ambipolar plume evolution are studied numerically. In both cases, collisions do not substantially alter the beam evolution for acceleration length scales ≤ 1 cm. The rate of dissociative recombination by electron impact with H_2O^+ is not high enough to significantly alter the acceleration efficiency in the case studied.

To further explore plume evolution will require a more detailed electron model that will allow better resolution of the electron density and temperature, taking into account the effects of expansion and energy transfer through these and other reactions. With such a model, the ambipolar potential drop should also be able to be modeled self-consistently. These effects could be captured with a fluid electron model solved in coordination with the particle simulations. It is possible that some of the processes currently being studied in Hall Thruster simulations, such as the rotating spoke ionization instability [161] may have analogous processes in an ambipolar thruster, which could be investigated either in the bulk of the discharge or near the exit plane. Detailed investigation of these processes would require fully-kinetic simulations with electrons treated as particles such as that of other low-temperature ionization wave phenomena [162].

5.5 Plasma Chemistry Conclusions

The analytical and numerical results obtained in this chapter have provided new insight into the importance of plasma chemistry in different regimes of the system. A 0D particle balance of the discharge regions indicates that dominant positive ion and achievable plasma density could vary widely based on electron temperature and reaction rates. As the discharge sets the upstream conditions for the plume, this is the most critical area for future study.

Next, the effects of plasma chemistry on plume evolution were explored for both gridded and ambipolar acceleration. The plume examples studied represent a set of discharge conditions that (1) were predicted numerically for a water plasma [146] and (2) would be most susceptible to chemistry effects in the plume due to the low ionization fraction. Even in this context, plasma chemistry is not found to be important in a gridded acceleration region. However it is observed in all cases that the unimpeded flow of neutral atoms out of the thruster would result in unacceptably low Isp values for an electric propulsion system.

The simulation of ambipolar acceleration both with and without electron reactions included reveals that H_3O^+ formation plays a negligible role in plume evolution. In contrast to the bulk discharge, the reaction rates for H_3O^+ formation (as shown previously in Fig. 5.2) are much lower for collisions in the plume due to the velocity dependence of the cross-section. It is likely here that effects of the symmetric charge exchange reaction (creating slow H_2O^+ ions) are more important due to its larger cross-section.

It is concluded that the efficiency impact of neutrals leaving the thruster unimpeded at slow velocities has a much bigger penalty on efficiency than their reactions with ions in the plume. Thus the priority for future investigation should be numerical and experimental studies of the achievable ionization fractions in a water discharge. The particle balance analysis predicts high ionization fractions are achievable for $T_e \sim 5$ eV and thus the extent to which this regime can be realized should be further investigated. In coordination with this effort, design changes to better confine neutral particles to the ionization region should be investigated numerically and experimentally.

Chapter 6: Conclusions and Future Work

6.1 Conclusions

6.1.1 Single-Stage Analysis Contributions

The suitability of water vapor as a propellant in electrodeless RF thrusters has been investigated from an analytical and numerical perspective, with model assumptions constrained by relevant theoretical and experimental results. Major conclusions from the literature affecting the efficiency model include (1) the ability to neglect negative ions except as an ionization energy loss pathway, (2) the behavior of the discharge as electropositive, dominated by H_2O^+ ions, and (3) the approximation of wall sheaths and magnetic nozzle potentials as 1D single-species Debye sheaths. Ionization costs for Maxwellian electrons are calculated and compared to argon, with curve fits provided for follow-on analyses. Though the ionization cost for water far exceeds argon at low temperature, it becomes comparable around 5 eV. As a result, the efficiency of a water propelled electrodeless thruster also becomes comparable above 5 eV. Thrust efficiency increases with both electron temperature and upstream mirror ratio, with diminishing gains achieved above a factor of 20 for the latter. Thus, per a zero-D analysis, water vapor appears to be a suitable propellant if a Maxwellian electron temperature above 5 eV can be sustained. As the physics of the the RF wave propagation is omitted, these results are relevant to any electrodeless configuration with Maxwellian electrons provided that radial wall losses can be mitigated.

6.1.2 Ion Cyclotron Heating Analysis Contributions

The gains in efficiency that can be attained with the addition of an ion cyclotron heating stage were assessed in 3 steps. First, the zero-D model developed for the single-stage thruster was extended to account for energy deposition and losses in a second stage. Next, this model was then used to evaluate a wide design space that included a range of device dimensions, magnetic field strengths, and heating energies. The design space that could provide improvements over a single-stage device was captured. Finally, particle studies of the ion trajectory in the presence of ion cyclotron heating provided a tool to investigate parameters such as antenna sizing and phase matching. These particle studies motivated further exploration of ion-ion reactions which were presented in Chapter 5. This work represents the first evaluation of ion cyclotron heating for a water-propelled plasma thruster and provides key insight into its regimes of applicability and limitations for small-scale devices.

6.1.3 Water Plasma Chemistry Contributions

This analysis represents the first detailed study on the effects of charge exchange and H_3O^+ formation for a water-propelled plasma thruster. The effects of water plasma chemistry are analyzed both in the context of plasma composition in the discharge region and in the context of plume evolution. It is found that wide ranges of ionization fractions and various ion species fractions are possible depending on the electron temperature. Lower electron temperatures favor higher proportions of H_3O^+ but lower overall ionization fractions. Electron temperatures around 5 eV result in H_2O^+ being the dominant ion and allow for high ionization fractions ($n_i/n_n \gtrsim 1$). These results further point the thruster design towards achieving electron temperatures in the range of 5 eV.

The study of chemistry effects in the plume evolution reveals that ions forming the plume are largely unaffected by reactions in this region. Effects can be neglected outright for fast gridded acceleration and can also be largely neglected for the ambipolar cases considered. It is noted that for the longest acceleration length analyzed (5 cm) a 10% reduction in ion Isp is observed. Longer length scales are difficult to capture with the Starfish PIC code in its current version but could be further explored in future work.

The results from both regimes indicate that the highest priority for future study should be better numerical and experimental predictions of the discharge conditions. High ionization fractions are shown to be critical for overall efficiency, otherwise the specific impulse of the system is dominated by the loss of slow neutrals. If high ionization fractions can be attained, it can be expected that plasma chemistry in the plume will not dramatically alter overall efficiency. Further simulations of high density plumes should follow the detailed discharge chemistry investigations.

6.2 Suggested Topics for Extension of this Work

6.2.1 Analytical Thrust Efficiency Modeling

Future work in the extension of analytical models of an electrodeless water vapor thruster should include an electron power balance analysis to self-consistently determine the electron temperature as a function of power deposited into the discharge. Other approximations, such as radially uniform plasma or zero radial losses in the ionization stage, could also be relaxed.

6.2.2 ICH Parameter Space Analysis

Future work in defining the practical design space for ion cyclotron heating could include creating a curve to specify feasible ICH magnetic field strengths as a function of thruster diameter (e.g. as shown in Fig. 6.1). Feasibility could be defined with mass and/or volume as the figure of merit. For example, at a given thruster diameter, one could calculate the thrust force and the *thrust-to-weight* ratio based on a model for magnet system mass as a function of magnetic field strength. Then the figures of merit could be compared with the *thrust-to-weight* or *mass-to-power* ratios of other state-of-the-art EP systems and determine a reasonable range. For example for ion engines: m/P $\approx$ 5-10 kg/kW, T/$m_{thruster}$ $\approx$ 5-10 mN/kg.

6.2.3 ICH Particle Studies

The particle-based modeling techniques to study ion cyclotron heating in Chap. 4 could be extended in several ways. Future work could include expansion to particles at all starting radial locations. The results could be generalized to a

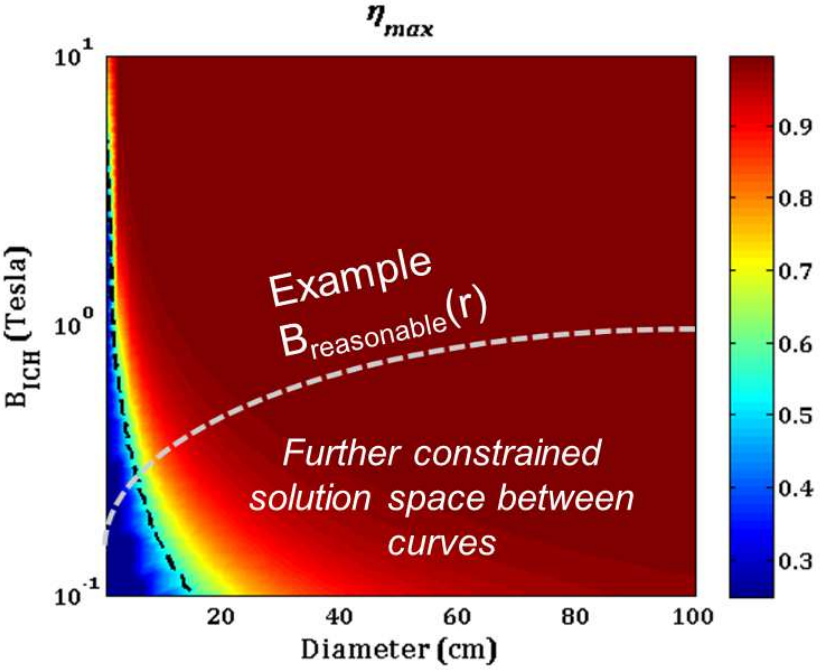

Figure 6.1: Efficiency contour for ICH design space with hypothetical magnetic field strength constraints.

thruster configuration by incorporating common radial density distributions for electrodeless thrusters. Beyond these efforts, the simulation could be integrated with a particle-in-cell framework for self-consistently calculating electromagnetic field penetration into the plasma and the effects of particle-particle interactions on heating. Such an effort would be a significant numerical undertaking but commercial tools, such as TechX's USIM or VSIM codes, may be applicable depending on the densities of interest.

6.2.4 Plasma Composition

The results presented in Section 5.3 showed that a reduced-order chemistry model is useful for predicting the dominant ion species and allowable plasma densities for a range of discharge conditions. This analysis could be extended by coupling a calculation of the electron temperature (and/or distribution function) to the neutral density. Such an effort would move the model closer to dependence on variables that represent real "knobs" that can be turned in the configuration of a physical system. While electron temperature is a useful variable, as it is easily and often measured, it is still a variable that ultimately depends on other physical settings such as the RF power, neutral density and flow rate, and wave heating properties. Additionally, it was observed that the choice of reference for particular cross-sections strongly affects the predicted composition. Thus it would be useful to set "error bars" on each cross-section based on the range of values available in the literature and propagate that uncertainty through to quantify the range of possible predicted compositions for various electron temperatures. Finally, comparison against experimental measurements of the plasma composition under various conditions would be extremely valuable. To our knowledge, there has been no clear experimental characterization of the exact ions present in low pressure water discharges to date.

6.2.5 Simulation Extension

Future development of PIC simulations could be extended to use collisional modeling in the discharge region to predict the plasma composition. This could be done most accurately with a fully kinetic approach (electrons as particles) but would be quite computationally expensive and thus would require parallelization and potentially GPU implementation. Implicit PIC methods may also be useful for this purpose, such as in [163]. Even a fluid electron implementation as simple as the neutral-Boltzmann approach would be useful for comparing against the results predicted in Chapter 5.3.

PIC simulations of the acceleration region could be extended in several ways. The simulations presented in this thesis assumed radially uniform ion and neutral densities. However, RF discharges often generate non-uniform plasma densities and the effects of these non-uniformities could be explored.

Appendix A: State of the Art Performance Data

All of the performance data collected for the systems listed in Chapter 2 are provided in the tables that follow. The corresponding references are included again for convenience. If a system's power range is specified, it is given in the third column, followed by the particular powers for which data is obtained in the fourth column. For thrust efficiency, if a value is reported in the reference, that value is used in calculations and plots for this survey. If only thrust, specific impulse, and input power are given, thrust efficiency is calculated as outlined in Chapter 2. In this table, both reported and calculated thrust efficiencies are shown. It is believed that any discrepancies in the two values stem largely from whether the authors report the power into the thruster or into the PPU. PPU efficiencies are typically greater than 90%. For the purposes of performance comparison and trending, these differences are not of concern.

Table A.1: Performance data for ion engines

Thruster Name	Model	Power Range, kW	Input Power, kW	Thrust, mN	Specific Impulse, sec	η reported	η calculated
BRFIT	3	0.08	0.08	1.6	2800	0.27	0.27
	7	0.15-0.40	0.40	11	3850	0.53	0.52
ESA	XX		8.2[*]	240	5400	0.79	0.78
IES	--	0.4 –0.9	0.54	20.9	2402	0.46	0.45
			0.61	23.2	2665	0.50	0.50
Ion Engine (R&D)	25 cm		2	80	2080	0.6	0.6
IT	50	0.05 –0.14	0.05	2	2300	0.45	0.45
			0.14	5	3500	0.61	0.61
	100	0.15 –0.50	0.15	7	1900	0.43	0.43
			0.50	18	3300	0.58	0.58
Mu	10	0.29 –0.35	0.35	8	3200	0.36	0.36
NEXT	--	0.6 –13	0.63	25.6	1410	0.30	0.28
			7.2	236	4000	0.67	0.64
NSTAR	--	0.5 –2.3	0.5	19	1900	0.36	0.35
			2.3	92	3100	0.62	0.61
RIT	10		0.46	15	3560	0.57	0.57
	22		4.5	150	4400	0.72	0.72
	35		3.0	104	4023	0.55	0.69
T	5		0.48	18	3200	0.55	0.59
	6	2.5 –4.5	2.5	75	3710	0.55	0.55
			4.5	145	4120	0.64	0.65
XIPS	8 cm	0.1 –0.35	0.1	2	2000	0.2	0.2
			0.35	14	3000	0.53	0.59
	13 cm		0.45	18	2350	0.49	0.46
	25 cm	2.3 –4.5	2.3	79	3400	0.65	0.57
			4.5	165	3500	0.63	0.63

[*]

Table A.2: Performance data for Hall thrusters

Thruster Name	Model	Power Range, kW	Input Power, kW	Thrust, mN	Specific Impulse, sec	η reported	η calculated
BHT	200[*]	0.1 –0.4	0.13	8	1390	0.40	0.41
			0.2	13	1394	0.44	0.44
			0.4	19.4	1900	0.50	0.45
	600	0.3 –0.8	0.6	39	1585	0.50	0.50
BPT	2000		2.2	123	1700	0.48	0.47
	4000	1.1 –4.5	1.1	80	1200	0.45	0.43
			4.9	250	2100	0.55	0.53
CHT	28 mm 40 mm 50 mm	0.1 –0.4	0.3	11	1800	0.32	0.32
CHT	2.6 cm	0.09 –0.19	0.09	3	1100	0.20	0.18
			0.19	6	1650	0.27	0.26
	9 cm		1	--	--	0.4	--
HiVHAc	--	0.32 –3.7	0.32	21.3	981	0.32	0.32
			3.52	197.5	2144	0.59	0.59
			3.66	157	2655	0.56	0.56
HEMPT	--	1.38 –1.5	1.5	90	2800	0.49	0.46
HT	100D	0.12 –0.4	0.12	6	800	0.2	0.2
			0.4	18	1600	0.35	0.35
	400	0.4 –0.8	0.4	19	1000	0.23	0.23
			0.8	25	1450	0.22	0.22
PlaS	40	0.1 –0.65	0.23	17	1010	0.37	0.37
PPS	1350-G		1.5	89	1650	0.50	0.52
ROS	200		2	132	1765	0.52	0.57
SPT	1	0.6 –3.2	0.6	39.9	1424	0.39	0.46
			3.1	144.5	2533	0.55	0.58
	50		0.35	20	1010	0.35	0.31
	70		0.7	40	1500	0.45	0.42
	100		1.35	80	1600	0.5	0.46
	140		5	300	1750	0.55	0.51
T	40	0.1 –0.4	0.1	5	1000	0.25	0.25
			0.4	20	1600	0.39	0.39
	140	2 –4	3.4	197	2000	0.57	0.57
TCHT	3B	0.08 –0.17	0.08	--	--	0.26	--
			0.17			0.39	

[*]

[*]

Table A.3: Performance data for helicon thrusters

Thruster Name	Research Group or University	Power Range, kW	Input Power, kW	Thrust, mN	Specific Impulse, sec	η reported	η calculated
HEAT	Japanese Collaboration	1.8 –2.3	2	11	840	0.02	0.02
			--	2.5	290	0.001	--
			--	0.9	390	0.0008	--
HDLT	ANU, Surrey Space Center	0.25 –0.65	0.25	1	--	--	--
			0.65	2.8	280	--	0.01
HPH.com	EU Collaboration	0.05 –0.1	0.008	0.5	422	0.13	0.13
			0.05	--	--	0.19	--
mHT	MIT	0.5–1.1	0.7	10	--	--	--
			1.1	20	--	--	--
PM-HPT	Tohoku Univ. & ANU		2	15	1960	0.075	0.072
VASIMR (VX-10)[*]	Ad Astra		3	--	--	0.02	--
			6.5	--	--	0.01	
Lab model	Georgia Tech	0.21 –0.84	0.84	6.3	140	--	0.01

---

[*]

Table A.4: Predicted performance data for helicon thrusters

Author(s)	Input Power, kW	Thrust, mN	Specific Impulse, sec	η predicted
Fruchtman	3.95	72	2300	0.2
Vitucci & Sedwick	1.8	--	--	0.27
	0.92	--	--	0.55
Ahedo	0.7	--	--	0.27

Appendix B: Numerical Experiments with Radial Confinement

For Cases II & III in Section 5.4.3 which have a large axial dimension and small radial dimension, the boundary condition at the top edge of the domain was experimented with. Previously, a symmetry boundary condition was applied to the bottom edge of the domain and the top edge had a Neumann boundary condition, allowing the plasma to expand into space. When the radial dimension is reduced in the longer axial cases, particles escape the domain quickly with a Neumann boundary condition at the top edge. Applying a symmetry boundary condition at the top edge instead approximates a 1D solution. In this case, particles cannot leave the domain along radial boundaries. However, confining the plasma in this way is not a physically realistic representation of the plume as radial expansion and trajectories are important. Thus all simulations are run for both sets of boundary conditions and results are compared. The results represent two limits: one where particles quickly leave the domain and the other where a maximal number of collisions are encountered. First, results are presented for two radial domain sizes (II-A.1: 1 mm, II-A.2: 1 cm) with with symmetry at the bottom edge only for both and for the 1 mm radial case (II-B) with top and bottom edge symmetry. The results are compared Simulation parameters for all simulation cases are included in Table B.1.

For each simulation case, the densities and velocities of each species are av-

Table B.1: PIC Simulation Parameters - Ambipolar Acceleration

Parameter	*Case I: 1 mm*	*Case II: 1 cm*	*Case III: 5 cm*
potential @ z = 0		0 V *(all)*	
potential @ z = L		-21.4 V *(all)*	
domain size (r × L)	1 cm × 1 mm	1 mm × 1 cm *(A.1,B)* 1 cm × 1 cm *(A.2)*	1 mm × 5 cm
grid spacing (Δr,Δz)		$5{\times}10^{-5}$, $5{\times}10^{-5}$ m $5{\times}10^{-5}$, $2{\times}10^{-4}$ m	*(I, II-A.1,B, III)* *(II-A.2)*
time-step (Δt)	$2{\times}10^{-9}$ s	$2{\times}10^{-9}$ s	$3{\times}10^{-9}$ s
particle weighting, H_2O	$1{\times}10^{11}$	$1{\times}10^{11}$ *(A.1,A.2)* $1{\times}10^{10}$ *(B)*	$5{\times}10^{10}$
particle weighting, H_2O^+	$1{\times}10^{6}$	$1{\times}10^{6}$	$1{\times}10^{6}$
particle weighting, H_3O^+	$1{\times}10^{4}$	$1{\times}10^{5}$ *(A.1,A.2)* $5{\times}10^{4}$ *(B)*	$5{\times}10^{5}$

eraged at the exit plane and summarized in Tables B.2 and B.3 for each set of boundary conditions. Values at the exit plane (z=L) are compared against entrance plane (z=0) conditions.

The results for the 1 mm case are almost identical between the two sets of boundary conditions as radial expansion does not play an important role in this small axial domain. However for the 1 cm and 5 cm cases shown in Table B.2, the exit plane values are biased to higher axial velocity particles and lower densities of H_3O^+ particles due to radial losses. The results presented in Table B.3 exhibit different trends. In this case, as the acceleration length increases, the fraction of H_2O^+ at the exit plane decreases while the fraction of H_3O^+ increases. This accounts

Table B.2: Ambipolar Acceleration: Exit Plane Averages (all acceleration lengths, Neumann B.C. at top edge)

Parameter	**Species**	*I: 1 mm*	*II-B: 1 cm*	*III: 5 cm*
density @ z = 0, m^{-3}	H_2O	2.2×10^{20}	1.7×10^{20}	1.3×10^{20}
	H_2O^+	8.1×10^{15}	1.1×10^{16}	9.7×10^{15}
density @ z = L, $\frac{n}{n_{H_2O}(x=0)}$	H_2O	3e-1	3e-2	3e-2
density @ z = L, $\frac{n}{n_{H_2O^+}(x=0)}$	H_2O^+	4e-1	2e-1	9e-2
	H_3O^+	2e-3	6e-4	3e-4
velocity @ z = 0, m/s	H_2O	221	277	757
velocity @ z = L, m/s	H_2O^+	15,420	15,758	16,107
	H_3O^+	13,883	13,248	14,314
	all	445	790	1068

Table B.3: Ambipolar Acceleration: Exit Plane Averages (all acceleration lengths, symmetry B.C. at top edge)

Parameter	**Species**	*I: 1 mm*	*II-B: 1 cm*	*III: 5 cm*
density @ z = 0, m^{-3}	H_2O	2.2×10^{20}	2.3×10^{20}	1.5×10^{20}
	H_2O^+	8.1×10^{15}	1.2×10^{16}	1.4×10^{16}
density @ z = L, $\frac{n}{n_{H_2O}(x=0)}$	H_2O	5e-1	2e-1	7e-1
density @ z = L, $\frac{n}{n_{H_2O^+}(x=0)}$	H_2O^+	4e-1	2e-1	7e-2
	H_3O^+	2e-3	9e-3	7e-2
velocity @ z = 0, m/s	H_2O	226	198	650
velocity @ z = L, m/s	H_2O^+	15,436	15,559	15,123
	H_3O^+	10905	13,955	14,314
	all	424	731	912

for over an order of magnitude difference in the predicted exit plane density of H_3O^+ for the 1 cm length results in Tables B.2 and B.3.

When particles are confined radially (Table B.3), they will experience more collisions before leaving the domain at the exit plane, with the number of collisions being proportional to the axial length. For example, there are 200 H_2O^+ ions for every H_3O^+ ion at the exit plane in the 1 mm case. In the 5 cm case, the numbers of H_2O^+ and H_3O^+ ions at the exit plane are equal. However the results shown in Table B.3 predict significantly higher secondary ion populations at the exit plane than would be found when 2D expansion is allowed and thus represent an upper limit. These results are included here to illustrate that with confinement, secondary ion populations can reach non-negligible populations. However, the boundary conditions here do not accurately represent the plume conditions and thus are only included as a point of comparison.

Beyond 1 cm, a non-negligible fraction of primary ions may undergo charge and proton exchange reactions if they are confined radially. When confined in this geometry, the H_3O^+ and charge exchange H_2O^+ ions gain a large axial velocity as the potential profile is relatively flat upstream of the exit plane. More comprehensive 2D modeling will be required to determine if radial losses of these ions would lead to substantial beam spreading or depletion of primary ions.

Appendix C: PIC Simulation Input Files

5 input files are created for each simulation:

- *"starfish.xml"* - master file (contains source and time-stepping info)
- *"domain.xml"* - defines grid for simulation domain and boundary conditions
- *"boundaries.xml"* - defines additional boundaries (e.g. virtual boundary for injection of particles)
- *"materials.xml"* - defines all particles (including weighting) and solid materials used in simulation domain
- *"interactions.xml"* - defines all possible reactions between items defined in *"materials.xml"*

An example is provided for each simulation type (gridded and ambipolar).

Gridded Acceleration Input Files

"starfish.xml"

```
<!--
<simulation>
```

```
<note>Gridded Acceleration Region - 1cmx1mm tube</note>

<!-- load input files -->
<load>domain.xml</load>
<load>materials.xml</load>
<load>boundaries.xml</load>
<load>interactions.xml</load>

<output type="boundaries" file_name="results/boundaries.vtp" format="vtk">
<variables>flux-normal.H2O+, deprate</variables>
</output>
<!-- set potential solver -->
<!--<solver type="constant-ef">
<comps>0,0</comps>
</solver>
-->

<solver type="poisson">
<n0>1</n0>
<Te0>5</Te0>
<phi0>0</phi0>
<max_it>1e4</max_it>
<nl_max_it>25</nl_max_it>
<tol>1e-3</tol>
<nl_tol>1e-2</nl_tol>
<linear>true</linear> <!-- gets rid of electrons for grid acceleration-->
<initial_only>false</initial_only>
</solver>

<!-- set sources
-->
<sources>


<boundary_source name="space">
<type>maxwellian</type>
<material>H2O</material>
<boundary>inlet</boundary>
<mdot>2e-5</mdot>
<temperature>300</temperature>
<v_drift>500</v_drift>
</boundary_source>

<boundary_source name="space">
<type>maxwellian</type>
```

```
<material>H2O+</material>
<boundary>inlet</boundary>
<mdot>3e-8</mdot>
<temperature>300</temperature>
<v_drift>5000</v_drift>
</boundary_source>

</sources>
<!-- -->

<!-- set time parameters -->
<time>
<num_it>10000</num_it>
<dt>5e-10</dt>
</time>

<!-- save animation -->
<animation start_it="1" frequency="50">
<output type="2D" file_name="field_ani.dat" format="tecplot"
variables="phi,nd.H2O,nd.H2O+,nd.H3O+,u.H2O+,v.H2O+,u.H3O+,
v.H3O+,u.H2O,v.H2O" />
</animation>

<!-- run simulation -->
<starfish />

<!-- save results -->
<output type="2D" file_name="field.dat" format="tecplot">
<variables>phi, nd.e-, nd.H2O+, nd.H2O, nd.H3O+, t.e-, t.H2O+,
t.H3O+, t.H2O, u.H2O+, v.H2O+, u.H3O+, v.H3O+, u.H2O, v.H2O,
u.HO, v.HO</variables>
</output>

<output type="boundaries" file_name="boundaries.dat" format="tecplot">
<variables>flux.H2O+, flux-normal.H2O+, deprate</variables>
</output>


</simulation>
```

“domain.xml”

```
<domain type="xy">
```

```
<mesh type="uniform" name="mesh">
<origin>0,0</origin>
<spacing>5e-5, 5e-4</spacing>
<nodes>21,21</nodes> <!-- 1 mm x 1 cm-->
<mesh-bc wall="left" type="dirichlet" value="0" />
<mesh-bc wall="right" type="dirichlet" value="-800" />
<mesh-bc wall="bottom" type="symmetry"/>
</mesh>
</domain>
```

"boundaries.xml"

```
<boundaries>

<boundary name="inlet" type="virtual" >
<path>M 0, 0.01 L 0, 0</path>
</boundary>

</boundaries>
```

"materials.xml"

```
<!-- materials file -->
<materials>

<material name="H2O" type="kinetic">
<molwt>18</molwt>
<charge>0</charge>
<spwt>1e10</spwt>
<particle_merge_skip>25</particle_merge_skip>
<vel_grid_dims>20,20,5</vel_grid_dims>
</material>

<material name="HO" type="kinetic">
<molwt>17</molwt>
<charge>0</charge>
<spwt>1e10</spwt>
```

```
</material>

<material name="H3O+" type="kinetic">
<molwt>19</molwt>
<charge>1</charge>
<spwt>1e3</spwt>
</material>

<material name="H2O+" type="kinetic">
<molwt>18</molwt>
<charge>1</charge>
<spwt>1e6</spwt>
<particle_merge_skip>25</particle_merge_skip>
<vel_grid_dims>20,20,5</vel_grid_dims>
<init>nd_back=1e4</init>
</material>

</materials>
```

“interactions.xml”

```
<!-- material interactions file -->
<material_interactions>

<!--Lishawa, 1990 Table 5-->
<chemistry>
<sources>H2O+,H2O</sources>
<products>HO,H3O+</products>
<rate type="table" is_sigma="true">
<table_values>
[1,2.9e-19], [1.5, 2.89E-19], [2, 1.86E-19],
[2.5, 8.51E-20], [5, 6.38E-20],
[6, 4E-20], [10, 3.13E-20], [15, 2e-20],
[20, 1.5e-20], [27, 0.5E-20]
</table_values>
<dep_var>T.H2O+</dep_var>
<input_wrappers>energy,JtoEv</input_wrappers>
</rate>
</chemistry>

<!--Lishawa, 1990 Table 7-->
<mcc model="cex" name="cex">
```

```
<source>H2O+</source>
<target>H2O</target>
<sigma>table</sigma>
<sigma_tabulated>
[0.5769, 4.2396E-19], [1.0897, 2.2325E-19],
[1.2821, 1.5821E-19], [1.6026, 1.2907E-19],
[2.6923, 9.55E-20], [6.859, 8.231E-20],
[12.1795, 8.265E-20], [19.2949, 6.628E-20],
[25.0641, 6.665E-20], [30.3205, 5.353E-20]
</sigma_tabulated>
<sigma_dep_var>energy</sigma_dep_var>
<max_target_temp>10000</max_target_temp>
<frequency>1</frequency>
</mcc>
```

Ambipolar Acceleration Input Files

"starfish.xml"

```
<!--
<simulation>
<note>Ambipolar Acceleration Region - 1cmx0.5mm tube</note>

<!-- load input files -->
<load>domain.xml</load>
<load>materials.xml</load>
<load>boundaries.xml</load>
<load>interactions.xml</load>

<output type="boundaries" file_name="results/boundaries.vtp"
format="vtk">
<variables>flux-normal.H2O+, deprate</variables>
</output>
<!-- set potential solver -->
<!--<solver type="constant-ef">
<comps>0,0</comps>
</solver>
-->
```

```
<solver type="poisson">
<n0>1</n0>
<Te0>5</Te0>
<phi0>0</phi0>
<max_it>1e4</max_it>
<nl_max_it>25</nl_max_it>
<tol>1e-3</tol>
<nl_tol>1e-2</nl_tol>
<linear>true</linear>
<initial_only>false</initial_only>
</solver>

<!-- set sources
-->
<sources>

</sources>
<boundary_source name="inlet">
<type>maxwellian</type>
<material>H2O</material>
<boundary>inlet</boundary>
<mdot>7.5e-7</mdot>
<temperature>300</temperature>
<v_drift>500</v_drift>
</boundary_source>

<boundary_source name="inlet">
<type>maxwellian</type>
<material>H2O+</material>
<boundary>inlet</boundary>
<mdot>7.8e-10</mdot>
<temperature>300</temperature>
<v_drift>5158</v_drift>
</boundary_source>

</sources>

<!-- set time parameters -->
<time>
<num_it>10000</num_it>
<dt>2e-9</dt>
</time>

<!-- save animation -->
```

```
<animation start_it="1" frequency="100">
<output type="2D" file_name="field_ani.dat" format="tecplot"
variables="phi,nd.e-,nd.H2O,nd.H2O+,nd.iH2O+,nd.H3O+,u.H2O+,
v.H2O+,u.iH2O+,v.iH2O+,u.H3O+,v.H3O+,u.H2O,v.H2O,
mpc.H2O,mpc.H2O+,mpc.iH2O+,mpc.H3O+" />
</animation>

<solver>
<type>poisson</type>
<!--<method>direct1d</method>-->
<n0>1e16</n0>
<Te0>5</Te0>
<phi0>0</phi0>
<max_it>1e4</max_it>
<nl_max_it>25</nl_max_it>
<tol>1e-3</tol>
<nl_tol>1e-2</nl_tol>
<linear>false</linear>
<initial_only>false</initial_only>
</solver>

<!-- run simulation -->
<starfish randomize="false" />

<!-- output -->
<!-- save results -->
<output type="2D" file_name="field.dat" format="tecplot">
<variables>phi, nd.e-, nd.H2O+, nd.iH2O+, nd.H2O, nd.H3O+, t.e-,
t.H2O+, t.H3O+, t.H2O, u.H2O+, v.H2O+, u.iH2O+, v.iH2O+, u.H3O+,
v.H3O+, u.H2O, v.H2O, u.HO, v.HO</variables>
</output>

<output type="boundaries" file_name="boundaries.dat" format="tecplot">
<variables>flux.H2O+, flux-normal.H2O+, deprate</variables>
</output>


</simulation>
```

"domain.xml"

```
<domain type="xy">
```

```
<mesh type="uniform" name="mesh">
<origin>0,0</origin>
<spacing>5e-5, 5e-5</spacing>
<nodes>201,11</nodes> <!-- 1 cm x 0.5 mm-->
<mesh-bc wall="left" type="dirichlet" value="0" />
<mesh-bc wall="right" type="dirichlet" value="-21.4" />
<mesh-bc wall="bottom" type="symmetry"/>
<!--<mesh-bc wall="top" type="symmetry"/>-->
</mesh>

</domain>
```

"boundaries.xml"

```
<boundaries>

<boundary name="inlet" type="virtual" >
<path>M 0, 0.0005 L 0, 0</path>
</boundary>

</boundaries>
```

"materials.xml"

```
<!-- materials file -->
<materials>

<materials>


<material name="e-" type="boltzmann_electrons">
<phi0>0</phi0>
<kTe0>5</kTe0>
<den0>1e16</den0>
</material>
```

```
<material name="H2O" type="kinetic">
<molwt>18</molwt>
<charge>0</charge>
<spwt>1e8</spwt>
<particle_merge_skip>25</particle_merge_skip>
<vel_grid_dims>20,20,5</vel_grid_dims>
<nd_back>1e16</nd_back>
</material>

<material name="HO" type="kinetic">
<molwt>17</molwt>
<charge>0</charge>
<spwt>1e10</spwt>
</material>
<!--
<material name="HO+" type="kinetic">
<molwt>17</molwt>
<charge>1</charge>
<spwt>1e10</spwt>
<particle_merge_skip>25</particle_merge_skip>
<vel_grid_dims>20,20,5</vel_grid_dims>
</material>
-->

<material name="H3O+" type="kinetic">
<molwt>19</molwt>
<charge>1</charge>
<spwt>1e3</spwt>
</material>

<material name="H2O+" type="kinetic">
<molwt>18</molwt>
<charge>1</charge>
<spwt>1e5</spwt>
<particle_merge_skip>25</particle_merge_skip>
<vel_grid_dims>20,20,5</vel_grid_dims>
<init>nd_back=1e4</init>
</material>

<material name="iH2O+" type="kinetic">
<molwt>18</molwt>
<charge>1</charge>
<spwt>1e3</spwt>
<particle_merge_skip>25</particle_merge_skip>
<vel_grid_dims>20,20,5</vel_grid_dims>
```

```
<init>nd_back=1e4</init>
</material>

</materials>
```

"interactions.xml"

```
<!-- material interactions file -->
<material_interactions>

<chemistry>
<sources>H2O,e-</sources>
<products>iH2O+,2*e-</products>
<rate type="poly">
<coeffs>1.36e-15</coeffs>-->
<dep_var>T.e-</dep_var>
</rate>
</chemistry>

<chemistry> <!--recombination H2O+ -->
<sources>H2O+,e-</sources>
<products>H2O</products>
<rate type="poly">
<coeffs>2.4e-16</coeffs>
<dep_var>T.e-</dep_var>
</rate>
</chemistry>

<chemistry> <!--recombination for new ions-->
<sources>iH2O+,e-</sources>
<products>H2O</products>
<rate type="poly">
<coeffs>2.4e-16</coeffs>
<dep_var>T.e-</dep_var>
</rate>
</chemistry>

<chemistry> <!--recombination H3O+ -->
<sources>H3O+,e-</sources>
<products>H2O</products>
<rate type="poly">
<coeffs>2.4e-15</coeffs>
```

```
<dep_var>T.e-</dep_var>
</rate>
</chemistry>

<!--Lishawa, 1990 Table 5-->
<chemistry>
<sources>H2O+,H2O</sources>
<products>HO,H3O+</products>
<rate type="table" is_sigma="true">
<table_values>
[1,2.9e-19], [1.5, 2.89E-19], [2, 1.86E-19],
[2.5, 8.51E-20], [5, 6.38E-20],
[6, 4E-20], [10, 3.13E-20], [15, 2e-20],
[20, 1.5e-20], [27, 0.5E-20]
</table_values>
<dep_var>T.H2O+</dep_var>
<input_wrappers>energy,JtoEv</input_wrappers>
</rate>
</chemistry>

<!--PEX for new ions, Lishawa, 1990 Table 5-->
<chemistry>
<sources>iH2O+,H2O</sources>
<products>HO,H3O+</products>
<rate type="table" is_sigma="true">
<table_values>
[1,2.9e-19], [1.5, 2.89E-19], [2, 1.86E-19],
[2.5, 8.51E-20], [5, 6.38E-20],
[6, 4E-20], [10, 3.13E-20], [15, 2e-20],
[20, 1.5e-20], [27, 0.5E-20]
</table_values>
<dep_var>T.iH2O+</dep_var>
<input_wrappers>energy,JtoEv</input_wrappers>
</rate>
</chemistry>

<!--Lishawa, 1990 Table 7-->
<mcc model="cex" name="cex">
<source>H2O+</source>
<target>H2O</target>
<sigma>table</sigma>
<sigma_tabulated>
[0.5769, 4.2396E-19], [1.0897, 2.2325E-19],
[1.2821, 1.5821E-19],[1.6026, 1.2907E-19],
[2.6923, 9.55E-20], [6.859, 8.231E-20],
```

```
[12.1795, 8.265E-20], [19.2949, 6.628E-20],
[25.0641, 6.665E-20], [30.3205, 5.353E-20]
</sigma_tabulated>
<sigma_dep_var>energy</sigma_dep_var>
<max_target_temp>10000</max_target_temp>
<frequency>1</frequency>
</mcc>


<!--CEX for new ions-->
<mcc model="cex" name="cex">
<source>iH2O+</source>
<target>H2O</target>
<sigma>table</sigma>
<sigma_tabulated>
[0.5769, 4.2396E-19], [1.0897, 2.2325E-19],
[1.2821, 1.5821E-19], [1.6026, 1.2907E-19],
[2.6923, 9.55E-20], [6.859, 8.231E-20],
[12.1795, 8.265E-20], [19.2949, 6.628E-20],
[25.0641, 6.665E-20], [30.3205, 5.353E-20]
</sigma_tabulated>
<sigma_dep_var>energy</sigma_dep_var>
<max_target_temp>10000</max_target_temp>
<frequency>1</frequency>
</mcc>
```

Bibliography

[1] Elaine M Petro and Raymond J Sedwick. Effects of Water Vapor Propellant on Helicon Thruster Peformance. In *52nd AIAA/SAE/ASEE Joint Propulsion Conference*, Salt Lake City, Utah, 2016. AIAA 2016-4735.

[2] D Rafalskyi and A Aanesland. Brief review on plasma propulsion with neutralizer-free systems. *Plasma Sources Science and Technology*, 25(4):43001, 2016.

[3] James H Gilland and G Piefer. Small Helicon Plasma Source Experiments. In *40th AIAA/ASME/SAE/ASEE Joint Propulsion Conference and Exhibit*, number 11-14 July, Fort Lauderdale, FL, 2004. AIAA 2004-3939.

[4] Jim Gilland. Application of a Helicon Discharge to Electric Propulsion. In *34th AIAA/ASME/SAE/ASEE Joint Propulsion Conference and Exhibit*, Cleveland, OH, 1998. AIAA 1998-3934.

[5] C. Charles. Hydrogen Ion Beam Generated by a Current-Free Double Layer in a Helicon Plasma. *Applied Physics Letters*, 84(3):332–334, 2004.

[6] N. Plihon, C. S. Corr, and P. Chabert. Double Layer Formation in the Expanding Region of an Inductively Coupled Electronegative Plasma. *Applied Physics Letters*, 86(9):1–3, 2005.

[7] C Charles, R W Boswell, R Laine, and P MacLellan. An Experimental Investigation of Alternative Propellants for the Helicon Double Layer Thruster. *Journal of Physics D: Applied Physics*, 41(17):175213, 2008.

[8] Franco Bosi, Fabio Trezzolani, Andrea Lucca Fabris, Marco Manente, Davide Melazzi, and Daniele Pavarin. Modelling and Optimization of Electrode-less Helicon Plasma Thruster with Different Propellants. In *50th AIAA/ASME/SAE/ASEE Joint Propulsion Conference*, Cleveland, OH, 2014. AIAA 2014-3404.

[9] Eduardo Ahedo. Plasmas for space propulsion. *Plasma Physics and Controlled Fusion*, 124037, 2011.

[10] P. Pergola. Semianalytic Approach for Optimal Configuration of Electric Propulsion Spacecraft. *IEEE Transactions on Plasma Science*, 43(1):305–320, 2015.

[11] Dan M Goebel and Ira Katz. *Fundamentals of Electric Propulsion*. Wiley & Sons, 2008.

[12] Robert G Jahn. *Physics of Electric Propulsion*. Courier Corporation, 2012.

[13] Manuel Martinez-Sanchez and Pollar. Spacecraft Electric Propulsion — An Overview. *Journal of Propulsion and Power*, 14(5):688–699, 1998.

[14] Marc Rayman, Thomas Fraschetti, Carol Raymond, and Christopher Russell. DAWN: A mission in development for exploration of main belt asteroids Vesta and Ceres. *Acta Astronautica*, 58(11):605–616, 2006.

[15] Dale Arney and Alan Wilhite. Rapid Cost Estimation for Space Exploration Systems. In *AIAA SPACE 2012 Conference & Exposition,*, pages AIAA–2012–5183, 2012.

[16] Christopher Russell and Carol Raymond. *The DAWN Mission to Vesta and Ceres*. Springer, New York, vol. 1 edition, 2012.

[17] James E Polk, R Y Kakuda, John R Brophy, V K Rawlin, Michael J. Patterson, James S Sovey, and J Hamley. Performance of the NSTAR ion propulsion system on the Deep Space One mission. pages AIAA–2001–965, 2001.

[18] Hitoshi Kuninaka, Kazutaka Nishiyama, Ikko Funaki, Tetsuya Yamada, and Yukio Shimizu. Powered Flight of Electron Cyclotron Resonance Ion Engines on Hayabusa Explorer. *Journal of Propulsion and Power*, 23(3), 2007.

[19] David Milligan, Octavio Camino, and Daniel Gesta. SMART-1 electric propulsion: an operational perspective. In *9th International Conference on Space Operations*, pages AIAA–2006–5767, Rome, Italy, 2006.

[20] John R Brophy. The DAWN Ion Propulsion System. *Space Science Reviews*, 1(4):251–261, 2011.

[21] Yasuo Horiuchi and Hitoshi Kuninaka. Enabling Inexpensive Robotic Precursors with the MU-10 Microwave Discharge Ion Engine Systemo Title. In *AIAA SPACE 2012 Conference & Exposition*, pages AIAA–2012–5325, 2012.

[22] David Y Oh. Evaluation of Solar Electric Propulsion Technologies for Discovery-Class Missions. *Journal of Spacecraft and Rockets*, 44(2):399–411, 2007.

[23] David Y Oh, John Steven Snyder, Dan M Goebel, Richard R Hofer, and Thomas M Randolph. Solar Electric Propulsion for Discovery-Class Missions. *Journal of Spacecraft and Rockets*, 51(6), 2014.

[24] George R Schmidt, David H Manzella, Hani Kamhawi, Tibor Kremic, Steven R Oleson, John W Dankanich, and Leonard A Dudzinski. Radioisotope electric propulsion (REP): A near-term approach to nuclear propulsion. *Acta Astronautica*, 66(3-4):501–507, 2010.

[25] Torsten Bondo, Roger Walker, Andrew Willig, Andreas Rathke, Dario Izzo, and Mark Ayre. Preliminary Design of an Advanced Mission to Pluto. pages ISTS–2004–k–10, 2004.

[26] C Casaregola, K. Geurts, P. Pergola, and Andrenucci. M. Radioisotope Low-Power Electric Propulsion Missions to the Outer Planets. In *Joint Propulsion Conference*, number July, pages AIAA–2007–5234, 2007.

[27] M. Buie, J. Veverka, L. Johnson, and M. Adams. Chiron Orbiter Mission: Misson Concept Study Report to the NRC Planetary Science Decadal Survey, Primitive Bodies Panel. NASA Goddard Space Flight Center, may 2010.

[28] M Omair, R. Amini, and J. Ervin. Joint Radioisotope Electric Propulsion Studies – Neptune System Explorer. *Journal of the British Interplanetary Society*, 63(11):454, 2011.

[29] Steven Oleson, Scott Benson, Leon Gefert, Michael Patterson, and Jeffrey Schreiber. Radioisotope electric propulsion for fast outer planetary orbiters. Number July, pages AIAA–2002–3967, 2002.

[30] Robert J Noble, Patricia M Beauchamp, Gary L Bennett, Metaspace Enterprises, John R Brophy, Bonnie J Buratti, Joan Ervin, and Jared Lang. New Opportunities for Outer Solar System Science using Radioisotope Electric Propulsion. pages SLAC–PUB–13772, sep 2009.

[31] Richard R Hofer and Thomas M Randolph. Mass and Cost Model for Selecting Thruster Size in Electric Propulsion Systems. *Journal of Propulsion and Power*, 29(1):166–177, 2013.

[32] Onboard Hayabusa and Asteroid Explorer. Flight tatus of cathode-less microwave discharge ion engines onboard Hayabusa asteroid explorer. pages AIAA–2004–3438, 2004.

[33] John R Brophy, Michael G Marcucci, Gani B Ganapathi, Charles E Garner, Michael D Henry, Barry Nakazono, and Don Noon. The Ion Propulsion System For Dawn. pages AIAA–2003–4542, 2003.

[34] W Andrew Hoskins, R. Joseph Cassidy, Olwen Morgan, Roger M Myers, Fred Wilson, and David Q King. 30 Years of Electric Propulsion Flight Experience

at Aerojet Rocketdyne. In *33rd International Electric Propulsion Conference*, pages IEPC–2013–439, Washington, D.C., 2013.

[35] Michael J Patterson, Scott W Benson, Digital Control, Interface Unit, Earth Gravity Assist, Engineering Model, Flow Control Device, and High Pressure Assembly. NEXT Ion Propulsion System Development Status and Performance. pages AIAA–2007–5199, 2007.

[36] W. P. Wright and P. Ferrer. Electric Micropropulsion Systems. *Progress in Aerospace Sciences*, 74:48–61, 2015.

[37] Dan M Goebel. Analytical Discharge Model for RF Ion Thrusters. *IEEE Transactions on Plasma Science*, 36(5):2111–2121, 2008.

[38] Busek RF Ion Thrusters. *http://www.busek.com/index_htm_files/70008514B.pdf*, page Accessed on 16 Nov. 2015.

[39] H Bassner, Daimlercrysler Aerospace, R Bond, V Thompson, A E A Technology, Robert Bond, and Vaughan Thompson. Development and Performance Testing of the ESA-XX Ion Thruster. In *35th AIAA / ASME / SAE / ASEE Joint Propulsion Conference and Exhibit*, pages AIAA 99–2441, 1999.

[40] Toshiyuki Ozaki, Yukikazu Kasai, Yasutaka Inanaga, Takafumi Nakagawa, Hiroyuki Osuga, Takashi Itoh, Kenichi Kajiwara, Katsuaki Matsui, Senior Engineer, Kamakura Works, Kamakura Works, Head Researcher, Kamakura Works, Head Engineer, Kamakura Works, Engineering Test, Satellite-viii Project Team, Spacecraft Propulsion, Engineering Group, and Technical Division. Electric Propulsion Development Activity at MELCO. pages AIAA–2006–4321, 2006.

[41] Hitoshi Kuninaka and Kenichi Kajiwara. Overview of JAXA's Activities on Electric Propulsion. In *32nd International Electric Propulsion Conference*, pages IEPC–2011–05, Wiesbaden, Germany, 2011.

[42] Vladimir Kim, Garri Popov, Valery Garkusha, Alexander Semenkin, and Sergei Tverdokhlebov. Electric Propulsion Activity in Russia. In *27th International Electric Propulsion Conference,*, pages IEPC–01–05, Pasadena, CA, 2001.

[43] Hitoshi Kuninaka, Kazutaka Nishiyama, Ikko Funaki, and Yukio Shimizu. Assessment of Plasma Interactions and Flight Status of the HAYABUSA Asteroid Explorer Propelled by Microwave Discharge Ion Engines. *IEEE Transactions on Plasma Science*, 34(5):2125–2132, 2010.

[44] Michael J Patterson and George C Soulas. Expanded Throttling Capabilities of the NEXT Thruster. In *49th AIAA/ASME/SAE/ASEE Joint Propulsion Conference*, pages AIAA 2013–3891, San Jose, CA, 2013.

[45] J E Polk, D Brinza, R Y Kakuda, J R Brophy, I Katz, J R Anderson, Nasa Glenn, and Brookpark Rd. Demonstration of the NSTAR Ion Propulsion System on the Deep Space One Mission. In *27th International Electric Propulsion Conference*, pages IEPC–01–075, Pasadena, CA, 2001.

[46] K. R. Chien, S. L. Hart, W. G. Tighe, M. K. DePano, T. A. Bond, and R. Spears. L-3 Communications ETI Electric Propulsion Overview. In *29th International Electric Propulsion Conference,*, pages IEPC–2005–315, Princeton, NJ, 2005.

[47] Helmut Bassner, Rainer Killinger, Hans Leiter, and Johann Müller. Development Steps of the RF-Ion Thrusters RIT. In *27th International Electric Propulsion Conference*, pages IEPC–01–105, Pasadena, CA, 2001.

[48] Hans J Leiter, Ralf Kukies, and Rainer Killinger. RIT-22 Ion Engine Development - Endurance Test and Life Prediction. Number July, pages AIAA–2006–4667, 2006.

[49] C Bundesmann, M Tartz, F Scholze, H Neumann, H J Leiter, F Scortecci, and D Feili. In-situ temperature, grid curvature, erosion, beam and plasma characterization of a gridded ion thruster RIT-22. In *31st International Electric Propulsion Conference*, pages IEPC–2009–160, Ann Arbor, MI, 2009.

[50] K H Groh and H W Loebtt. State-of-the-Art of Radio-Frequency Ion Thrusters. *Journal of Propulsion and Power*, 7(4):573–579, 1991.

[51] Mark W. Crofton. Evaluation of the United Kingdom Ion Thruster. *Journal of Spacecraft and Rockets*, 33(5):739–747, 1996.

[52] John Steven Snyder, Dan M Goebel, Richard R Hofer, and James E Polk. Performance Evaluation of the T6 Ion Engine. *Journal of Propulsion and Power*, 28(2):371–379, 2012.

[53] 8cm Xenon Ion Propulsion System (XIPS), 2013.

[54] Kuei-ru Chien, William G Tighe, Thomas A Bond, and Rafael Spears. An Overview of Electric Propulsion at L-3 Communications , Electron Technologies Inc. In *42nd AIAA/ASME/SAE/ASEE Joint Propulsion Conference & Exhibit*, number July, pages AIAA–2006–4322, Sacramento, CA, 2006.

[55] William G Tighe, Kuei-ru Chien, and Ezequiel Solis. Performance Evaluation of the XIPS 25-cm Thruster for Application to NASA Discovery Missions. In *42nd AIAA/ASME/SAE/ASEE Joint Propulsion Conference & Exhibit*, pages AIAA–2006–4666, Sacramento, CA, 2006.

[56] A. Shagayda. On Scaling of Hall Effect Thrusters. *IEEE Transactions on Plasma Science*, 43(1):12–28, 2014.

[57] M. Yu. Potapenko and V V Gopanchuk. Characteristic Relationship between Dimensions and Parameters of a Hybrid Plasma Thruster. In *32nd International Electric Propulsion Conference*, pages IEPC–2011–042, Wiesbaden, Germany, 2011.

[58] Yevgeny Raitses, Artem Smirnov, and Nathaniel J Fisch. Cylindrical Hall Thrusters. pages AIAA–2006–3245, San Francisco, CA, 2006.

[59] N Koch, M Schirra, S Weis, A Lazurenko, B Van Reijen, J Haderspeck, A Genovese, P Holtmann, Thales Electron, Devices Gmbh, R Schneider, K Matyash, and O Kalentyev. The HEMPT Concept - A Survey on Theoretical Considerations and Experimental Evidences. In *32nd International Electric Propulsion Conference*, pages IEPC–2011–236, Wiesbaden, Germany, 2011.

[60] James Szabo, Bruce Pote, Surjeet Paintal, Mike Robin, Adam Hillier, Richard D Branam, and Richard E Huffman. Performance Evaluation of an Iodine-Vapor Hall Thruster. *Journal of Propulsion and Power*, 28(4):848–857, 2012.

[61] Busek Low Power Hall Thrusters. *http://www.busek.com/index_htm_fil'es/70008510B.pdf*, page Accessed on 16 Nov. 2015.

[62] J. W. Dankanich, J. Szabo, B. Pote, S. Oleson, and H Kamhawi. Mission and system advantages of iodine Hall thruster. pages AIAA–2014–3905, 2014.

[63] Richard R Hofer, Thomas M Randolph, David Y Oh, John Steven Snyder, and Kristi H De Grys. for NASA Science Missions. (July):1–26, 2006.

[64] BPT-2000 and BPT-4000 Hall Effect Thruster Specification Sheets. *https://www.rocket.com/files/aerojet/documents/Capabilities/PDFs/Electric Propulsion Data Sheets.pdf*, page Accessed on 16 Nov. 2015.

[65] Mihui Seo, Jongsub Lee, Jongho Seon, Hae June Lee, Wonho Choe, Mihui Seo, Jongsub Lee, Jongho Seon, Hae June Lee, and Wonho Choe. Radial scale effect on the performance of low-power cylindrical Hall plasma thrusters Radial scale effect on the performance of low-power cylindrical Hall plasma thrusters. *Applied Physics Letters*, 103:133501, 2013.

[66] K. A. Polzin, T. E. Markusic, B. J. Stanojev, A. Dehoyos, Y. Raitses, A. Smirnov, and N. J. Fisch. Performance of a low-power cylindrical Hall thruster. *Journal of Propulsion and Power*, 23(4):886–888, 2007.

[67] Peter Y Peterson. Hall Thruster Technology for NASA Science Missions: HiVHAC Status Update. Number July, pages AIAA–2007–5236, 2007.

[68] H. Kamhawi, T. Haag, L. Pinero, W. Huang, T. Peterson, D. Manzella, and D. Hobson. Overview of the Development of a Low Cost High Voltage Hall Accelerator Propulsion System for NASA Science Missions. pages AIAA–2011–5520, 2011.

[69] C. Ducci, S. Oslyak, D. Dignani, R. Albertoni, and M Andrenucci. HT100D performance evaluation and endurance test results. In *33rd International Electric Propulsion Conference*, pages IEPC–2013–140, Washington, D.C., 2013.

[70] J Gonzalez and G Saccoccia. ESA Electric Propulsion Activities. In *32nd International Electric Propulsion Conference*, pages IEPC–2011–329, Wiesbaden, Germany, 2011.

[71] H. De Clercq, C. Rijm, E. Bourguignon, T. Scalais, and V. Lempereur. High Power Processing Unit for Stationary Plasma Thruster. In *Proceedings of the 3rd International Conference on Spacecraft Propulsion*, Cannes, France, 2000.

[72] G. D. Racca, A. Marini, L. Stagnaro, J. Van Dooren, L. Di Napoli, B. H. Foing, and R. Lumb. SMART-1 mission description and development status. *Planetary and Space Science*, 50(14):1323–1337, 2002.

[73] Nicolas Cornu, Frédéric Marchandise, Franck Damon, and Denis Estublier. The PPS 1350-G Qualification Demonstration : 10500 hrs on the Ground and 5000 hrs in Flight. pages AIAA–2007–5197, 2007.

[74] David H Manzella, David T Jacobson, and Robert S Jankovsky. High Voltage SPT Performance. pages AIAA–2001–3774, 2001.

[75] O. A. Mitrofanova, R. Y. Gnizdor, V. M. Murashko, A. I. Koryakin, and A. N Nesterenko. New Generation of SPT-100. In *32nd International Electric Propulsion Conference*, pages IEPC–2011–041, Wiesbaden, Germany, 2011.

[76] C Mclean and B Mcvey. Testing of a U.S.-built HET system for orbit transfer applications. In *35th AIAA / ASME / SAE / ASEE Joint Propulsion Conference and Exhibit*, pages AIAA–1999–2574, 1999.

[77] Atsushi Shirasaki, Hirokazu Tahara, and Takao Yoshikawa. Operational characteristics of cylindrical Hall thrusters. In *28th International Electric Propulsion Conference*, pages IEPC–03–051, Toulouse, France, 2003.

[78] A. Shirasaki and H. Tahara. Plume Measurements and Miniaturization of the Hall Thrusters with Circular Cross-sectional Discharge Chambers. In *29th International Electric Propulsion Conference*, pages IEPC–2005–051, Princeton, NJ, 2005.

[79] Francis F. Chen. Physics of Helicon Discharges. *Physics of Plasmas*, 3(5):1783, 1996.

[80] Christine Charles and Rod Boswell. Current-free double-layer formation in a high-density helicon discharge. *Applied Physics Letters*, 82(9):1356–1358, 2003.

[81] Francis F. Chen. Ion Ejection from a Permanent-Magnet Mini-Helicon Thruster. *Physics of Plasmas*, 21(9), 2014.

[82] Kazunori Takahashi, Christine Charles, Rod Boswell, and Akira Ando. Effect of Magnetic and Physical Nozzles on Plasma Thruster Performance. *Plasma Sources Science and Technology*, 23(4), 2014.

[83] Francis F Chen. Helicon Discharges and Sources: A Review. *Plasma Sources Science and Technology*, 24(1), 2015.

[84] C. Charles. A Review of Recent Laboratory Double Layer Experiments. *Plasma Sources Science and Technology*, 16:R1–R25, 2007.

[85] E. Ahedo and M. Merino. Two-Dimensional Supersonic Plasma Acceleration in a Magnetic Nozzle. *Physics of Plasmas*, 17(7):Paper 073501, 2010.

[86] T. Lafleur. Helicon Plasma Thruster Discharge Model. *Physics of Plasmas*, 21(4), 2014.

[87] F. F. Chen. Experiments on Helicon Plasma Sources. *Journal of Vacuum Science & Technology A: Vacuum, Surfaces, and Films*, 10(4):1389–1401, 1992.

[88] Logan T Williams and Mitchell L R Walker. Thrust Measurements of a Helicon Plasma Source. In *AIAA/ASME/SAE/ASEE Joint Propulsion Conference & Exhibit*, number August, pages AIAA–2011–5893, 2011.

[89] Jared P. et al Squire. Development toward a Spaceflight Capable VASIMR Engine and SEP Applications. In *AIAA SPACE 2014 Conference and Exposition*, pages AIAA–2014–4173, San Diego, CA, 2014.

[90] Benjamin W. Longmier, Jared P. Squire, Chris S. Olsen, Leonard D. Cassady, Maxwell G. Ballenger, Mark D. Carter, Andrew V. Ilin, Tim W. Glover, Greg E. McCaskill, Franklin R. Chang Díaz, and Edgar a. Bering. Improved Efficiency and Throttling Range of the VX-200 Magnetoplasma Thruster. *Journal of Propulsion and Power*, 30(1):123–132, 2014.

[91] S. et. al. Harada. Electrostatic acceleration of helicon plasma using a cusped magnetic field. *Applied Physics Letters*, 105(19):194101, 2014.

[92] S Shinohara. High-density helicon plasma sources: Basics and application to electrodeless electric propulsion. *Fusion Science and Technology*, 63(1):164–167, 2013.

[93] Shunjiro Shinohara, Hiroyuki Nishida, Takao Tanikawa, Tohru Hada, Ikkoh Funaki, and Konstantin P Shamrai. Development of Electrodeless Plasma Thrusters With High-Density Helicon Plasma Sources. *IEEE Transactions on Plasma Science*, 42(5):1245–1254, 2014.

[94] Sabrina Pottinger, Vaios Lappas, Christine Charles, and Rod Boswell. Performance characterization of a helicon double layer thruster using direct thrust measurements. *Journal of Physics D: Applied Physics*, 44(23):235201, 2011.

[95] F Trezzolani, A Lucca Fabris, D Pavarin, A Selmo, A I Tsaglov, A V Loyan, O P Rubalov, and M Manente. Low Power Radio-Frequency Plasma Thruster Development and Testing. In *33rd International Electric Propulsion Conference*, pages IEPC–2013–153, Washington, D.C., 2013.

[96] Oleg V. Batishchev. Minihelicon plasma thruster. *IEEE Transactions on Plasma Science*, 37(8):1563–1571, 2009.

[97] FR Chang Díaz, J. P. Squire, and T. Glover. VASIMR Engine: Project Status and Recent Accomplishments. In *42nd AIAA Aerospace Sciences Meeting and Exhibit*, Reno, NV, 2004.

[98] Tim W Glover, Franklin Chang Diaz, Verlin Jacobson, Alfonso G Tarditi, and Jared P Squire. Ion Cyclotron Heating Results in the VASIMR VX-10. In *40th AIAA/ASME/SAE/ASEE Joint Propulsion Conference*, number July, pages AIAA–2004–3639, 2004.

[99] Amnon Fruchtman. Neutral Depletion in a Collisionless Plasma. *IEEE Transactions on Plasma Science*, 36(2, Part I):403–413, 2008.

[100] John Vitucci and Raymond Sedwick. Development of a Superconducting Helicon Thruster. In *48th AIAA/ASME/SAE/ASEE Joint Propulsion Conference & Exhibit*, Atlanta, GA, 2012. AIAA 2012-3866.

[101] Eduardo Ahedo and Jaume Navarro-Cavalle. Helicon Thruster Plasma Modeling: Two-Dimensional Fluid-dynamics and Propulsive Performances. *Physics of Plasmas*, 20(4):043512, 2013.

[102] Adriane Faust and Raymond J Sedwick. Comparison of Diagnostics for Argon and Water Vapor Plasma with a Helium Seed Gas in a Helicon Thruster. In *52nd Aerospace Sciences Meeting, AIAA SciTech*, National Harbor, MD, 2014. AIAA 2014-0141.

[103] Sonca V T Nguyen, John E. Foster, and Alec D. Gallimore. Operating a Radio-Frequency Plasma Source on Water Vapor. *Review of Scientific Instruments*, 80(8), 2009.

[104] R. N. Franklin. Electronegative Plasmas - Why Are They So Different? *Plasma Sources Science and Technology*, 11:A31–A37, 2002.

[105] N. Oudini, J. L. Raimbault, P. Chabert, A. Meige, and A. Aanesland. Particle-in-Cell Simulation of an Electronegative Plasma under Direct Current Bias Studied in a Large Range of Electronegativity. *Physics of Plasmas*, 20(4), 2013.

[106] Yukikazu Itikawa and Nigel Mason. Cross sections for Electron Collisions with Water Molecules. *Journal of Physical and Chemical Reference Data*, 34(1):1–22, 2005.

[107] Francis F. Chen and Rod W. Boswell. Helicons-the past decade. *IEEE Transactions on Plasma Science*, 25(6):1245–1257, 1997.

[108] K. Takahashi, C. Charles, R. W. Boswell, T. Kaneko, and R. Hatakeyama. Measurement of the Energy Distribution of Trapped and Free Electrons in a Current-Free Double Layer. *Physics of Plasmas*, 14(11), 2007.

[109] F Cannat, T Lafleur, J Jarrige, P Chabert, P Elias, and D Packan. Optimization of a coaxial electron cyclotron resonance plasma thruster with an analytical model. *Physics of Plasmas*, 22(5), 2015.

[110] J P Passchier and W J Goedheer. Relaxation Phenomena after Laser-Induced Photodetachment in Electronegative RF Discharges. *Journal of Applied Physics*, 73(3):1073–1079, 1993.

[111] I D Kaganovich, R. N. Franklin, and V I Demidov. Introduction to Complex Plasmas: Principles of Plasma Transport in Multicomponent Plasmas. In Michael Bonitz, Norman Horing, and Patrick Ludwig, editors, *Springer Series on Atomic, Optical and Plasma Physics*, pages 17–39. Springer, New York, NY, 59 edition, 2010.

[112] Christine Charles and Rod W. Boswell. Breakdown, Steady State, and Decay Regimes in Pulsed Oxygen Helicon Diffusion Plasmas. *Journal of Applied Physics*, 78(2):766–773, 1995.

[113] A Fridman and L Kennedy. *Plasma Physics and Engineering*. CRC Press, New York, NY, 2004.

[114] R J Goldston and P H Rutherford. *Introduction to Plasma Physics*. Taylor & Francis Group, New York, NY, 2000.

[115] R N Franklin. The Plasma - Sheath Boundary Region. *Journal of Physics D: Applied Physics*, 36:R309–320, 2003.

[116] N St J Braithwaite and J E Allen. Boundaries and Probes in Electronegative Plasmas. *Journal of Physics D: Applied Physics*, 21(12):1733–1737, 1988.

[117] Karl Ulrich Riemann. Bohm Criterion and Boundary Conditions for a Multicomponent System. *IEEE Transactions on Plasma Science*, 23(4):709–716, 1995.

[118] Dongsoo Lee, Noah Hershkowitz, and Greg D. Severn. Measurements of Ar+ and Xe+ Velocities Near the Sheath Boundary of Ar-Xe Plasma using Two Diode Lasers. *Applied Physics Letters*, 91(4):Paper 041505, 2007.

[119] S. D. Baalrud and C. C. Hegna. Determining the Bohm Criterion in Plasmas with Two Ion Species. *Physics of Plasmas*, 18(2), 2011.

[120] Manuel Martinez-Sanchez, Jaume Navarro-Cavalle, and Eduardo Ahedo. Electron cooling and finite potential drop in a magnetized plasma expansion. *Physics of Plasmas*, 22(5), 2015.

[121] M A Lieberman and A J Lichtenberg. *Principles of Plasma Discharges and Materials Processing.* Wiley, Hoboken, NJ, 2005.

[122] P A Thorn, M J Brunger, H Kato, M Hoshino, and H Tanaka. Cross Sections for the Electron Impact Excitation of the a3B1, b3A1 and B1A1 Dissociative Electronic States of Water. *Journal of Physics B: Atomic Molecular and Optical Physics*, 40(4):697–708, 2007.

[123] M. A. Khakoo, C. Winstead, and V. McKoy. Vibrational Excitation of Water by Electron Impact. *Physical Review A - Atomic, Molecular, and Optical Physics*, 79(5):Paper 052711, 2009.

[124] David D Blackwell and Francis F Chen. Time-Resolved Measurements of the Electron Energy Distribution Function in a Helicon Plasma. *Plasma Sources Science and Technology*, 10(2):226–235, 2001.

[125] E. E. Scime, A. M. Keesee, and R. W. Boswell. Mini-conference on helicon plasma sources. *Physics of Plasmas*, 15(5):Paper 058301, 2008.

[126] M Surendra, D B Graves, and G M Jellum. Self-Consistent Model of a Direct Current Glow Discharge. *Physical Review A*, 41(2):1112–1125, 1990.

[127] Yu. V. Kovtun. Mean Energy of Water Molecule Ionization by Electron Impact. *Technical Physics*, 60(8):1110–1118, 2015.

[128] a Fruchtman. Ambipolar and nonambipolar cross-field diffusions. *Plasma Sources Science and Technology*, 18:025033, 2009.

[129] Manuel Martínez-Sánchez and Eduardo Ahedo. Magnetic Mirror Effects on a Collisionless Plasma in a Convergent Geometry. *Physics of Plasmas*, 18(3):Paper 033509, 2011.

[130] Kazunori Takahashi, Daiki Sato, Koichi Takaki, and Akira Ando. Development of a compact magnetically expanding plasma source with a strong magnetic field. *Plasma Sources Science and Technology*, 22(5):055002, 2013.

[131] T. Lafleur, D. Packan, F. Cannat, J. Jarrige, and P. Q. Elias. Modelling of magnetic nozzle thrusters with application to ECR and Helicon thrusters. In *34th International Electric Propulsion Conference*, Hyogo-Kobe, Japan, 2015.

[132] Elaine M Petro and Raymond J Sedwick. Survey of Moderate-Power Electric Propulsion Systems. *Journal of Spacecraft and Rockets*, 54(3):529–541, 2017.

[133] E. A. Bering, F. R. Chang-Diaz, J. P. Squire, M. Brukardt, T. W. Glover, R. D. Bengtson, V. T. Jacobson, G. E. McCaskill, and L. Cassady. Electromagnetic Ion Cyclotron Resonance Heating in the VASIMR. *Advances in Space Research*, 42(1):192–205, 2008.

[134] Andrew V Ilin, Franklin R Chang Díaz, and Jared P Squire. Plasma Heating Simulation in the VASIMR System. In *43rd AIAA Aerospace Sciences Meeting and Exhibit*, pages AIAA–2005–0949, Reno, Nevada, 2005.

[135] Fumiko Otsuka. Numerical Studies of Ponderomotive Acceleration and Ion Cyclotron Resonance : Application to Next Generation Electric Thrusters. *Plasma and Fusion Research*, 8(1606012):1–14, 2013.

[136] S. Heuraux, F. da Silva, T. Ribeiro, B. Despres, M. Campos Pinto, J. Jacquot, E. Faudot, S. Wengerowsky, L. Colas, and L. Lu. Simulation as a tool to improve wave heating in fusion plasmas. *Journal of Plasma Physics*, 81(05), 2015.

[137] E M Hollmann, G Antar, R P Doerner, S C Luckhardt, E M Hollmann, G Antar, R P Doerner, and S C Luckhardt. Omegatron mass spectrometer for analysis of ion concentrations in hydrogenic plasmas Omegatron mass spectrometer for analysis of ion concentrations in hydrogenic plasmas. *Review of Scientific Instruments*, 72(1):623–626, 2001.

[138] Benjamin W Longmier, Jared P Squire, Leonard D Cassady, Maxwell G Ballenger, Mark D Carter, Chris Olsen, Andrew V Ilin, Tim W Glover, Greg E Mccaskill, Franklin R Chang Díaz, Ad Astra, and Rocket Company. VASIMR VX-200 Performance Measurements and Helicon Throttle Tables Using Argon and Krypton. In *32nd International Electric Propulsion Conference,*, pages IEPC–2011–156, Wiesbaden, Germany, 2011.

[139] SuperPower Inc. 2G HTS Coils. *http://www.superpower-inc.com/system/files/SP_Coil+Fact+Sheet_2014_v1.pdf*, pages Accessed on Sept. 1, 2017, 2014.

[140] Drew W Hazelton. 2G HTS Wire Development at Super-Power. *https://nationalmaglab.org/images/magnet_development/asc/searchable_docs/asc_resources/coated_conductors/2016/io_14_hazelton.pdf*, pages Accessed on Sept. 1, 2017., 2016.

[141] AMSC. Effects of Temperature and Magnetic Field on Amperium ® Wire Performance. *http://www.amsc.com/library/AMPIcBT_AN_A4_0112.pdf*, pages Accessed on Sept. 1, 2017, 2012.

[142] P. Chabert and Nicholas Braithwaite. *Physics of Radio-Frequency Plasmas.* Cambirdge University Press, Cambridge, U.K., 2011.

[143] Demin Zhou, Kazuhito Ohmi, Katsunobu Oide, Takeshi Matsuoka Ã, Timofei S Rudenko, Ikkoh Funaki, Konstantin P Shamrai, and Takahiro Nakamura. One Dimensional Modeling of Radio Frequency Electric Field Penetration into Magnetized Plasmas. *Japanese Journal of Applied Physics*, 51(9R):096021, 2012.

[144] C. K. Birdsall and A. Langdon. *Plasma Physics Via Computer Simulation.* McGraw-Hill, Inc., New York, NY, 1985.

[145] Elaine Petro and Raymond Sedwick. Effects of Water Vapor Propellant on Electrodeless Thruster Performance. *Journal of Propulsion and Power*, 33(6):1410–1417, 2017.

[146] Kengo Nakamura and Yoshinori Takao. Investigation of Ion Species in Water Plasma Discharges for Miniature Microwave Discharge Ion Thrusters. In *2018 Joint Propulsion Conference, AIAA Propulsion and Energy Forum, July 9-11,*, Cincinnati, Ohio, 2018.

[147] S V Avtaeva, A A General, and V A Kel'man. Kinetic model for low-density non-stationary gas discharge in water vapour. *J. Phys. D: Appl. Phys.*, 43:315201, 2010.

[148] A. Fridman. *Plasma Chemistry.* Cambridge University Press, 2008.

[149] C.R. Lishawa, R.A. Dressler, J.A. Gardner, R.H. Salter, and E. Murad. Cross sections and product energy analysis of H2O+ − H2O collisions at suprathermal energies. *The Journal of Chemical Physics*, 93(5):3196–3205, 1990.

[150] J Scott Miller, Steve H Pullins, Dale J Levandier, Yu-hui Chiu, and Rainer A Dressler. Xenon charge exchange cross sections for electrostatic thruster models. *Journal of Applied Physics*, 91(3):984–991, 2002.

[151] B Peart, R Forrest, and K T Dolder. Measurements of cross sections for detachment of electrons from C - and O - ions by electron impact. *Journal of Physics B: Atomic and Molecular Physics*, 12:847–853, 1979.

[152] B Peart, D S Walton, K T Dolder, D S Walton, B Peart, K T Dolder, B Peart, R Forrest, and K T Dolder. Electron detachment from H - ions by electron impact. *Journal of Physics B: Atomic and Molecular Physics Electron*, 3:1346–1356, 1970.

[153] A. Good, D. A. Durden, and P. Kebarle. Mechanism and Rate Constants of Ion–Molecule Reactions Leading to Formation of H+(H2O)n in Moist Oxygen and Air. *The Journal of Chemical Physics*, 52(1):222–229, 1970.

[154] L I Virin, R V Dzhagatspanyan, G V Karachevtsev, V K Potapov, and V L Talroze. *Ion–Molecule Reactions in Gases.* 1979.

[155] L G Bruskin, M A Koen, and I M Sidorov. Modelling of neutral-gas releases into the Earth's ionosphere. *Pure Appl. Geophys.*, 127:415, 1988.

[156] A V Eletskiy and B M Smirnov. The dissociative recombination of an electron and a molecular ion. *Usp. Fiz. Nauk*, 136(25), 1982.

[157] Starfish. *https://www.particleincell.com/starfish/*.

[158] K. Nakamura, H. Koizumi, M. Nakano, and T. Yoshinori. Effects of negative ions on discharge characteristics of water plasma source for a miniature microwave discharge ion thruster Effects of negative ions on discharge characteristics of water plasma source for a miniature microwave discharge ion thruster. *Physics of Plasmas*, 26(March):043508, 2019.

[159] Alexander Bennet, Christine Charles, and Rod Boswell. Separating the location of geometric and magnetic expansions in low-pressure expanding plasmas. *Plasma Sources Science and Technology*, 27(7):75003, 2018.

[160] Matt Wiebold, Yung-ta Sung, John E Scharer, Matt Wiebold, Yung-ta Sung, and John E Scharer. Experimental observation of ion beams in the Madison Helicon eXperiment Experimental observation of ion beams in the Madison Helicon eXperiment. *Physics of Plasmas*, 18(2011):063501, 2014.

[161] R. Kawashima, K. Hara, and K. Komurasaki. Numerical analysis of azimuthal rotating spokes in a crossed-field discharge plasma. *Plasma Sources Science and Technology*, 27(3), 2018.

[162] Jean Pierre Boeuf and Bhaskar Chaudhury. Rotating instability in low-temperature magnetized plasmas. *Physical Review Letters*, 111(15):1–5, 2013.

[163] S Mattei, K Nishida, M Onai, J Lettry, M Q Tran, and A Hatayama. A fully-implicit Particle-In-Cell Monte Carlo Collision code for the simulation of inductively coupled plasmas. *Journal of Computational Physics*, 350:891–906, 2017.